

2014-01-01

Design And SYNThesis Of Porous Organic Frameworks For H₂ And CH₄ Storage And For Selective CO₂ Adsorption

Venkata Neti

University of Texas at El Paso, pawanchem@gmail.com

Follow this and additional works at: https://digitalcommons.utep.edu/open_etd



Part of the [Chemistry Commons](#)

Recommended Citation

Neti, Venkata, "Design And SYNThesis Of Porous Organic Frameworks For H₂ And CH₄ Storage And For Selective CO₂ Adsorption" (2014). *Open Access Theses & Dissertations*. 1690.
https://digitalcommons.utep.edu/open_etd/1690

This is brought to you for free and open access by DigitalCommons@UTEP. It has been accepted for inclusion in Open Access Theses & Dissertations by an authorized administrator of DigitalCommons@UTEP. For more information, please contact lweber@utep.edu.

DESIGN AND SYNTHESIS OF POROUS ORGANIC FRAMEWORKS FOR H₂
AND CH₄ STORAGE AND FOR SELECTIVE CO₂ ADSORPTION

VENKATA SURYA PAVAN KUMAR NETI

Department of Chemistry

APPROVED:

Luis Echegoyen, Ph.D., Chair

Russell Chianelli, Ph.D.

James Salvador, Ph.D.

David Zubia, Ph.D.

Bonnie Gunn, Ph.D.

Benjamin C. Flores, Ph.D.
Dean of the Graduate School

Copyright ©

by

Venkata Surya Pavan Kumar Neti

2014

DESIGN AND SYNTHESIS OF POROUS ORGANIC FRAMEWORKS FOR H₂
AND CH₄ STORAGE AND FOR SELECTIVE CO₂ ADSORPTION

by

VENKATA SURYA PAVAN KUMAR NETI

DISSERTATION

Presented to the Faculty of the Graduate School of

The University of Texas at El Paso

in Partial Fulfillment

of the Requirements

for the Degree of

DOCTOR OF PHILOSOPHY

Department of Chemistry

THE UNIVERSITY OF TEXAS AT EL PASO

May 2014

Table of Contents

Table of Contents	iv
Acknowledgements	ivi
Abstract	v
List of Tables.....	viii
List of Figures	viii
Scope of this dissertation	1
Chapter 1: A Review of Porous Organic Frameworks	2
1.1 Covalent Organic Frameworks	3
1.2 Porous Organic Polymers	30
1.3 Metal Organic Frameworks	15
Chapter 2: Impact of pore size on H ₂ adsorption in covalent organic frameworks.....	29
1.1 Introduction	300
1.2 Experimental Section.....	30
1.3 Results and Discussion	308
1.4 Conclusions.....	75
1.5 References	76
Chapter 3: Impact of basicity on CO ₂ adsorption in porous organic polymers.....	78
2.1 Introduction	79
2.2 Experimental Section.....	82
2.3 Results and Discussion.....	85
2.4 Conclusions.....	117
2.5 References	117
Chapter 4: Synthesis of metal organic frameworks.....	119
3.1 Introduction	120
3.2 Experimental Section.....	122
3.3 Results and Discussion	124
3.4 Conclusions.....	142
3.5 References	142
Vita.....	143

Acknowledgements

First, I would like to thank Prof. Luis Echegoyen for his support, motivation and scientific freedom over these years. I appreciate his precious time for correcting my articles and reports and valuable advice on my PhD thesis. Also I would like to thank Professors Shuguang Deng (NMSU) and William R. Dichtel (Cornell) for their suggestions during my research and allowing me to work in their labs. Thanks to Professors Alan Balch and Marilyn Olmstead and Dr. Alejandro Metta for crystal structures. I also thank Professors Russell Chianelli, James Salvador, David Zubia, Bonnie Gunn, Katja Michael and Jorge Gardea. This would not have been possible without all their help.

Thanks to Dr. Mahsa Hosseini for teaching me X-ray diffraction data collection and SEM. Thanks to Xiaofei Wu for surface area measurements. Thanks to Dr. Juan Noveron for allowing me to use their Materials Studio facilities. Thanks to John Colson, David Bunck and Fernando Uribe-Romo (Dichtel research group) for teaching me techniques to make covalent organic frameworks.

Thanks to my previous and present lab mates Dr. Ning Chen, Dr. Rachana Singh, Dr. Fang-Fang Li, Dr. Ping Peng, Dr. Agustín Molina, Dr. Marta Izqueirido, Dr. Álvaro Duarte, Dr. Marta Plonska, Dr. Chia-Hsiang, Dr. Manuel Chaur, Dr. Angy Ortiz, Dr. Julio Pinzón, Cheryl Moore, Adrián Villalta-Cerdas, Danisha Rivera, Maira Cerón, Robert Cotta, Danny Arteaga, Alexis Tigreros, Nuria Alegret, Jesse Murillo, Fernando Delgado, Yuyang Li, Nathaly Ortiz, Mauricio Cerón, Vivian Triana, Catalina Suárez, David Buck, Edison Castro, Elías Muñoz, Raine Stene, and Guillermo Campos for scientific discussions and general encouragement. I thank Dr. Sohan DeSilva for NMR support and Dr. Jose Nuñez for help with IR spectroscopy. I particularly thank Gabriela Aguilar and Laura Flores for administrative and non-administrative support for the group and Grace Awad and Lucema Armenta in the chemistry department. Thanks to my classmates and friends in the chemistry departments both at Clemson University and at UTEP for their support when I've needed it the most.

Finally, I would like to thank my wife Madhu Latha for her unconditional love even when I neglected to spend time with her during my PhD and my mother, father and brother for their love and encouragement all these years.

Abstract

Three new boronate-ester based covalent organic frameworks (CoPc-PorDBA, CoPc-BPDA and HHTTP-PorDBA), an imine-linked porphyrin porous polymer (CuPor-BPDC) and imine and benzothiazole based porous polymers (IBTP), and a triazole based phthalocyanine “click” polymer (Pc-POP) were synthesized. The CoPc-PorDBA and CoPc-BPDA COFs exhibited high BET surface areas (1087, 1315 m² g⁻¹, respectively) whereas HHTTP-PorDBA showed a low BET surface area of 205 m² g⁻¹. The H₂ storage capacities of CoPc-BPDA and CoPc-PorDBA range between 0.8-1.2wt% at 77K, 1bar and the CH₄ storage capacities range between 0.4-0.8wt% at 298K, 1bar. These materials also had good thermal stabilities up to 350 °C. The BET surface areas of Porous polymers CuPor-BPDC, IBTP, and Pc-POP, are 428 m² g⁻¹, 442 m² g⁻¹, and 115 m² g⁻¹, and showed CO₂ capture capacities of 5.5 wt%, 7.8 wt%, and 11.9 wt%, respectively, at 273 K/1 bar with selectivities for CO₂/CH₄ adsorption ranging between 5.4-6.4. The chemical connectivity and composition of the COFs (CoPc-PorDBA, CoPc-BPDA, HHTTP-PorDBA) and of the polymers (CuPor-BPDC, IBTP, Pc-POP) were characterized by several methods such as infrared spectroscopy, powder X-ray diffraction (PXRD), solid-state ¹³C CP-MAS NMR, surface area measurements, solid-state UV-Vis, and thermogravimetric and elemental analysis.

List of Tables

Table 1.4: H ₂ and CH ₄ adsorption properties of covalent organic frameworks.	75
Table 2.4: H ₂ , CH ₄ , and CO ₂ adsorption properties of porous organic polymers.	116

List of Figures

Figure 1: Synthesis of COF-1.....	5
Figure 2: Synthesis of COF-5.....	5
Figure 3: Synthesis of TP-COF.....	6
Figure 4: Synthesis of ZnPc-ANDI-COF.....	7
Figure 5: Synthesis of 2D D-A COF.....	7
Figure 6: Synthesis of HHTP-PBBA COF on graphene surface	8
Figure 7: Synthesis of CTFs.....	10
Figure 8: Synthesis of COF-300.....	11
Figure 9: Synthesis of imine POFs.....	12
Figure 10: Synthesis of COF-42 and 43.....	13
Figure 11: Synthesis of "click" based POP.....	14
Figure 12: Synthesis of BILP-3 and 6.....	15
Figure 17: Synthesis of PPFs.....	19
Figure 18: PXRD of CoPc-PorDBA COF.....	39
Figure 19: IR1 of CoPc-PorDBA COF	42
Figure 20: IR2 of CoPc-PorDBA COF	42
Figure 21: N ₂ adsorption of CoPc-PorDBA COF	44
Figure 22: DPD of CoPc-PorDBA COF	44
Figure 23: CPD of CoPc-PorDBA COF	45
Figure 24: BET plot of CoPc-PorDBA COF	45
Figure 25: H ₂ adsorption of CoPc-PorDBA COF	46
Figure 26: CH ₄ adsorption of CoPc-PorDBA COF.....	46

Figure 27: UV-Vis of precursor of CoPc-PorDBA COF	47
Figure 28: Diffuse reflectance spectra of CoPc-PorDBA COF	48
Figure 29: $^{13}\text{C}/\text{CP}$ NMR of CoPc-PorDBA COF	49
Figure 30: $^{13}\text{C}/\text{CP}$ NMR of CoPc	49
Figure 31: SEM image of CoPc-PorDBA COF	50
Figure 32: TGA of CoPc-PorDBA COF	50
Figure 33: PXRD of CoPc-BPDA COF.....	52
Figure 34: IR1 of CoPc-BPDA COF	55
Figure 35: IR2 of CoPc- BPDA COF	56
Figure 36: Gas adsorption of CoPc-BPDA COF	57
Figure 37: DPD of CoPc-BPDA COF	58
Figure 38: CPD of CoPc-BPDA COF	59
Figure 39: BET plot of CoPc-BPDA COF	59
Figure 40: $^{13}\text{C}/\text{CP}$ NMR of CoPc-BPDA COF	60
Figure 41: $^{13}\text{C}/\text{CP}$ NMR of CoPc	61
Figure 42: SEM image of CoPc-BPDA COF	62
Figure 43: Cryo-TEM image of CoPc-BPDA COF	62
Figure 44: TGA of CoPc-BPDA COF	63
Figure 49: PXRD of HHTP- PorDBA COF.....	65
Figure 45: IR1 of HHTP- PorDBA COF	69
Figure 46: IR2 of HHTP - PorDBA COF	69
Figure 47: Gas adsorption of HHTP- PorDBA COF	71
Figure 48: DPD, CPD, and BET plot of HHTP- PorDBA COF	72
Figure 49: UV-Vis diffuse reflectance of HHTP- PorDBA COF	73

Figure 50: SEM image of HHTP- PorDBA COF	74
Figure 51: TGA of HHTP- PorDBA COF	74
Figure 52: PXRD of CuPor-BPDC.....	86
Figure 53: IR1 of CuPor-BPDC	87
Figure 54: IR2 of CuPor-BPDC	87
Figure 55: Gas adsorption of CuPor-BPDC	89
Figure 56: CPD, DPD and BET plot of CoPc-PorDBA COF	90
Figure 57: Vant't Hoff plots of CuPor-BPDC	91
Figure 58: Diffuse reflectance spectra of CuPor-BPDC	91
Figure 59: $^{13}\text{C}/\text{CP}$ NMR of CuPor-BPDC	92
Figure 60: $^{13}\text{C}/\text{CP}$ NMR of CuPor	93
Figure 61: SEM image of CuPor-BPDC	93
Figure 62: TGA of CuPor-BPDC	94
Figure 63: PXRD of IBTP.....	98
Figure 64: IR1 of IBTP	99
Figure 65: IR2 of IBTP	99
Figure 66: Gas adsorption of IBTP	101
Figure 67: CPD, DPD and BET plot of IBTP	102
Figure 68: Vant't Hoff plots of IBTP	103
Figure 69: Diffuse reflectance spectra of IBTP	104
Figure 70: $^{13}\text{C}/\text{CP}$ NMR of IBTP	105
Figure 71: SEM image of IBTP	105
Figure 72: TGA of IBTP	106
Figure 73: PXRD of Pc-POP.....	110

Figure 74: IR1 of Pc-POP	111
Figure 75: IR2 of Pc-POP	112
Figure 76: Gas adsorption of Pc-POP	113
Figure 77: CPD, DPD and BET plot of Pc-POP	114
Figure 78: Vant't Hoff plots of Pc-POP	115
Figure 79: Diffuse reflectance spectra of Pc-POP	115
Figure 80: ^{13}C /CP NMR of Pc-POP	116
Figure 81: SEM image of Pc-POP	116
Figure 82: TGA of Pc-POP	117
Figure 83: Synthesis of MOF-177 and MOF-177/BFG.....	124
Figure 84: PXRD of MOF-177 and MOF-177/BFG	125
Figure 85: IR1 of MOF-177 and MOF-177/BFG	126
Figure 86: IR2 of MOF-177 and MOF-177/BFG	126
Figure 87: Raman spectrum of MOF-177/BFG	127
Figure 88: N_2 adsorption of MOF-177 and MOF-177/BFG	128
Figure 89: CPD of MOF-177 and MOF-177/BFG	128
Figure 90: DPD of MOF-177 and MOF-177/BFG	129
Figure 91: SEM and TEM of MOF-177 and MOF-177/BFG	131
Figure 92: Fluorescence quenching selectivities of MOF-177 and MOF-177/BFG	132
Figure 93: Fluorescence quenching titrations of MOF-177 and MOF-177/BFG	133
Figure 94: Stern-Volmer plots of MOF-177/BFG	137
Figure 95: TGA of MOF-177 and MOF-177/BFG	138
Figure 96: Synthesis of ZnDPyP	139
Figure 97: Single crystal structure of ZnDPyP	140

Figure 98: Crystal packing of ZnDPyP	141
Figure 99: PXRD of ZnDPyP	142
Figure 100: TGA of ZnDPyP	143

Scope of this dissertation

Until 2010 most studies of metallated phthalocyanine-based COFs were mainly focused on donor and acceptor properties, aiming to find alternatives to replace bulk heterojunction solar cells. Thus, the H₂ storage potential of metallated phthalocyanine COFs have not been studied in detail. A few 3D COFs such as COF-102 and COF-301 were shown to possess H₂ storage capacities of 5.2 wt% and 0.44 wt% at 298K. When they are doped with palladium to give Pd@COF-102 and PdCl₂@COF-301, the H₂ storage properties were increased to 9.5 wt% and 4.2 wt%. Phthalocyanines can also bind a wide variety of metals such as Pd, Fe, Co etc. Incorporation of these transition metal ions into the core of the phthalocyanine or porphyrin should increase the H₂ storage capacities of metallated phthalocyanine or porphyrin COFs due to the presence of metal--H₂ interactions. Thus we decided to investigate the H₂ and CH₄ storage properties of a cobalt-based phthalocyanine and a porphyrin COF as well as their respective POPs exhibiting Co--H₂ interactions at low pressure (1atm) and at different temperatures (77K, 273K and 298K). In addition to H₂ and CH₄ storage properties, we also explored the CO₂ capture properties of a variety of nitrogen-containing in the porous organic polymers in order to find alternate solutions for existing commercial amine-based solutions for post combustion CO₂ capture and separation.

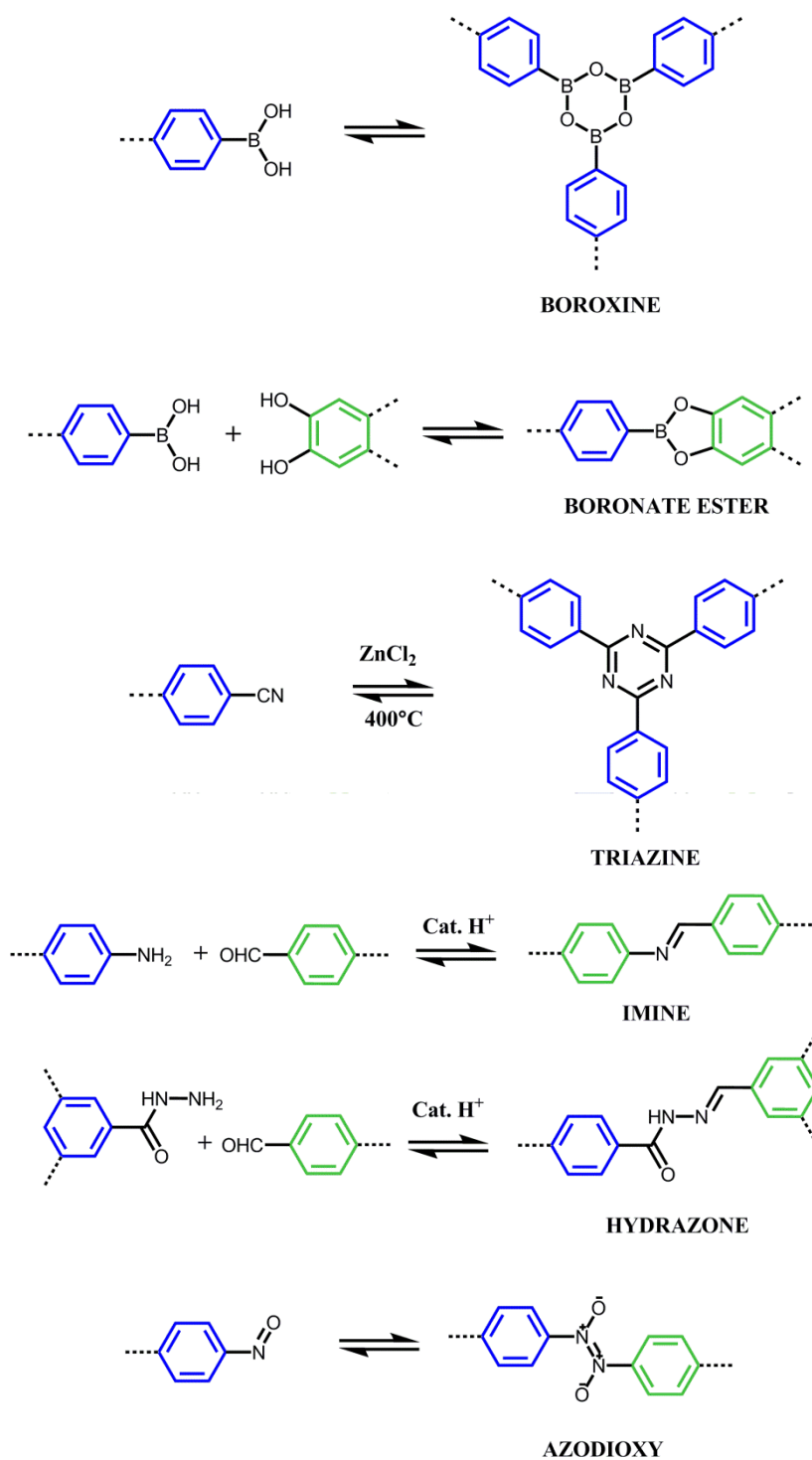
Chapter 1

Review of porous organic frameworks

1.1 Covalent Organic Frameworks:

Covalent Organic Frameworks (COFs) are crystalline porous materials formed by light weight elements (C, N, O, B, Si, H), and the linkages are made by strong, directional and thermodynamically stable covalent bonds.¹⁻¹³ Their construction involves reversible formation of covalent bonds (Scheme 1). A large variety of monomers can be used to construct COFs, and this versatility has enabled the rational design and assembly of materials having excellent properties for gas storage,¹⁴⁻¹⁶ to capture harmful gases of environmental importance¹⁷ (CO₂, NH₃, SO₂), for catalysis,¹⁸ optoelectronic applications¹⁹⁻²⁴ and in organic photovoltaics.²⁵

Some of the first examples of covalent organic frameworks are COF-1 and COF-5 (Figures 1 and 2).¹ Benzene-1,4-diboronic acid is an organic building block and the boronic acid functionalities form boroxine anhydrides after controlled dehydration, and these anhydrides constitute trigonal planar building units or secondary building units (SBU's). Even with the optimized conditions for crystallization, only microcrystalline powders were formed, not single crystals. The prediction of the crystal structures of frameworks is based on the geometry of the building blocks. For example, COF-1 is composed of three boronic acid molecules that converge to form a planar six-membered B₃O₃ (boroxine) ring after the elimination of three water molecules. These molecular structures of cyclotrimerized boronic acids are typically in planar conformations held together C–H_(o-C₆H₄)–O_(BO) [2.975 Å]^o hydrogen bonds.



Scheme 1. Dynamic chemical reactions for the synthesis of covalent organic frameworks.

Computer generated crystal models were created for both COF-1 and COF-5. Only two high symmetry nets, *gra* for COF-1 and *bnn* for COF-5, exist by connecting the hexagons. These models

were used to simulate the powder diffraction patterns. COFs are porous, and both COF-1 and COF-5 possess relatively high surface areas, $S_{\text{BET}} = 711 \text{ m}^2/\text{g}$ (COF-1) and $S_{\text{BET}} = 1590 \text{ m}^2/\text{g}$ (COF-5).

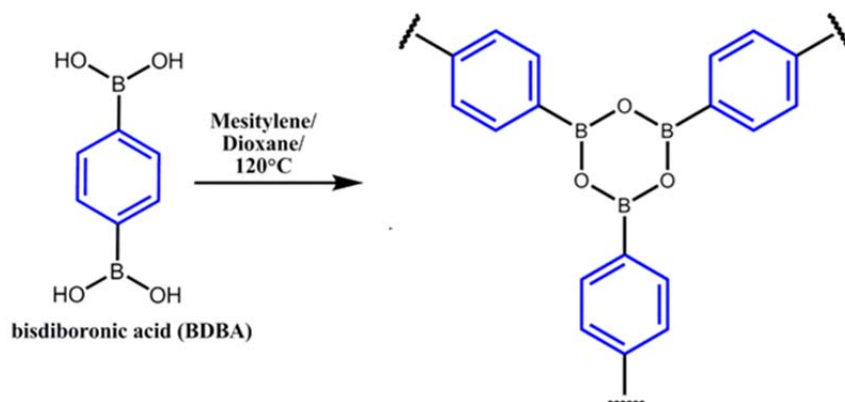


Figure 1. Synthesis of COF-1 from 1,4-biphenyldiboronic acid.

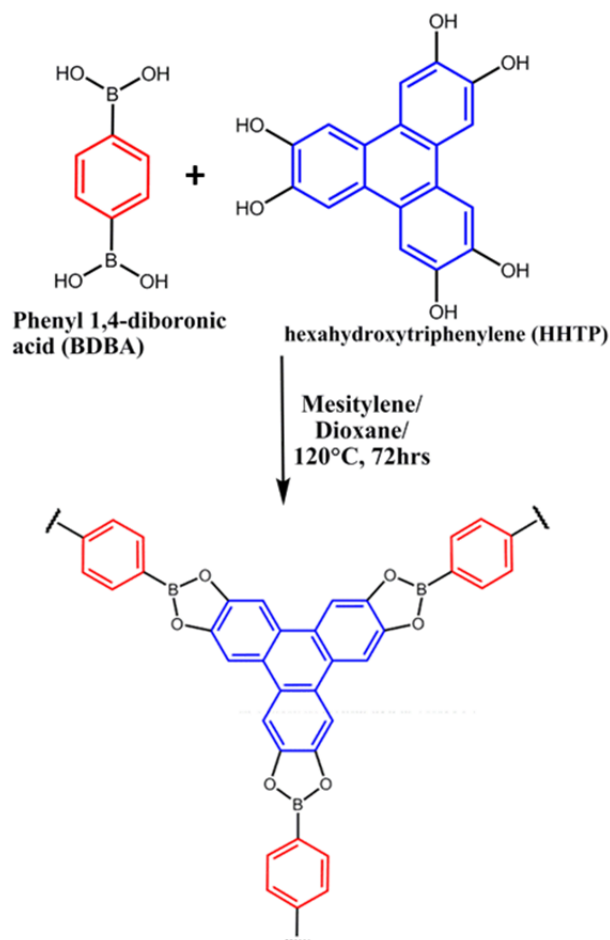


Figure 2. Synthesis of COF-5 from hexahydroxytriphenylene and 1,4-biphenyldiboronic acid.

In 2008, Jiang and co-workers first studied the luminescence and semiconducting properties of a belt shaped 2D TP-COF that contains pyrene diboronic acid and hexahydroxytriphenylene monomers (Figure 3).¹⁹ The semiconducting properties of this COF arise from the π -stacking of pyrene units that form structures that are 100nm thick and 300nm wide. It is also fluorescent when excited at 474nm, due to the vertical alignment of the pyrene units which strongly absorb photons in the UV-Vis region and emit in the blue. The TP-COF electric current can be switched on and off without any decomposition and a very high current was observed when it was doped with iodine. In 2011 and 2013 the same group measured charge dynamics in two 2D COFs containing donors and acceptors that were incorporated within the material.^{20,21} They analyzed the charge dynamics using time-resolved spectroscopy to elucidate the photochemical processes of the free charges from their generation to their delocalization. Based on these results they demonstrated that 2D layered COF materials are a new family of π -electronic frameworks that are potentially useful for optoelectronic applications. (Figures 4 and 5).

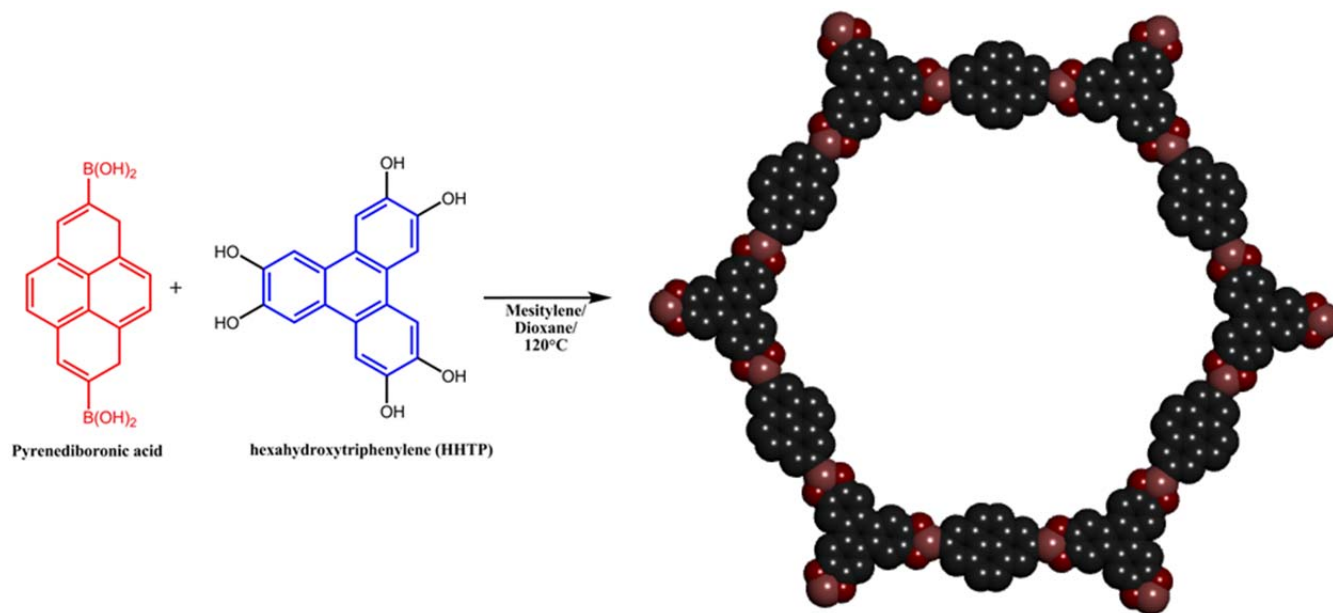


Figure 3. Synthesis of TP-COF from pyrene 1,4-diboronic acid and hexahydroxytriphenylene.

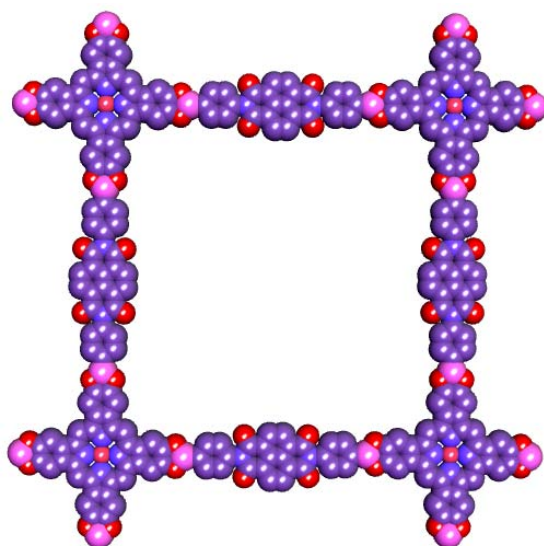


Figure 4. Donor–acceptor COF (DZnPc-ANDI-COF).

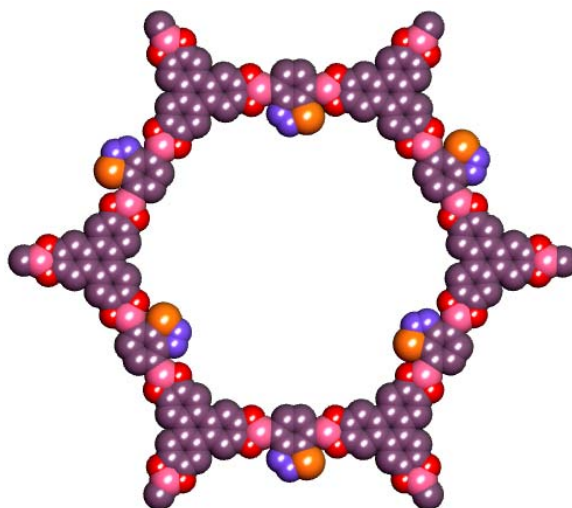


Figure 5. Synthesis of 2D D-A COF with self-sorted and periodic electron donor-accepter ordering and bicontinuous conducting channels

In 2011, Dichtel and co-workers reported thin films of vertically oriented 2D COFs on single-layer graphene (SLG on Cu and SiO₂ surfaces) under solvothermal reaction conditions (Figure 6).²² Unlike Jiang’s work which used powders of COFs between Au and Al electrodes, Dichtel’s work further advanced the field of COFs by placing SLG deposited substrates on SiO₂ and Cu in the reaction vessels. Different types of COFs such as COF-5, TP-COF, NiPc-COF, HHTP-DPB-COF, and ZnPc-PPE-COF have been successfully prepared and characterized by grazing angle X-ray diffraction measurements

using synchrotron radiation. The thin films possess high crystallinity, and the layer thicknesses can be tuned by varying the reaction temperatures and times.

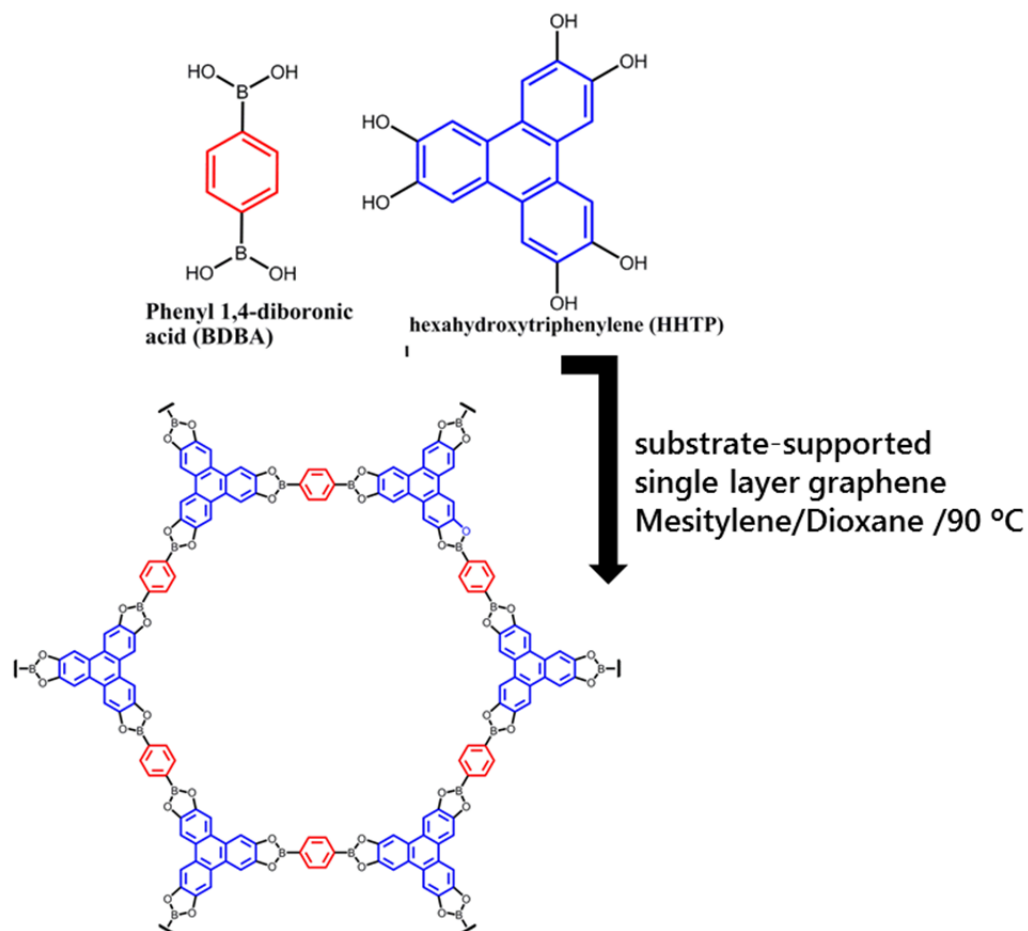


Figure 6. Synthesis of HHTP and PBBA in the presence of a substrate-supported single layer graphene surface provides COF-5 as both a film on the graphene surface, as well as a powder precipitated in the bottom of the reaction vessel.

1.2 Porous Organic Polymers (POPs)

In addition to covalent organic frameworks (COFs), a number of new micro and mesoporous amorphous networks called porous organic polymers (POPs) have been emerging as a new class of materials. These nanoporous organic polymers^{26–31} show considerable promise for gas capture³², storage³³ and separation technologies³⁴, and as nano-filtration membranes³⁵, catalysts³⁶, drug delivery

vehicles³⁷ and charge carriers.^{38,39} POPs are similar to COFs with respect to porosity but are more stable, particularly towards water, making them ideal for use in a variety of applications in real-world environments. POPs are further divided into sub classes (a) polymers of intrinsic microporosity (PIMs) (b) porous organic polymers (POPs) (c) conjugated microporous polymers (CMPs) (d) porous aromatic frameworks (PAFs). These porous organic polymers can easily be designed and synthesized from common organic reactions such as Suzuki and Sonogashira cross-coupling reactions, Yamamoto polymerization, and alkene and alkyne metathesis and other type of chemical reactions. To date, many amorphous porous organic materials with tunable functionalities have been developed.⁴⁰⁻⁵⁰

Efficient and selective separation of CO₂ from other gases in the atmosphere continues to be a major challenge. At present, organoamine solutions are commercial products used to capture CO₂. Porous solid adsorbents such as porous organic polymers are an alternative to capture CO₂, because regeneration of the amine solutions requires considerable energy and they are also highly corrosive. In order to avoid energy-intensive CO₂ capture, the ideal porous organic polymer should exhibit an enthalpy of adsorption (Q_{st}) less than 40 kJ mol⁻¹ (physisorption process). If any of these materials exhibit Q_{st} higher than 40 kJ mol⁻¹ they would have chemisorbed species. Physisorption is better because the porous organic polymer can be easily regenerated without applying heat. In order to improve the physisorption processes (a) the CO₂ selectivity of the POP should be high enough, which means that the porous polymer should capture CO₂ physisorbed, and (b) CO₂ uptake should be substantial. Nitrogen containing COFs and POPs are crystalline and amorphous porous networks containing robust polymeric C=N bonds. These materials have attracted significant attention due to their ability to capture CO₂ through R=N(δ^-)-C(δ^+)O₂ partial dipolar interactions. C-N linkages can be found in crystalline and amorphous materials such as triazine, imine, hydrazone, triazole, benzimidazole, and imide-based frameworks. Boronate ester and boroxine based COFs are known for the reactivity of the B-O bonds

towards moisture, hence C-N based crystalline or amorphous porous materials are better alternatives for practical applications such as CO₂ capture, H₂ and CH₄ storage.

In 2008, Kuhn and Thomas *et al* discovered a new class of polymer frameworks synthesized from simple aromatic nitriles with regular and irregular porosities (Figure 7).⁶ Via dynamic trimerization under ionothermal conditions, that is, in molten zinc chloride at high temperature, triazine-based materials with high porosities and surface areas were obtained.⁶ The yields of these reactions are generally close to quantitative and the polymers were synthesized by heating a molten mixture of the nitrile and ZnCl₂ in quartz ampules at 400 °C. Figure 7 shows a schematic representation of the formation of a triazine-based framework material by a trimerization reaction of 1,4-dicyanobenzene. Kuhn and Thomas *et al* proved that crystallinity is not a prerequisite for molecular control over pore size in rigid frameworks. Narrow pore size distributions have been obtained in three-dimensional porous organic polymers, showing that long-range order is not necessary for obtaining uniform pore sizes.

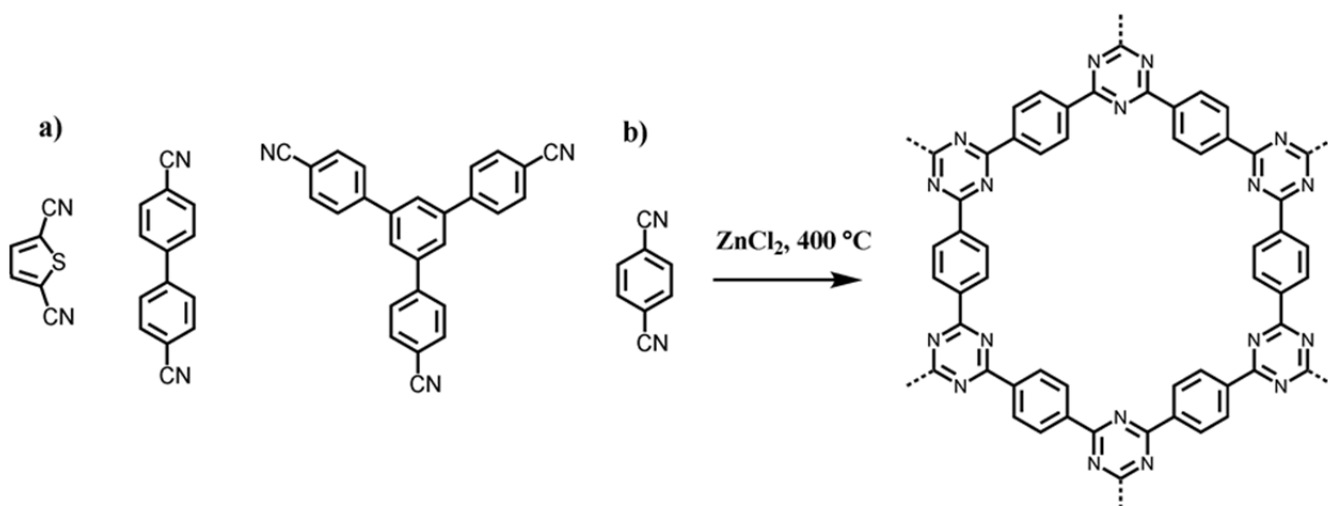


Figure 7. Nitrile monomers used for the ionothermal synthesis of polytriazine networks. b) Trimerization of dicyanobenzene in molten ZnCl₂ lead to trimers and oligomers and then to a covalent triazine-based framework (CTF-1).

In 2009 Yaghi *et al* successfully achieved the design, synthesis and characterization of crystalline imine-linked 3D COFs constructed solely by using C-C and C-N bonds.⁷ Schiff base condensation of tetra (4-anilyl) methane with terephthalaldehyde resulted in imine bond formation with elimination of water to give COF-300 (Figure 8). One pot synthesis of imine-linked amorphous microporous polymer organic frameworks (POFs) led to quantitative yields via Schiff base condensation between 1,3,5-triformylbenzene and several diamine monomers (Figure 9).¹⁸ These POFs exhibit high specific surface areas up to 1500 m²g⁻¹ with isosteric heats of H₂ adsorption up to 8.2 kJ mol⁻¹. In 2011, Yaghi *et al* reported another reversible covalent reaction that produces hydrazone framework materials with high porosity, low density, and high gas uptake. The hydrazone functional group is the combination of an amine with an imine through the neighbouring nitrogen atoms of the hydrazine.

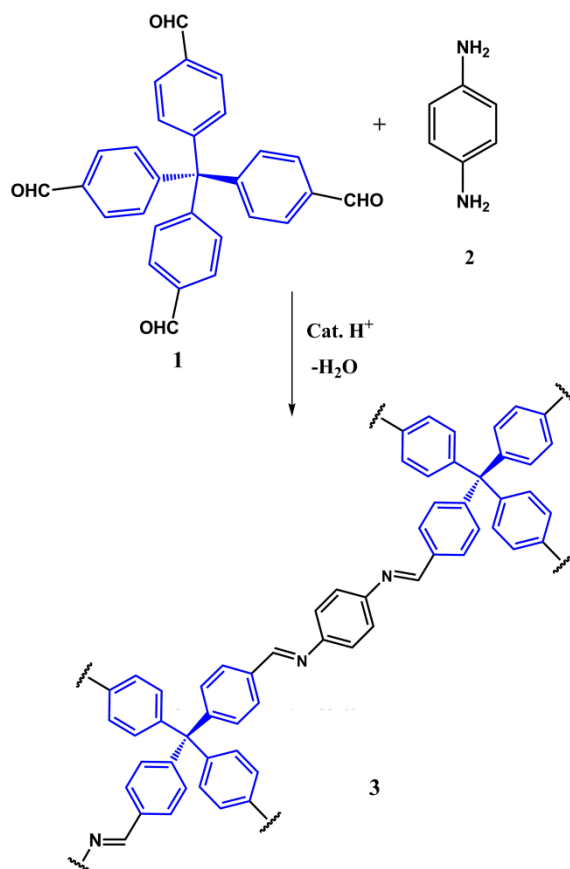


Figure 8. Condensation of divergent **1** with ditopic **2** leads to the rod-like bis-imines **3** which join together the tetrahedral building blocks to give the diamond structure of COF-300.

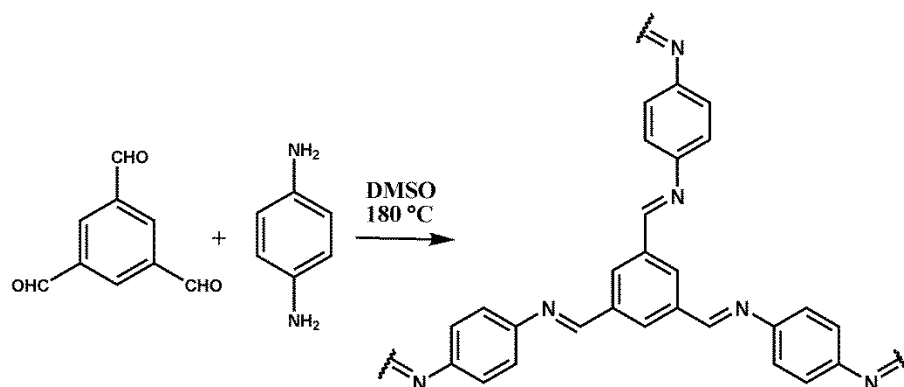


Figure 9. Synthesis of imine porous organic frameworks via Schiff base condensation polymerization.

Yaghi *et al* synthesized hydrazone COFs 42 and 43 (Figure 10) solvothermally by the reversible dehydration of 2,5-diethoxyterephthalohydrazide and 1,3,5-triformylbenzene and/or 1,3,5-tris(4-formylphenyl)benzene in mixtures of mesitylene, 1,4-dioxane, and acetic acid (6M) in sealed tubes under vacuum.¹¹ These materials are potentially useful for the capture of environmentally relevant gases such as CO₂ due to their nitrogen rich nature. However, no such studies have been published to date.

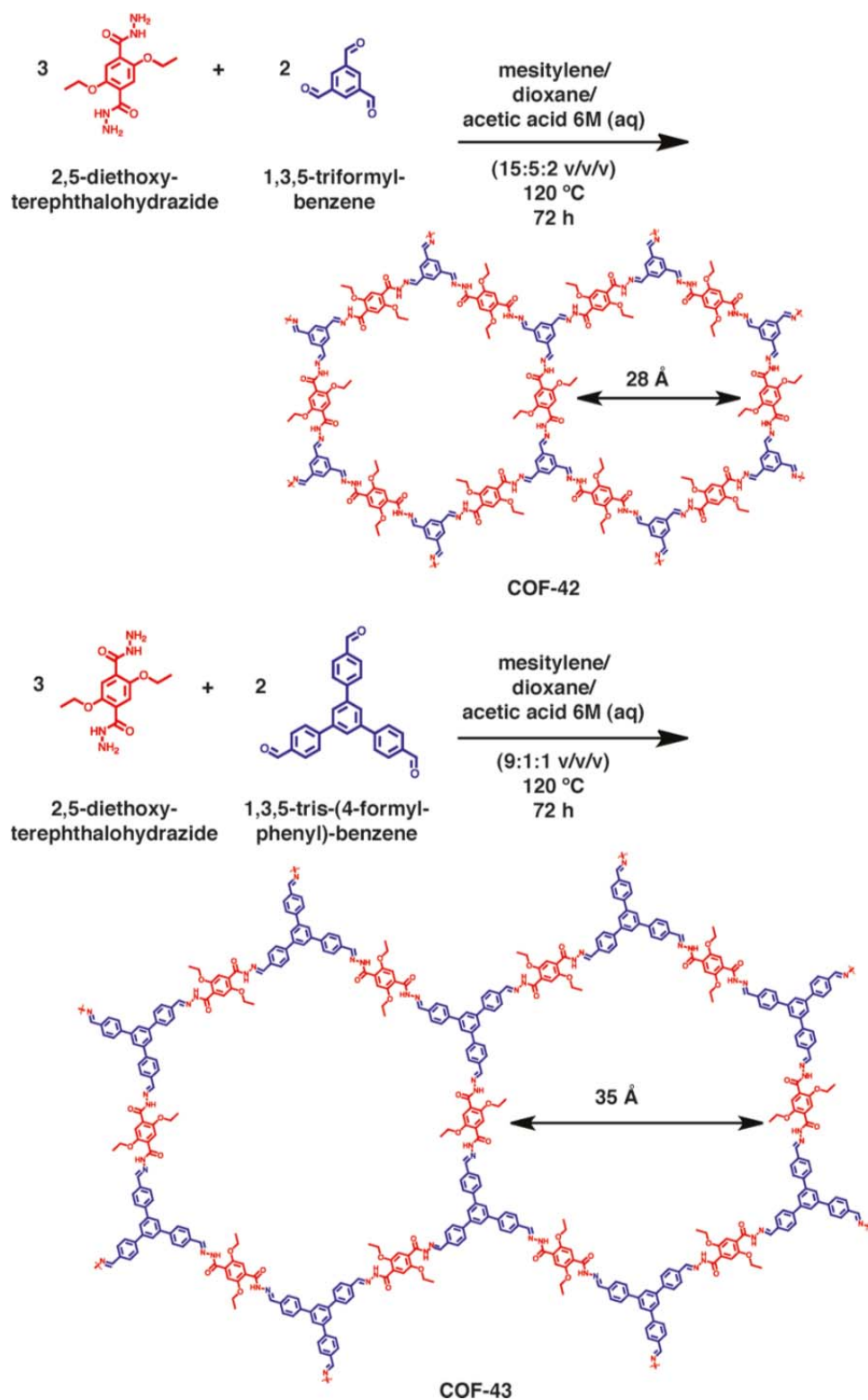


Figure 10. Synthesis of COF-42 and COF-43 by condensation of linear 2,5-diethoxyterephthalohydrazide building blocks (red) with trigonal-planar 1,3,5-triformylbenzene (blue) or 1,3,5-Tris(4-formylphenyl)benzene (Blue) to form COF-42 and COF-43 (cavity sizes are indicated).

In 2011, the Huisgen 1,3-dipolar cycloaddition reaction (“click” chemistry) also found its way into porous organic polymers (Figure 11).²⁷ These 1,3-dipolar cycloaddition “click” reactions of organic azides and terminal alkynes have had a strong impact on material sciences, especially polymer science. “Click” POP proved to be thermally stable and showed excellent resistance to strongly acidic and basic conditions. Its N_2 and H_2 adsorption capacities are $1260\text{ m}^2\text{ g}^{-1}$ and 1.6 wt% at 77 K and 1 bar are comparable with metal and covalent organic frameworks with similar surface areas.

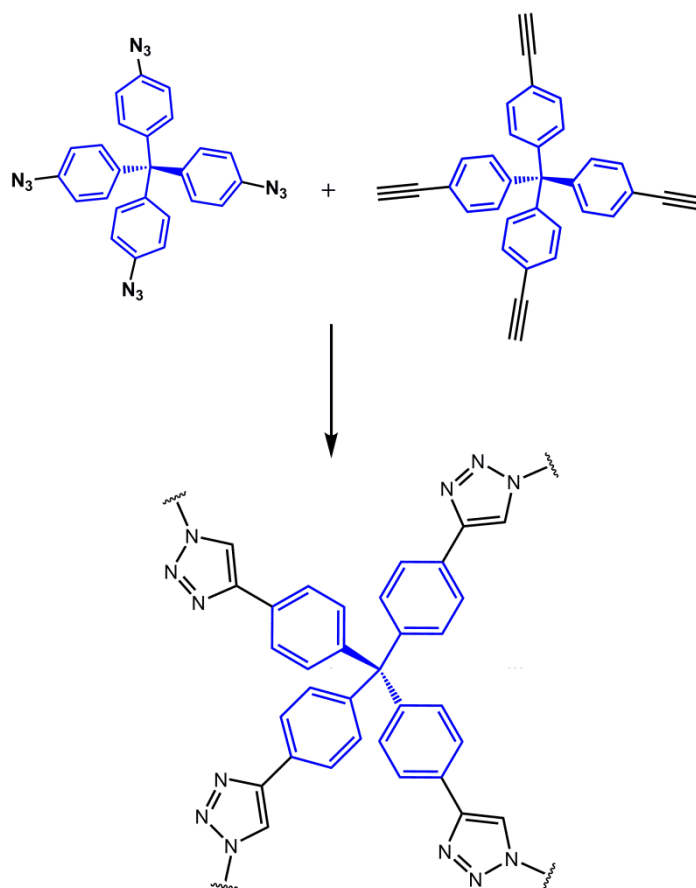


Figure 11. Top: synthesis of “click-based” POP from monomers using copper-catalyzed alkyne–azide coupling.

In 2011, Rabbani *et al* prepared a series of benzimidazole-linked polymers (BILPs) featuring high surface areas and amine functionalized pore walls and their performance in CO_2 removal from natural gas or flue-gas were evaluated (Figure 12).¹¹ Their studies show that the efficiencies of BILPs in

CO₂ removal from CH₄ depends upon the pore metrics and surface chemical functionalization. The high CO₂/CH₄ selectivities in the range of 8.0-17 and the high surface areas of BILPs make them attractive for use in natural gas purification applications.

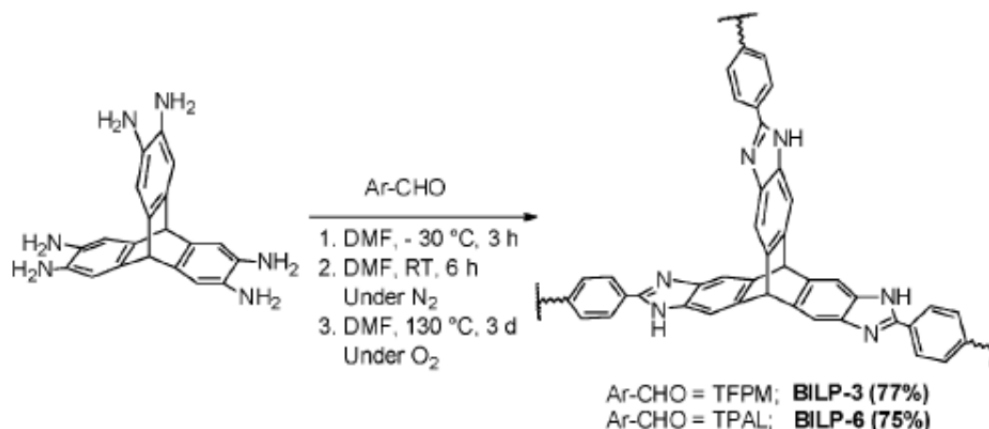


Figure 12. Synthesis of BILP-3 and BILP-6.

1.3 Metal Organic Frameworks (MOFs)

Crystal engineering involves the design and development of new porous single crystalline materials called metal organic frameworks (MOFs).⁵¹⁻⁶⁰ MOFs can be built from multi-dentate organic ligands such as carboxylates, and pyridines linked to metal ions or clusters or struts. Kitagawa and co-workers reported the first example of reversible gas uptake in a MOF called [Co₂(bipy)₃(NO₃)₄]_n in 1997.⁶¹ In 1999, Yaghi and co-workers achieved the synthesis of highly porous MOF-5 [Zn₄O(bdc)₃]_n.⁶² These two major breakthroughs revolutionized the field of MOFs. The porous nature of these materials makes them useful in heterogeneous catalysis, gas storage and in materials chemistry. MOFs with exceptionally large surface areas have been prepared with permanent porosities. MOFs can be designed and synthesized by systematic modification of the organic building blocks and the inorganic building units called secondary building units (SBUs) and by varying reaction conditions such as solvents (DMF, DEF, etc.) and temperatures.⁶³⁻⁶⁵ Metal-carboxylate clusters are well-known in inorganic chemistry, which serve as the basis to predict the structural geometries of MOFs.

SBU are the inorganic clusters that are linked together by the organic components to form the product framework.⁶⁶⁻⁶⁷ Examples of some SBUs that are commonly encountered in metal carboxylate MOFs are illustrated in Figure 15. These are: “dinuclear” cluster or the square “paddlewheel” with two terminal ligand sites [tetrakis(4-carboxyphenyl)porphyrin], the “tetranuclear” cluster or octahedral “basic zinc acetate” cluster [tetrahedral adamantane-1,3,5,7-tetracarboxylic acid] and the “trinuclear” cluster or the trigonal prismatic oxo-centered trimer, with three terminal ligand sites [trigonal 1,3,5-tris(4-carboxyphenyl)benzene]. These linkages are formed *in-situ* under specific synthetic conditions, and the geometry of the utilized linker can be used to predict the network topology of the corresponding MOF that is feasible within certain constraints. The success of an SBU in the design of an open framework relies both on its rigidity and directionality of bonding, which must be reliably maintained during the assembly process.

MOF-5 synthesized from a solution of $\text{Zn}(\text{NO}_3)_2 \cdot 6\text{H}_2\text{O}$ and benzene-1,4-dicarboxylic acid in *N,N'*-dimethylformamide, which generates $\text{Zn}_4\text{O}(\text{CO}_2)_6$ octahedral clusters *in situ*, which is a basic zinc acetate structure, with an oxide and four zinc centers that are tetrahedral, bridged by six terephthalate carboxylate linkers or struts forming the cubic structure based on the *pcu* net. This highly crystalline material is stable, up to 400 °C, and remarkably, solvent free single crystals maintain their diffraction quality even after heating to 300 °C. The solvent molecules in the pores of the as synthesized material can be exchanged with chloroform to remove unreacted linkers, metal salts, and the original solvent (DMF) from the pores. Chloroform is then removed under vacuum, and the resulting framework does not lose any weight. The resulting material has very high stability, up to about 500 °C. The surface area measured for MOF-5 was initially 2,900 m²/g, but now a value of 3,800 m²/g can be obtained from activated and evacuated samples of MOF-5.

After exploration of MOF-5, several MOFs with exceptionally large surface areas have been prepared with permanent porosity for H₂ and CH₄ storage and for CO₂ capture applications. The highest surface areas reported to date are over 6000 m²/g. Another application of MOFs results from decorating the pore surfaces with redox-active metal centers for energy storage and catalysis. For these applications, porphyrins are chosen as molecular building blocks to build nano, micro and mesoporous materials. These structures have been extensively studied over the past several decades in materials science. Many interesting properties of these porphyrins arise from the metals coordinated to the porphyrins. In 2009, Choe and co-workers successfully prepared a series of crystalline 2D/3D metal-organic frameworks with fascinating topologies, built from paddlewheel clusters and porphyrins. These solids are referred to as porphyrin paddlewheel frameworks (PPFs).⁶⁸⁻⁶⁹ Interestingly, these PPFs have large void spaces with channel sizes up to ca. 2nm (Figure 17). The topologies of PPFs can be systematically controlled by the coordination chemistry of the metal centers in the porphyrins and the length of bis-pyridyl pillars.

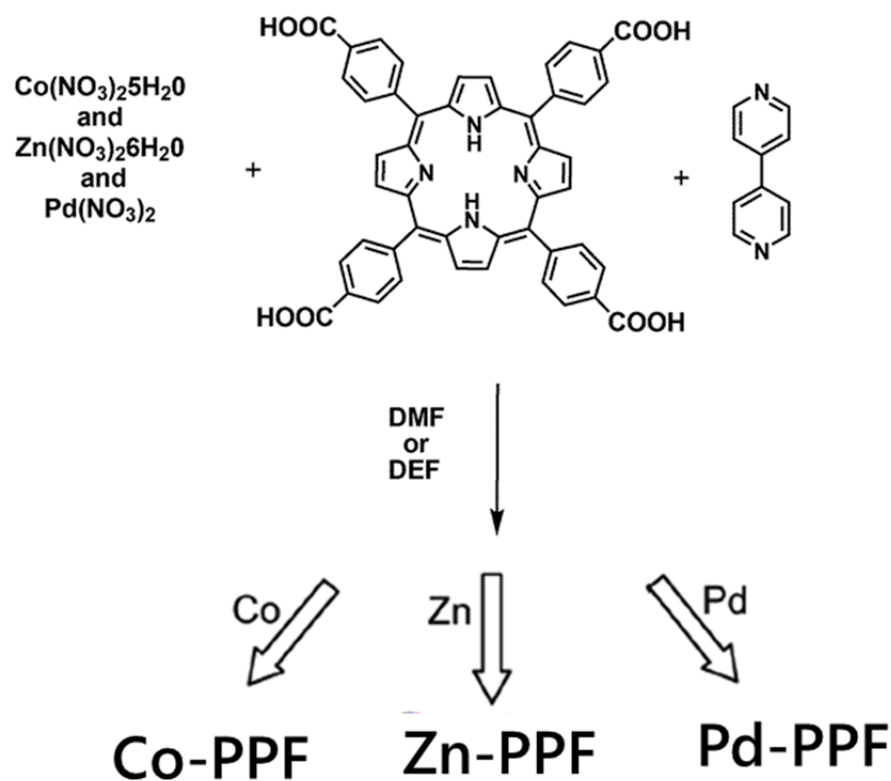


Figure 17. Synthesis of porphyrin paddlewheel metal organic frameworks.

Hupp and co-workers also developed porphyrin-based MOFs containing a variety of transition metal atoms for catalysis and light harvesting applications.⁷⁰⁻⁷¹ These porphyrin-based materials are providing important understanding in areas such as gas storage, heterogeneous catalysis, and chemical sensors.

There are only a few experimental reports of MOFs encapsulating C_{60} either acting as pillars or trapped inside the pores. In 2001, Sun *et al* reported the first example of a porphyrin MOF synthesis in the presence of C_{60} , which led to a porphyrin MOF with C_{60} pillars.⁷² They described that there is no necessity to pair a concave host with a convex guest. Another *in-situ* study described the growth of crystals in the presence of C_{60} during the assembly of a 2-dimensional network containing octahedral $\text{trans-NiCl}_2\text{N}_4$ nodes in which the nitrogen donors are provided by 4'-tert-butyl-4,2':6'4"-terpyridine. In the absence of the fullerene, the coordination network comprises [4 + 4] macrocycles connected by

trans-[NiCl₂N₄] nodes.⁷⁴ The presence of C₆₀ favors the assembly of [3 + 3] macrocycles which efficiently host the fullerenes and are connected into 2-dimensional sheets through *trans*-[NiCl₂N₄] nodes and fullerene-free [6 + 6] macrocycles.

A second example of C₆₀ incorporation was reported by Yaghi *et al* using MOF-177. Due to the stability and large porosity of MOF-177, they tested its ability to adsorb large organic molecules. MOF-177 crystals were placed into a C₆₀-toluene solution. Even several days the crystals shape and integrity remain unchanged and a change in color was observed to deep red provided optical evidence of C₆₀ inclusion into the MOF-177.⁷³ Metal-organic frameworks (MOFs) are currently attracting considerable attention for a variety of sensing applications. They are ideal candidates because they have tailorable porosity and ultrahigh surface areas. The organic linkers can consist of a variety of functional molecules, including fluorophores. Toward that goal, two groups of researchers have shown how molecular sieving can be used for size selective sensing in luminescent Zn₃btc₂ (btc = benzenetricarboxylate).⁷⁵⁻⁷⁷ Following exposure to amines of different sizes, a decrease in the fluorescence was observed for amines that were small enough to easily diffuse into the MOF pores, including ethylamine, dimethylamine, and propylamine. In contrast, aniline and butylamine showed no quenching, presumably due to size exclusion.

A similar size-selective effect has been observed for a Cd²⁺-based MOF.⁷⁸ Introduction of various anions revealed that only nitrite quenches the luminescence. While the investigators speculated that energy transfer to (-NO₂) through strut-based C-H bonds that purportedly engage in hydrogen bonding with nitrite ions, a more plausible mechanism is the reductive quenching of the highly energetic excited state by the nitrite. Linker-based fluorescence is common due to the fact that many MOFs contain conjugated ligands that absorb in the visible or UV, together with d¹⁰ metal ions such Zn(II) or

Cd(II) (largely electronically inert ions). Recently, Lan and co-workers reported two fluorescent Zn-based MOFs capable of sensing nitro-containing molecules, which is potentially useful for the detection of explosives.⁷⁹⁻⁸⁰ Detection of hazardous materials is a significant concern for homeland security, and portable sensors are potentially desirable to circumvent the complexity sometimes associated with traditional analytical methods. In the case of explosives, identification can be accomplished by detecting a byproduct or an additive when the explosive itself is not readily detectable (e.g., due to low vapor pressure). $\text{Zn}_2(\text{bpdc})_2\text{bpee}$ (bpdc = 4,40-biphenyldicarboxylate; bpee = 1,2- bipyridylethene), a MOF containing a linker with the potential to fluoresce, was screened for the detection of 1,4-dinitrotoluene (DNT), which is a byproduct during the formation of 2,4,6-trinitrotoluene (TNT) and 2,3-dimethyl-2,3-dinitrobutane (DMNB). The latter is an additive used to facilitate detection of plastic explosives. In its solvent-evacuated state, the MOF shows an emission band centered at 420 nm. Upon exposure to 0.18 ppm DNT or 2.7 ppm DMNB, the emission red shifts and decreases in intensity due to electron transfer from the struts to DNT and DMNB guests. The fluorescence quenching efficiency saturates at 85% for DNT and 84% for DMNB, within 10s. The quenching efficiency is defined as $(I_0 - I) / I_0 \times 100\%$, where I_0 is the intensity before exposure, and I is the intensity following exposure. Remarkably, this sensor exhibits sensitivity comparable to those of conjugated polymer films for the detection of DNT and outperforms them in terms of response time. In addition, this sensor displays unparalleled sensitivity to DMNB, which is notoriously difficult to detect, possibly due to poor π - π interactions and consequent weak binding. Importantly, both analytes adsorb semireversibly that is, the initial fluorescence is recoverable by heating to 150°C. More recently, the same group measured the quenching effect of various substituted aromatics on $[\text{Zn}_2(\text{oba})_2(\text{bpy})]_3 \text{DMA}$ [H_2Oba = 4,40-oxybis(benzoic acid); bpy = 4,40-bipyridine; DMA = N,N'-dimethylacetamide].⁸⁰ This pillared paddle-wheel MOF emits at 420 nm. When exposed to a range of nitroaromatic analytes, it was found that all nitro-containing molecules quench the fluorescence to varying degrees. The quenching efficiency increased in the order $\text{DNT} < \text{p-}$

dinitrobenzene \approx nitrotoluene < m-dinitrobenzene < nitrobenzene. This trend was rationalized on the basis of both the electron-withdrawing ability of the analyte and its vapor pressure. The dinitrobenzenes are highly electron deficient and therefore should be good oxidative quenchers, but they have low vapor pressures. Nitrobenzene has a higher quenching efficiency (despite having one fewer NO₂ group) presumably because of its relatively high vapor pressure. The nitrotoluenes are less electron-deficient due to the electron-donating methyl substituents, so they quench less efficiently.

References

- 1) A. P. Côté, A. I. Benin, N. W. Ockwig, M. O’Keeffe, A. J. Matzger and O. M. Yaghi, *Science.*, 2005, **310**, 1166.
- 2) R. W. Tilford, W. R. Gemmill, H.-C. zur Loye and J. J. Lavigne, *Chem. Mater.*, 2006, **18**, 5296
- 3) A. P. Côté, H. M. El-Kaderi, H. Furukawa, J. R. Hunt and O. M. Yaghi, *J. Am. Chem. Soc.*, 2007, **129**, 12914
- 4) H. M. El-Kaderi, J. R. Hunt, J. L. Mendoza-Cortes, A. P. Côté, R. E. Taylor, M. O’Keeffe and O. M. Yaghi, *Science.*, 2007, **316**, 268
- 5) J. R. Hunt, C. J. Doonan, J. D. LeVangie, A. P. Côté and O. M. Yaghi, *J. Am. Chem. Soc.*, 2008, **130**, 11872
- 6) P. Kuhn, M. Antonietti and A. Thomas, *Angew. Chem., Int. Ed.*, 2008, **47**, 3450
- 7) F. J. Uribe-Romo, J. R. Hunt, H. Furukawa, C. Klöck, M. O’Keeffe and O. M. Yaghi, *J. Am. Chem. Soc.*, 2009, **131**, 4570
- 8) E. L. Spitler and W. R. Dichtel, *Nat. Chem.*, **2010**, *2*, 672
- 9) F. J. Uribe-Romo, C. J. Doonan, H. Furukawa, K. Oisaki and O. M. Yaghi, *J. Am. Chem. Soc.*, 2011, **133**, 11478
- 10) M. Dogru, A. Sonnauer, A. Gavryushin, P. Knochel and T. Bein, *Chem. Commun.*, 2011, **47**, 1707

- 11) K. T. Jackson, T. E. Reich and H. M. El-Kaderi, *Chem. Commun.*, 2012, **48**, 8823
- 12) E. L. Spitler, J. W. Colson, F. J. Uribe-Romo, A. R. Woll, M. R. Giovino, A. Saldivar, and W. R. Dichtel, *Angew. Chem., Int. Ed.*, 2012, **51**, 2623
- 13) D. N. Bunck and W. R. Dichtel, *Angew. Chem., Int. Ed.*, 2012, **51**, 1855.
- 14) H. Furukawa and O. M. Yaghi, *J. Am. Chem. Soc.*, 2009, **131**, 8875.
- 15) S. B. Kalidindi, H. Oh, M. Hirscher, D. Esken, C. Wiktor, S. Turner, G.V. Tendeloo, and R. A. Fischer, *Chem. Eur. J.*, 2012, **18**, 10848
- 16) J. L. Mendoza-Cortes, W. A. Goddard, H. Furukawa and O. M. Yaghi, *J. Phys. Chem. Letts.*, 2012, **3**, 2671
- 17) C. J. Doonan, D. J. Tranchemontagne, T. G. Glover, J. R. Hunt, O. M. Yaghi, *Nature Chem.*, **2010**, **2**, 235
- 18) S.-Y. Ding, J. Gao, Q. Wang, Y. Zhang, W.-G. Song, C.-Y. Su and W. Wang, *J. Am. Chem. Soc.*, 2011, **133**, 19816
- 19) S. Wan, J. Guo, J. Kim, H. Ihee and D. Jiang, *Angew. Chem., Int. Ed.*, 2008, **46**, 8826
- 20) S. Wan, J. Guo, J. Kim, H. Ihee and D. Jiang, *Angew. Chem., Int. Ed.*, 2009, **48**, 5439
- 21) S. Wan, F. Gándara, A. Asano, H. Furukawa, A. Saeki, S. K. Dey, L. Liao, M. W. Ambrogio, Y. Y. Botros, X. F. Duan, S. Seki, J. F. Stoddart and O. M. Yaghi, *Chem. Mater.*, 2011, **23**, 4094
- 22) J. W. Colson, A. R. Woll, A. Mukherjee, M. P. Levendorf, E. L. Spitler, V. B. Shields, M. G. Spencer, J. Park, and W. R. Dichtel, *Science.*, 2011, **332**, 228
- 23) X. Ding, X. Feng, A. Saeki, S. Seki, A. Nagai and D. Jiang, *Chem. Commun.*, 2012, **48**, 8952
- 24) X. Ding, J. Guo, X. Feng, Y. Honsho, J. Guo, S. Seki, P. Maitrad, A. Saeki, S. Nagase, and D. Jiang, *Angew. Chem., Int. Ed.*, 2011, **50**, 1289
- 25) M. Dogru, M. Handloser, F. Auras, T. Kunz, D. Medina, A. Hartschuh, P. Knochel, T. Bein, *Angew. Chem.* 2013, **52** 2920

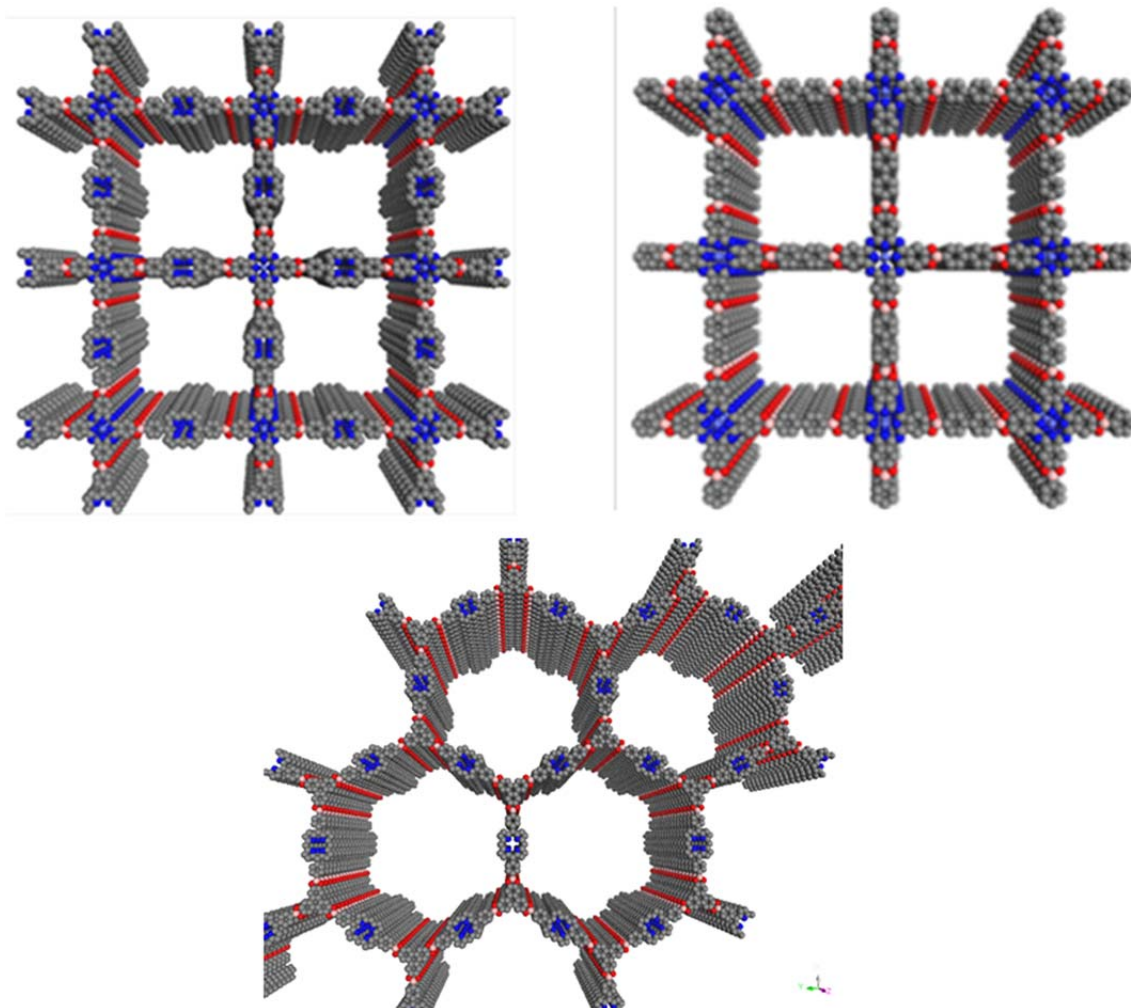
- 26) A. Thomas, *et al. Angew. Chem., Int. Ed.*, 2010, **49**, 8328
- 27) R. Dawson, A. I. Cooper, D. J. Adams, *Prog. Polym. Sci.*, 2012, **37**, 530
- 28) N. Y. Du, *et al. Nat. Mater.*, 2011, **10**, 372
- 29) S. Kitagawa, R. Kitaura, S. Noro, *Angew. Chem., Int. Ed.*, 2004, **43**, 2334
- 30) G. Ferey, *Chem. Soc. Rev.*, 2008, **37**, 191
- 31) O. M. Yaghi, *et al. Nature.*, 2003, **423**, 705
- 32) S. Xiang, *et al. Nat. Commun.*, 2012, **3**, 1
- 33) A. P. Cote, *et al. Science.*, 2005, **310**, 1166
- 34) P. M. Budd, *et al. Chem. Commun.*, 2004, 230
- 35) P. Kaur, J. T. Hupp, and S. T. Nguyen, *ACS Catal.*, 2011, **1**, 819
- 36) H. Y. Zhao, *et al. Chem. Commun.*, 2011, **47**, 6389
- 37) S. Wan, *et al. Chem. Mater.*, 2011, **23**, 4094
- 38) J. X. Jiang, A. Trewin, D. J. Adams, and A. I. Cooper, *Chem. Sci.*, 2011, **2**, 1777
- 39) H. M. El-Kaderi, *et al. Science.*, 2007, **316**, 268
- 40) N. B. McKeown, P. M. Budd, *Macromolecules.*, 2010, **43**, 5163
- 41) C. D. Wood, *et al. Chem. Mater.*, 2007, **19**, 2034
- 42) J. X. Jiang, *et al. Angew. Chem., Int. Ed.*, 2007, **46**, 8574
- 43) M. G. Schwab, *et al. J. Am. Chem. Soc.*, 2009, **131**, 7216
- 44) T. Ben, *et al. Angew. Chem., Int. Ed.*, 2009, **48**, 9457
- 45) D. Q. Yuan, W. G. Lu, D. Zhao, and H. C. Zhou, *Adv. Mater.*, 2011, **23**, 3723
- 46) A. P. Katsoulidis, M. G. Kanatzidis, *Chem. Mater.*, 2011, **23**, 1818
- 47) M. G. Rabbani, T. E. Reich, R. M. Kassab, K. T. Jackson, and H. M. El-Kaderi, *Chem. Commun.*, 2012, **48**, 1141
- 48) M. Rose, W. Bohlmann, M. Sabo, S. Kaskel, *Chem. Commun.*, 2008, 2462

- 49) P. Mohanty, L. D. Kull, and K. Landskron, *Nat. Commun.*, 2011, **2**, 401
- 50) H. A. Patel, *et al. J. Mater. Chem.*, 2012, **22**, 8431
- 51) O. M. Yaghi, H. Li, *J. Am. Chem. Soc.*, 1995, **117**, 10401
- 52) H. Li, M. Eddaoudi, T. L. Groy, O. M. Yaghi, *J. Am. Chem. Soc.*, 1998, **120**, 8571
- 53) H. Li, M. Eddaoudi, M. O’Keeffe, O. M. Yaghi, *Nature.*, 1999, **402**, 276
- 54) M. Eddaoudi, *et al. Science.*, 2002, **295**, 469
- 55) O. M. Yaghi, *et al. Nature.*, 2003, **423**, 705
- 56) J. L. C. Rowsell, E. C. Spencer, J. Eckert, J. A. K. Howard, O. M. Yaghi, *Science.*, 2005, **309**, 1350
- 57) H. Furukawa, *et al. Science.*, 2010, **329**, 424
- 58) O. K. Farha, *et al. Nat. Chem.*, 2010, **2**, 944
- 59) O. K. Farha, *et al. J. Am. Chem. Soc.*, 2012, **134**, 9860
- 60) O. K. Farha, *et al. J. Am. Chem. Soc.*, 2012, **134**, 15016
- 61) M. Kondo, T. Yoshitomi, H. Matsuzaka, S. Kitagawa, K. Seki, *Angew. Chem., Int. Ed.*, 1997, **36**, 1725
- 62) H. Li, M. Eddaoudi, M. O’Keeffe, O. M. Yaghi, *Nature.*, 1999, **402**, 276
- 63) B. Chen, *et al. J. Am. Chem. Soc.*, 2000, **122**, 11559
- 64) Z. Wang, S. M. Cohen, *J. Am. Chem. Soc.*, 2007, **129**, 12368
- 65) H. Furukawa, *et al. Inorg. Chem.*, 2011, **50**, 9147
- 66) M. O’Keeffe, M. A. Peskov, S. J. Ramsden, O. M. Yaghi, *Acc. Chem. Res.*, 2008, **41**, 1782
- 67) O. M. Yaghi, Q. Li, *MRS Bulletin.*, 2009, **34**, 682
- 68) E-Y. Choi, P. M. Barron, R. W. Novotny, H-T. Son, C. Hu, W. Choe, *Inorg. Chem.*, 2009, **48**, 426
- 69) H. Chung, P. M. Barron, R. W. Novotny, H-T. Son, C. Hu, W. Choe, *Cryst. Growth Des.*, 2009, **9**, 3327.

- 70) O. K. Farha, A. M. Shultz, A. A. Sarjeant, S. T. Nguyen, and J. T. Hupp, *J. Am. Chem. Soc.*, 2011, **133**, 5652
- 71) C. Y. Lee, O. K. Farha, B. J. Hong, A. A. Sarjeant, S. T. Nguyen, and Joseph T. Hupp, *J. Am. Chem. Soc.*, 2011, **133**, 15858
- 72) D. Sun, F. S. Tham, C. A. Reed, P. D. W. Boyd, *Proc. Natl. Acad. Sci. USA.*, 2002, **99**, 5088
- 73) H. K. Chae, D. Y. Siberio-Perez, J. Kim, Y.-B. Go, M. Eddaoudi, A. J. Matzger, M. O'Keeffe, O. M. Yaghi, *Nature.*, 2004, **427**, 523
- 74) E. C. Constable, G. Zhang, C. E. Housecroft, J. A. Zampese, *CrystEngComm.*, 2012, **14**, 1770
- 75) L-G. Qiu, Z-Q. Li, Y. Wu, W. Wang, T. Xu, X. Jiang, *Chem. Commun.*, 2008, 3642.
- 76) X. Zou, G. Zhu, I. J. Hewitt, F. Sun, S. Qiu, *Dalton Trans.*, 2009, 3009.
- 77) Y. Qiu, H. Deng, J. Mou, S. Yang, M. Zeller, S. R. Batten, H. Wu, J. Li, *Chem. Commun.*, 2009, 5415.
- 78) L. B-Desmonts, D. N. Reinhoudt, M. Crego-Calama, *Chem. Soc. Rev.*, 2007, **36**, 993.
- 79) A. Lan, K. Li, H. Wu, D. H. Olson, T. J. Emge, W. Ki, M. Hong, and J. Li, *Angew. Chem., Int. Ed.*, 2009, **48**, 2334.
- 80) S. Pramanik, C. Zheng, X. Zhang, T. J. Emge, and J. Li, *J. Am. Chem. Soc.*, 2011, **133**, 4153.

Chapter 2

Impact of pore size on H₂ adsorption of covalent organic frameworks



Introduction

Recently, there has been significant interest in the development of covalent organic frameworks (COFs) for applications related to the storage of hydrogen and methane. Research in this area is highly challenging due to the fact that hydrogen has a very low gravimetric and volumetric density. Thus, all existing H₂ storage methods have various difficulties that must be overcome before large-scale commercialization can be considered.¹⁻⁵ Because of this, the development of new storage materials that can also increase the amount of hydrogen stored is imperative.

Hydrogen is the most abundant element in the universe and has great potential to become one of the dominant energy sources in the future. The problem is how to pack hydrogen into a 2D COF as small as possible without using excessive high pressure or very low temperatures. Recently, Pd@COF-102 (9.5wt%) and PdCl₂@COF-301 (4.2wt%) were shown to possess higher H₂ storage properties at 298K than the metal-free COF-102 (5.2wt%) and COF-301 (0.44wt%) by themselves.⁶⁻⁸ Using density functional theory (DFT) calculations it was also shown that lithium-doped free base phthalocyanine COF (5.3wt%)⁹ and lithium-doped fullerene intercalated 2D layered free base phthalocyanine COFs (12wt%)¹⁰ should exhibit superior H₂ storage capabilities at 77K and 298K at 100bar compared to lithium-free (3.7wt%) and Li@fullerene free phthalocyanine COFs (4.2wt%). Iron containing nanoporous porphyrin polymers with high surface areas were also shown to possess high H₂ storage capacities when compared to free-base porphyrin polymers due to the presence of metal-hydrogen interactions in the former (5wt%).¹¹ Although 2D layered COFs show lower H₂ storage capacities when compared to 3D COFs,¹² metallated phthalocyanine based 2D COFs have the advantage of hosting a variety of metals in the core of the phthalocyanines. Phthalocyanines are ubiquitous in many applications such as in liquid crystals, luminescent devices, and organic light emitting diodes¹³ (OLED's), mainly due to their stability, planarity, and rigidity. Phthalocyanines can also bind a wide variety of metals such as Pd, Fe, Co etc. Incorporation of these transition metal ions into the core of the

phthalocyanine should increase the hydrogen storage capacities of metallated phthalocyanine COFs due to the presence of metal--H₂ interactions. A few metallophthalocyanine COFs have been reported with Zn, Ni, or Co central ions, but the hydrogen and methane storage properties at low pressures have not been reported.¹⁴⁻¹⁶ Thus, we have chosen to investigate the H₂ and CH₄ storage properties of a cobalt based phthalocyanine COF at both low pressure and at varied temperatures. This has led us to explore cobalt phthalocyanine COFs containing perfectly ordered channels that allow H₂ to effectively access the interior space for efficient H₂ storage materials.¹⁷⁻¹⁹

The current chapter is focused on the rational design and synthesis of three novel COFs using phthalocyanine or porphyrin building blocks connected through boronate ester linkages. The studies are based on a synthetic strategy to achieve materials containing macrocycles such as 5, 15 phenyldiboronic acid porphyrin (PorDBA), combined with octahydroxy phthalocyanine Co(II) (CoPc) and hexahydroxytriphenylene (HHTP) and 4,4'-biphenyldiboronic acid (BPDA) linkers. The linker length affects the pore sizes and volumes of the frameworks depending on the incorporated boronic acid or hydroxyl moieties. The CoPc-BPDA and CoPc-PorDBA COFs were observed having square shaped pore sizes in a **sql** topology²⁰ using the space group *P4/mmm*. These two COFs were constructed from the dehydration reaction between octahydroxyphthalocyanine Co(II) and 5, 15 dihydroxyboryl porphine building blocks (CoPc-PorDBA, Scheme 5) and octahydroxyphthalocyanine and 4,4'-biphenyldiboronic acid (CoPc-BPDA, Scheme 6). HHTP-PorDBA COF with 5.2nm wide hexagonal pore size was synthesized from HHTP and PorDBA (Scheme 7). The hexagonal pore size and **hnn** topology has a space group *P6/mmm* differing from that of the square shaped phthalocyanine COFs.

The syntheses of CoPc-PorDBA, CoPc-BPDA, and HHTP-PorDBA COFs were carried out solvothermally in a mixture of dimethylacetamide and o-dichlorobenzene (2/1 v/v), whereas the HHTP-PorDBA COF was synthesized in a mixture of mesitylene and dioxane (1/1 v/v) in sealed glass ampoules at 120 °C for 72 h. The chemical connectivity and composition of all the COFs presented here were characterized by several methods such as Fourier-Transform infrared spectroscopy (FT-IR), solid-

state ^{11}B and ^{13}C CP-MAS NMR, powder X-ray diffraction (PXRD), BET surface area measurements, scanning electronic microscopy (SEM), Cryo-electron microscopy, diffuse reflectance UV-Vis, and elemental analysis.

Experimental Methods

All chemicals and solvents were purchased from Sigma-Aldrich or Alfa Aesar and used without further purification otherwise noted. Fourier transform infrared (FT-IR) spectra were recorded on a Perkin-Elmer Spectrum One infrared spectrometer (ATR). ^1H NMR spectra were recorded on JEOL 600MHz spectrometer, where chemical shifts (δ in ppm) were determined with a residual proton of the solvent as standard. Matrix-assisted laser desorption ionization time-of-flight mass spectra (MALDI-TOF MS) were recorded on Bruker benchtop microflex model using trihydroxyanthracene as the matrix. Field-emission scanning electron microscopy (FE-SEM) was performed on a Hitachi S-4800 spectrometer fitted with an EDAX energy-dispersive spectrometry system by adhering sample on a sampling platform. Powder X-ray diffraction (PXRD) data were recorded on a Bruker Discover D8 model diffractometer by depositing powder on a plastic substrate, from $2\theta = 1^\circ$ up to 30° with a 0.05° increment. In order to determine pore textural properties including the specific Brunauer–Emmet–Teller (BET) surface area, pore volumes and size distributions, nitrogen adsorptions and desorption isotherms on CoPc-PorDBA, CoPc-BPDA, and HHTP-PorDBA COF samples were measured at 77 K on an ASAP-2020 adsorption apparatus (Micromeritics). Thoroughly washed samples were degassed in situ at 150°C with a heating rate of $3^\circ\text{C}/\text{min}$ under a vacuum (0.0001 mmHg) for 12 h before nitrogen adsorption measurements in order to ensure the micro-channels of the structure were guest-free. The Brunauer-Emmett-Teller (BET) method was utilized to calculate the specific surface areas by using the non-local density functional theory (NLDFT) model, and the pore volume was derived from the sorption

curve. Thermogravimetric analysis from 30-700°C was carried out on a Mettler-Toledo thermogravimetric analyzer in an N₂ atmosphere using a 3°C/min ramp time.

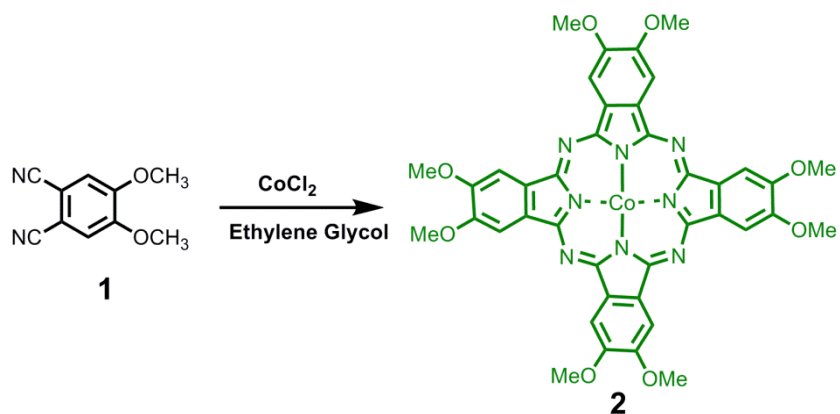
2. Synthesis and characterization of precursors of CoPc-PorDBA COF

Synthesis of 4,5-Dimethoxyphthalodinitrile (1)

1,2-Dibromo-4,5-dimethoxybenzene (8.87 g, 0.03 mol) was heated under reflux (bath temperature 165°C) for 5 h with 8.06 g (0.09 mol) of CuCN in 120 mL of DMF. After being cooled, the reaction mixture was stirred in 300 mL of concentrated ammonium hydroxide and air was led through the solution for a period of 12 h. The blue solution was suction filtered (sintered glass), and the solid residue was washed with a little dilute ammonium hydroxide and then with copious amounts of water until the filtrates were neutral. The dry, crude olive-green product was placed in the thimble of a Soxhlet extractor and extracted for 3 days with ether. The nitrile isolated from the ether was crystallized from methanol. Yield: 57%

Synthesis of 2,3,9,10,16,17,23,24-Octamethoxyphthalocyaninato)cobalt(II) (MeO)₈PcCo (2)

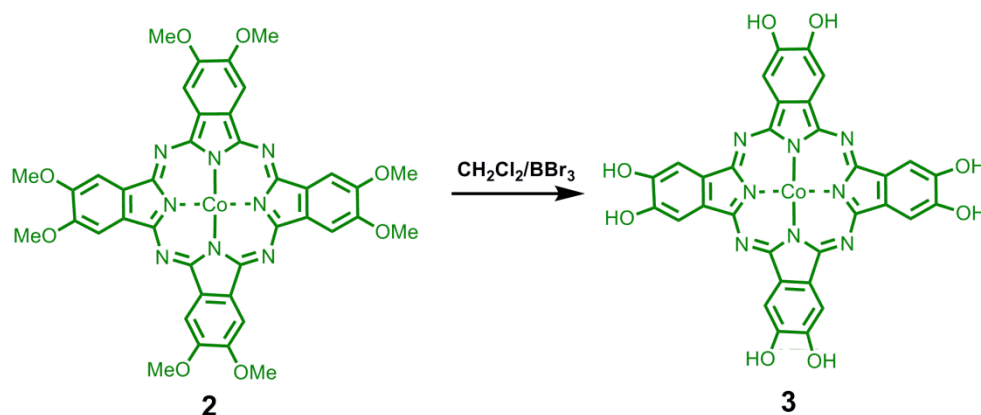
4,5-Dimethoxyphthalodinitrile(1, 13.77 g, 0.073 mol) and 1.5 g (0.012 mol) of cobalt(II) chloride were heated in 180 mL of ethylene glycol at 200°C for 5 h, after which the mixture was cooled somewhat, and an equal volume of water was added. The mixture was suction filtered while still hot, and the filtrate was washed with hot water. The crude product was boiled 2 h, first with 500 mL of 1 N HCl and then with 500 mL of 1 N NaOH, filtered, and washed with water each time until the filtrate was neutral. The solid material was then stirred in methanol, suction-filtered, and dried in vacuo 6 h at 60°C. (MeO)₈PcCo obtained as a green solid in 40% yield. MALDI-TOF MS for C₄₀H₃₂N₈O₈Co (Calculated 811.17), found $m/z = 811.87 [M]^+$.



Scheme 1. Synthesis of octamethoxy phthalocyanine Co(II) from dimethoxyphthalonitrile.

Synthesis of 2,3,9,10,16,17,23,24-Octahydroxyphthalocyaninato)cobalt(II) (OH)₈PcCo (3)

(MeO)₈CoPc (2, 142.0 mg, 0.175 mmol) was suspended in 10 mL of dichloromethane, and boron tribromide (0.68 mL, 7 mmol) was added under N₂ atmosphere. The mixture was stirred for 3 days, and 10 mL of methanol was added slowly. The solvent was removed, the residue was washed by methanol and centrifuged. After repeating the cycle of wash and centrifuge more than 3 times, the precipitate was collected and dried in vacuum, to give (OH)₈CoPc as a dark green solid in 70% yield. MALDI-TOF MS for C₃₂H₁₆N₈O₈Co (Calculated 699.04), found m/z = 698.99 [M]⁺.



Scheme 2. Synthesis of octahydroxy phthalocyanine Co(II) from octamethoxy phthalocyanine Co(II).

Synthesis of 2, 2'-dipyrromethane (4)

A mixture of paraformaldehyde (1.50 g, 50.0 mmol) and pyrrole (347 mL, 5.00 mol) in a 500-mL flask was degassed with a stream of argon for 10 min at room temperature. The mixture was heated at 55°C for about 10 min under argon to obtain a clear solution. InCl₃ (1.11 g, 5.00 mmol) was then added, and the mixture was stirred at 55°C for 2.5 h. The heat source was removed, and NaOH (6.0 g, 0.15 mol) was added. The mixture was stirred for 1 h and then filtered. The filtrate was concentrated, and the pyrrole was recovered. The crude solid obtained after removing pyrrole was extracted with 20% ethyl acetate/ hexanes (250 mL). The solvent was evaporated. Crystallization [methanol/water (4:1)] afforded pale white crystals. Yield: 45%. ¹H NMR (600 MHz, CDCl₃, 298K, δ = ppm, J = Hz): 7.72 (2H, br s), 6.64 (2H, m), 6.19 (2H, m), 6.08 (2H, m), 3.97 (2H, s).

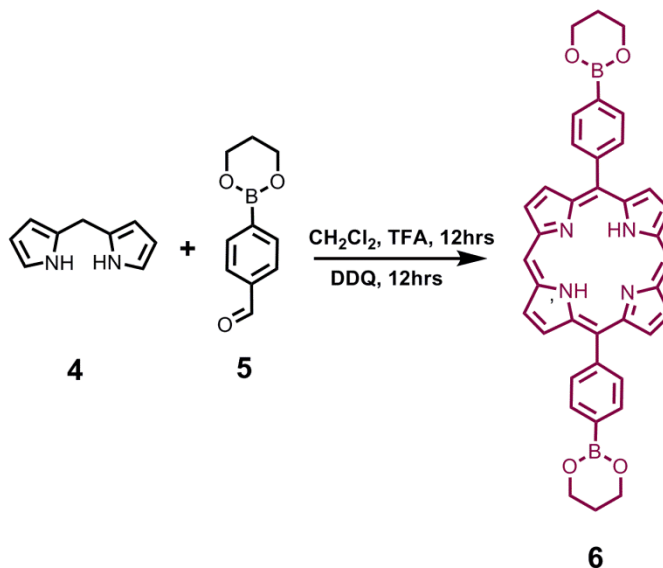
Synthesis of 4-(1,3-dioxaborinan-2-yl)benzaldehyde (5)

4-formyl boronic acid (0.750 g, 5 mmol) and 1,3-propanediol (0.380 g, 5 mmol) were heated at reflux for 12 h in toluene (100 mL) using a Dean-Stark equipment to remove water. The solvent was evaporated under reduced pressure to give a crude product as a white solid. The crude product was used in the next step without purification. ¹H NMR (600 MHz, CDCl₃) 10.03 (s, 1H), 7.91-7.84 (dd, J = 2.6, 7.6, 2H), 4.18 (t, J = 5.2 Hz, 4H), 2.08 (t, J = 5.6Hz, 2H).

Synthesis of 5, 15-bis(4-[1,3,2]-dioxaborinan-2-yl-phenyl)porphyrin (6)

4-(1,3-dioxaborinan-2-yl)benzaldehyde (**5**, 115 mg, 0.605 mmol), 2, 2'-dipyrromethane (**4**, 80 mg, 0.55 mmol) were dissolved in 100 mL of dry dichloromethane and then 50 μ l BF₃.Et₂O was added to the mixture and then the mixture was stirred for 12hrs at room temperature. To this reaction mixture was added chloranil (560 mg, 0.605 mmol). After evaporation of the solvent, the crude mixture was chromatographed (silica gel, CHCl₃) to produce 50 mg of 5,15-bis(4-[1,3,2]-dioxaborinan-2-yl-

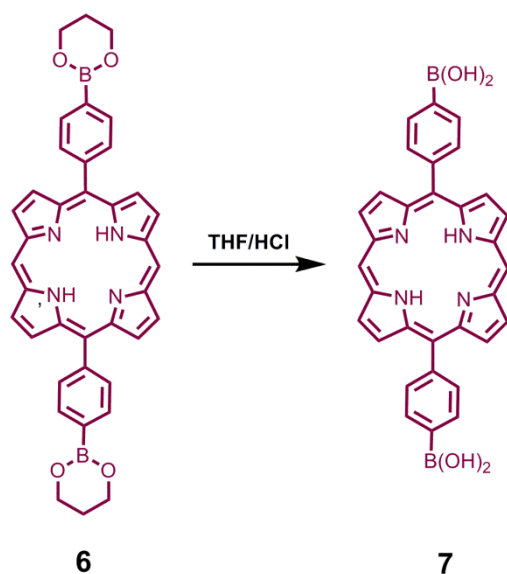
phenyl)porphyrin. Yield: 30%. ^1H NMR (600 MHz, CDCl_3 , 298K, δ = ppm, J = Hz): 2.25 (m, 4H), 4.37 (m, 8H), 8.21 (d, J = 7.8, 4H), 8.28 (d, J = 7.8, 4H), 9.08 (d, J = 4.6, 4H), 9.40 (d, J = 4.6, 4H), 10.3 (s, 2H). MALDI TOF-MS (THA): calcd. (Found) for $[\text{M}+\text{H}]^+$: 630.26 (631.46).



Scheme 3. Synthesis of 5, 15-bis(4-[1,3,2]-dioxaborinan-2-yl-phenyl)porphyrin from 4-(1,3-dioxaborinan-2-yl)benzaldehyde and 2, 2'-dipyrrromethane.

Synthesis of 5, 15-bis[(dihydroxyboryl)phenyl]-21H,23H-porphine (7)

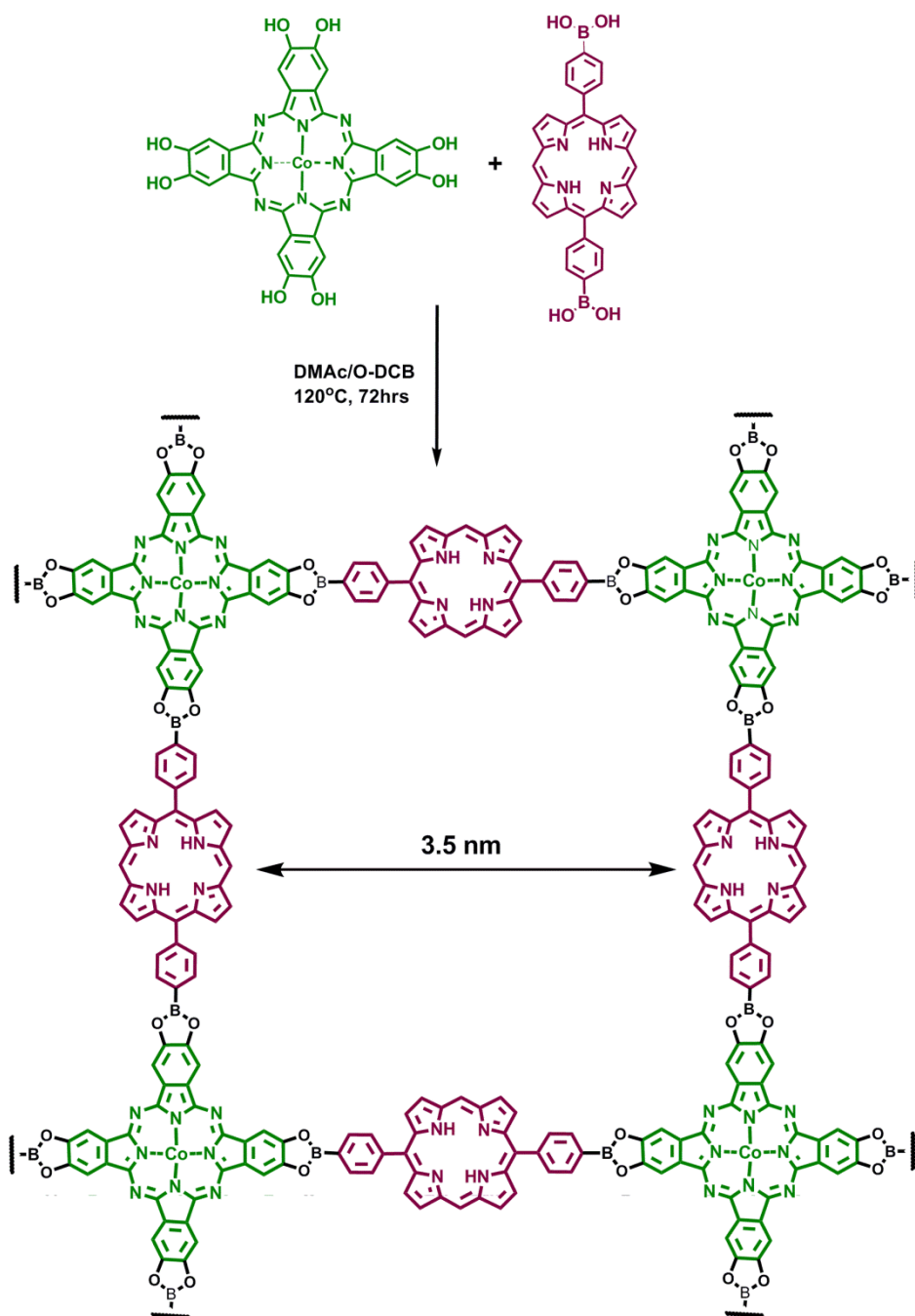
5, 15-bis(4-[1,3,2]-dioxaborinan-2-yl-phenyl)porphyrin (100 mg) was dissolved in THF (100 mL), an aqueous solution of HCl (pH = 1.0, 100 mL) was added to the mixture. The mixture was stirred at r.t for 24 hrs. Dichloromethane (100 mL) was added to the mixture, and the organic layer was washed with aqueous saturated solution of NaHCO_3 (200 mL) and water (200 mL), and dried over anhydrous Na_2SO_4 . The solvents were removed under reduced pressure and then poured into hexanes (50 mL). The purple precipitate was collected by centrifugation, yield 60%. ^1H NMR (600 MHz, $\text{DMSO}-d_6$, 298K, δ = ppm, J = Hz): -3.31 (s, 2H, pyrrole-N-H) 8.38-8.43 (dd, J = 12.6, 8H), 9.04 (d, J = 3.88, 4H), 9.67 (d, J = 4.1, 4H), 10.67 (s, 2H), 13.31 (brs, 4H, B-OH). MALDI TOF-MS (THA): calcd. (found) for $[\text{M}+\text{H}]^+$: 550.19 (551.29).



Scheme 4. Synthesis of 5, 15-bis[(dihydroxyboryl)phenyl]-21*H*,23*H*-porphine from 5, 15-bis(4-[1,3,2]-dioxaborinan-2-yl-phenyl)porphyrin.

2.1 *Synthesis and characterization of CoPc-PorDBA COF*

5, 15 porphyrin diboronic acid (**7**, 33mg, 0.06 mmol) and (OH)₈Pc Co (**3**, 21 mg, 0.03 mmol) were sonicated in a mixture of DMAC/*o*-dichlorobenzene (2/1 in vol.; 3 mL) in a glass ampoule and then ampoule was flash frozen in liquid N₂ bath and sealed off at the neck of the ampoule under high vacuum. The ampoule was placed in an oven at 120°C for 74hrs. Then the mixture was filtered off, washed with anhydrous toluene and dried at 100°C under vacuum for 12hrs, to give a dark green powder in 65% isolation yield and was totally insoluble in common organic solvents (such as DCM, THF, DMF, DMSO, etc.). Elemental analysis (%) calcd. for CoPc-PorDBA COF (C₉₆H₄₈B₄N₁₆O₈Co)_n Theory: C (69.64), H (2.92), B (2.61), N (13.54), O (7.73) found C (63.95), H (3.02), N (14.12) respectively. Elemental analysis of boronate COFs generally give lowered carbon values from the formation of non-combustible boron carbide byproducts. The presence of boron was confirmed by a ¹¹B MAS NMR spectroscopy.



Scheme 5. Synthesis of CoPc-PorDBA COF from 5,15 porphyrin diboronic acid and (OH)₈Pc Co(II).

2.1.1 Powder X-ray diffraction and simulation of CoPc- PorDBA COF

Powder X-ray diffraction (Cu K α radiation) was used to determine the crystallinity of the synthesized CoPc- PorDBA COF. The CoPc- PorDBA COF displays an intense diffraction peak at a 2 θ angle (d -spacing) of 2.63° (36.14 Å), less intense peaks at 3.52° (25.55 Å), 5.31 (18.07 Å), 7.74° (7.33

Å), and a broad peak at 25.3° (24.54 Å) (Figure 22). This pattern was manually indexed into a primitive tetragonal unit cell with cell parameters $a = 36.14$ Å and $c = 3.62$ Å similar to other previously reported primitive tetragonal NiPc and ZnPc COFs.¹⁴⁻¹⁶ Crystal models were generated using the Materials Studio modeling suite, using eclipsed sheets of CoPc-PorDBA COF (Figure 22 inset) in a **sql** topology²⁰ using the space group $P4/mmm$, obtaining simulated cell parameters of $a = 36.14$ Å and $c = 3.62$ Å, which match well with the indexed values. Simulated PXRD pattern matched well the experimentally measured one (Figure 22). Pawley refinement was subsequently performed to refine the unit cell parameters and to confirm the assignments of the observed diffraction peaks, obtaining values of $a = 36.54$ Å and $c = 3.67$ Å with good residuals (see below).

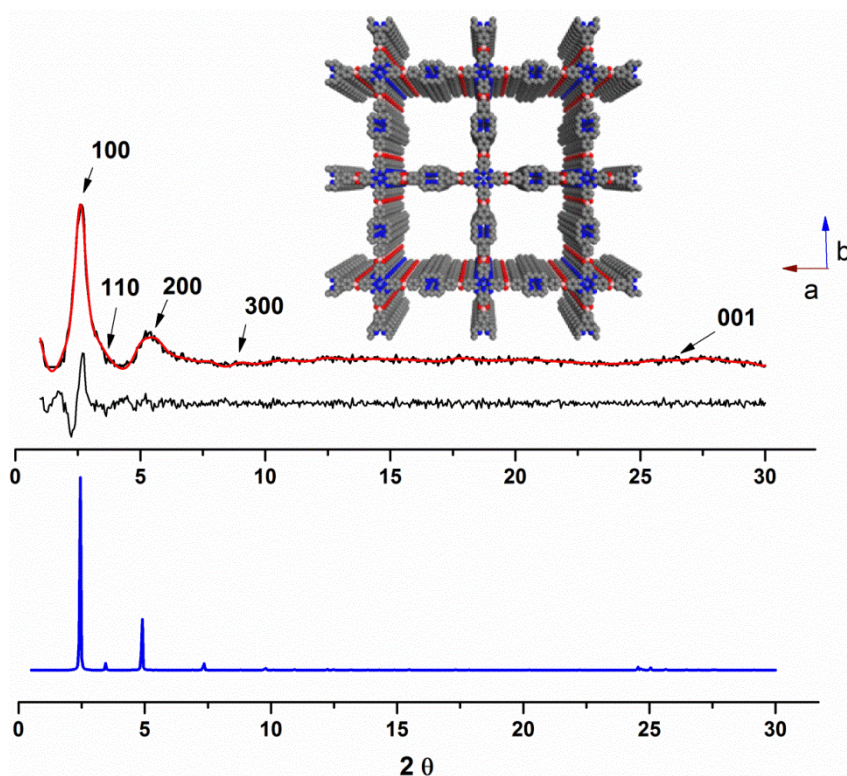
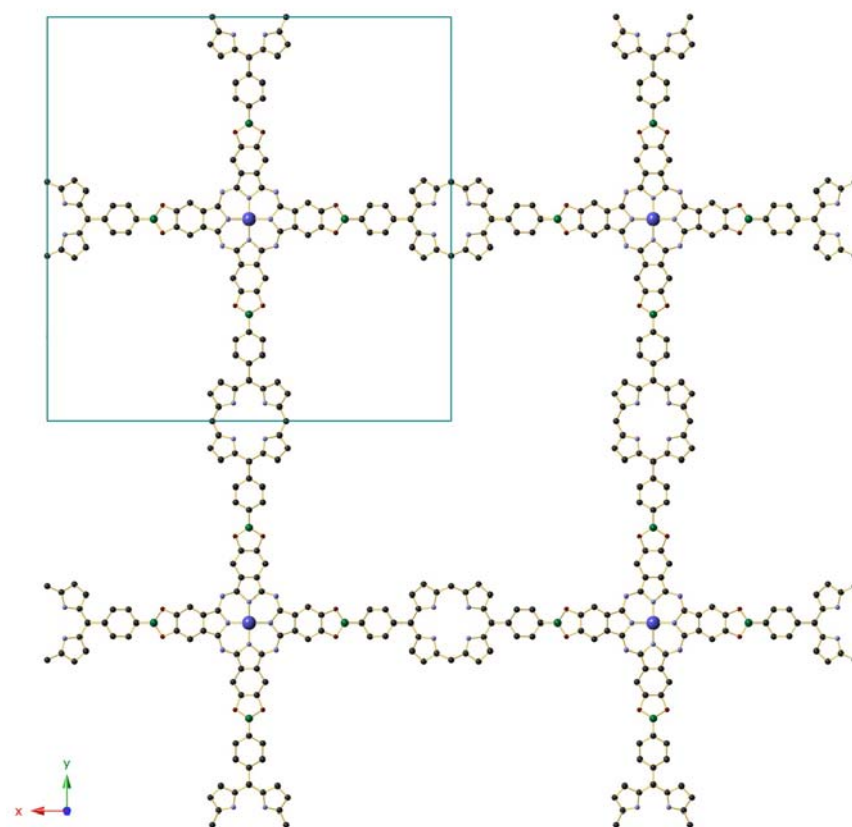


Figure 18. XRD pattern of CoPc-PorDBA COF with the observed pattern in black, Pawley refined profile in red, and the difference plot in black (observed minus refined profiles). The calculated XRD pattern from the proposed models is shown in blue. Inset: Eclipsed stacking representation of CoPc-PorDBA COF based on powder diffraction and modeling projected along the c axis (top) and the b axis (bottom) (H atoms are omitted). C, B, and O are represented in turn as gray, purple, and red spheres.

Modeling of the CoPc-PorDBA COF structure:



Simulation and Refinement of the CoPc-PorDBA COF.

Geometry optimization and Pawley refinement of the CoPc-PorDBA COF was performed with Accelrys MS Modeling 4.3 using Reflex. The final tetragonal unit cell was calculated with the geometrical parameters from the optimized structure. Pawley refinement was performed to optimize the lattice parameters iteratively until the R_{WP} value converges. After Pawley refinement the peak profile was refined using the Pseudo-Voigt peak shape function and whole profile fitting was done using Berrar - Baldinozzi function for asymmetry correction during the refinement processes. The final R_{WP} and R_p values were 10.26% and 15.68%, respectively. The unit cell parameters were first calculated and then refined from the experimentally observed peak positions, as a result we obtained cell parameters of $a = b$

= 36.54 Å and $c = 3.67$ Å. Simulated PXRD patterns were calculated for an eclipsed arrangement of $P4/mmm$ space group, where all atoms in an each layer of the framework lay over one another.

Refined unit cell parameters and fractional atomic coordinates for CoPc-PorDBA COF.

CoPc-PorDBA COF	a (Å)	c (Å)
MS modeling	36.5427	3.6735
Pawley refinement	36.1499	3.6246

Atom name	x	y	z
C1	0.5	0.5	0.25
B2	0.5	0.5	0.25
N3	0.5	0.5	0.25
C4	0.5	0.5	0.25
C5	0.5	0.5	0.25
C6	0.46689	0.5	0.5
C7	0.46669	0.5	0.5
C8	0.48075	0.5	0.5
C9	0.46026	0.5	0.5
C10	0.48086	0.5	0.5
C11	0.46913	0.5	0.5
O12	0.46596	0.5	0.5
C13	0.53479	0.5	0.5
C14	0.56997	0.5	0.5
C15	0.59558	0.5	0.5
C16	0.57509	0.5	0.5
N17	0.53879	0.5	0.5
N18	0.43351	0.5	0.25
C19	0.5	0.5	0.0625
C20	0.59115	0.5	0.25

2.1.2 FT-IR measurements of CoPc-PorDBA COF

The Fourier-Transformed Infrared spectrum showed a stretching frequency at 1344 cm^{-1} which corresponds to the newly formed boronate ester linkage between **3** and **7** (Figures 23 and 24) including attenuation of peaks at 3400 cm^{-1} and 3140 cm^{-1} , which correspond to hydroxyl groups of the phthalocyanine and porphyrin diboronic acid, respectively.

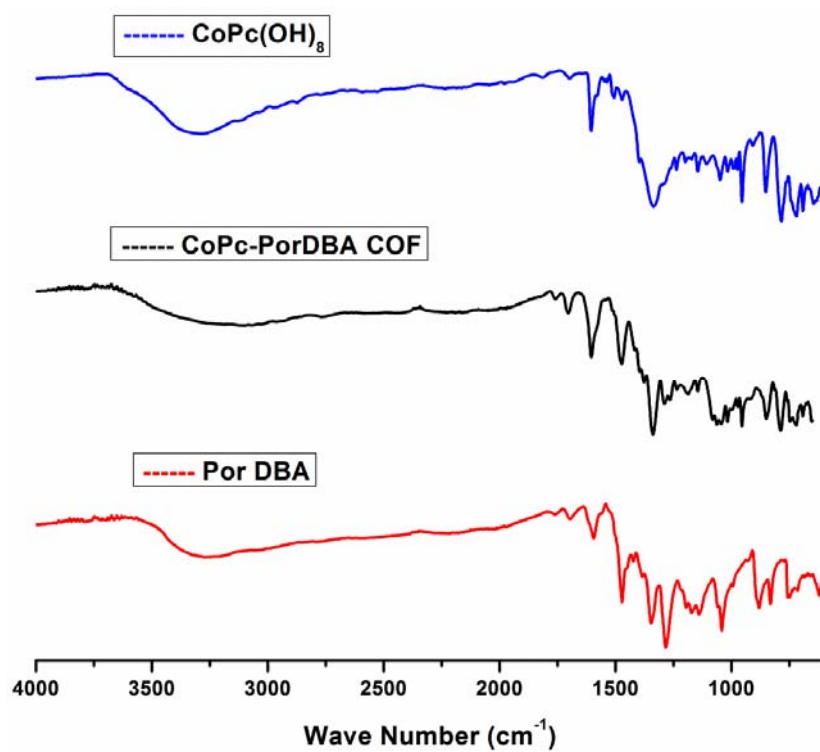


Figure 19. IR spectra of $(\text{OH})_8\text{Pc Co(II)}$ (blue), CoPc-PorDBA COF (black) and 5, 15 porphyrin diboronic acid (red).

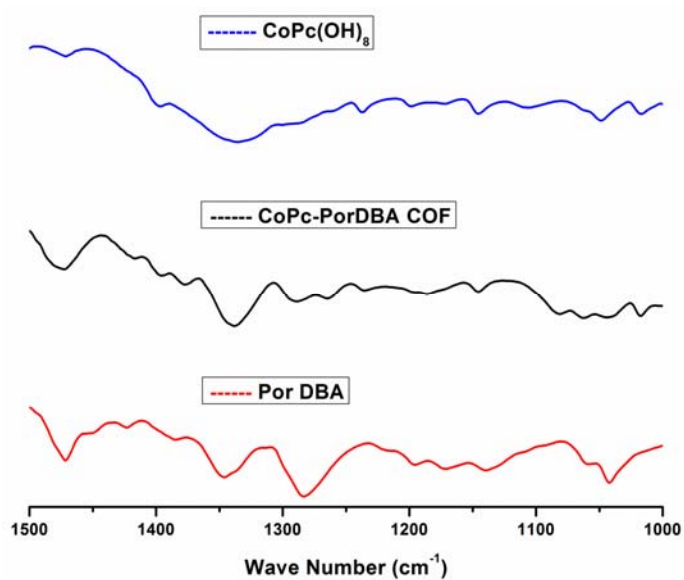


Figure 20. Expanded IR spectra of $(\text{OH})_8\text{Pc Co(II)}$ (blue), CoPc-PorDBA COF (black) and 5, 15 porphyrin diboronic acid (red).

Peak (cm ⁻¹)	Assignments
3400-3350 (w)	O–H stretch of the end-groups B(OH) ₂ or OH
1604 (s)	C=C stretch for phenyl ring
1540 (w) 1510 (w) 1488 (w) 1465 (w)	Skeletal vibration of porphyrin ring
1390 (m)	C=C vibration of phenyl ring
1344 (s)	B–O stretch (boronic ester)
1250 (w)	C–B stretch
1207 (w)	C–H in plane deformation
1132 (s)	C–O stretch (characteristic band for boronic ester)
856 (w)	C–H out of plane deformation of <i>p</i> -substituted benzene
798 (m) 745 (w) 736 (w) 700 (w)	C–H out of plane deformation

2.1.3 Gas adsorption measurements of CoPc-PorDBA COF

To evaluate the porosity of the CoPc-PorDBA COF, N₂ adsorption-desorption isotherms were measured at 77K. A Brunauer-Emmet-Teller (BET) surface area of 1315m²/g was obtained with a type IV shaped isotherm typical of mesoporous materials and with reversible sorption profiles (Figure 25). The total pore volume was calculated to be 0.88cm³/g and the average pore size was calculated using nonlocal density functional theory (NLDFT), and found to be approximately 3.5 nm (Figure 26). Once the permanent porosity of CoPc-PorDBA COF was established, we evaluated the potential of CoPc-PorDBA COF for H₂ and CH₄ storage. The H₂ storage capacity of CoPc-PorDBA COF is 0.8 wt% at 77K, 1bar (Figure 29) which is comparable to other crystalline 2D COFs such as COF-10¹² (0.8 wt% at 1bar). In direct contrast to the H₂ uptake, the CH₄ isotherm for CoPc-PorDBA revealed an uptake of

only 0.6 wt% at 298K, 1bar (Figure 30). We believe that the lower uptake of CH₄ compared to H₂ may be due to the size difference.

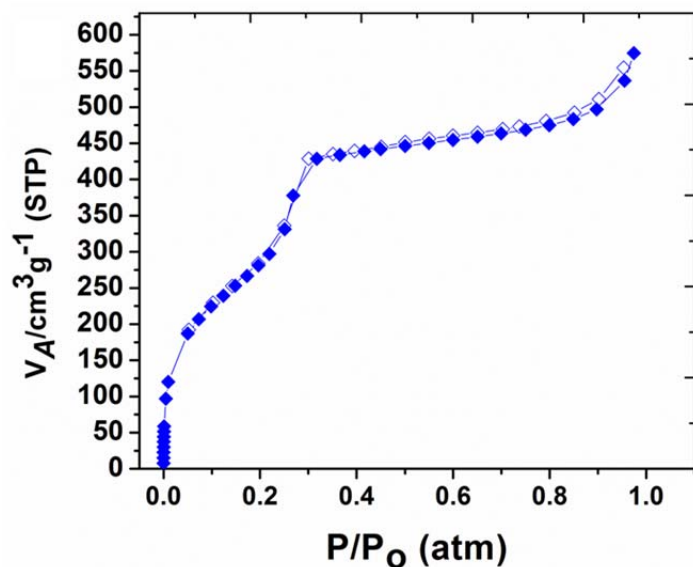


Figure 21. N₂ adsorption (filled symbols) and desorption (empty symbols) isotherm curve and surface area.

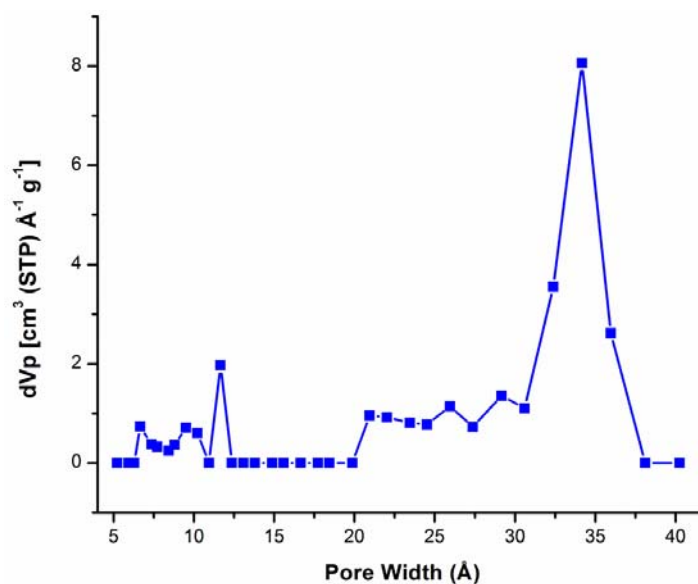


Figure 22. Differential (top) pore size distribution plot of CoPc-PorDBA COF from the application of the NLDFIT model to the N₂ isotherm.

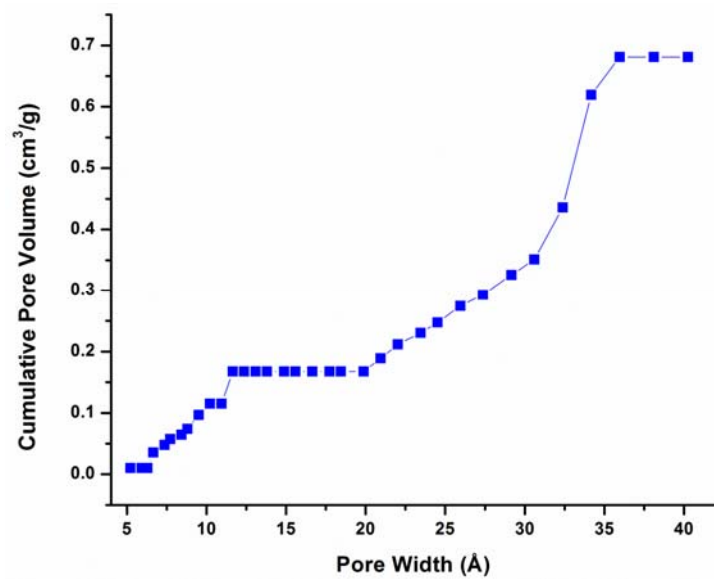


Figure 23. Cumulative (bottom) pore size distribution plot of CoPc-PorDBA COF from the application of the NLDFIT model to the N₂ isotherm.

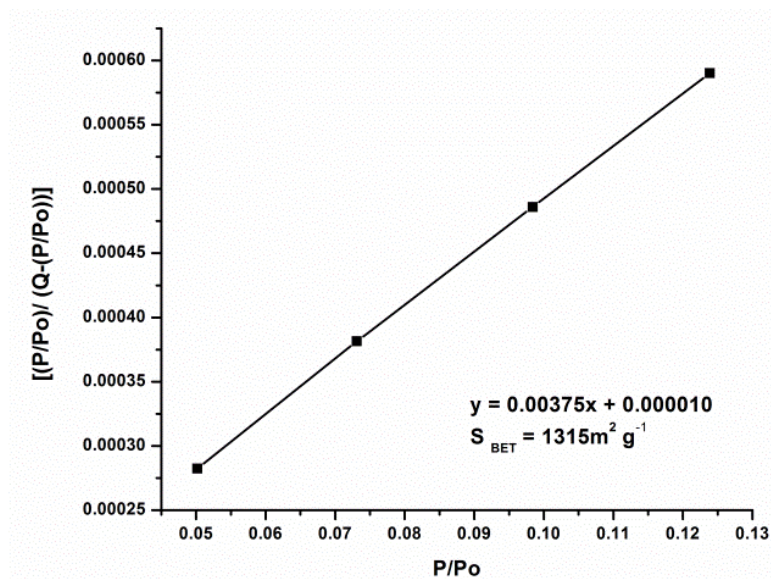


Figure 24. BET plot for CoPc-PorDBA COF calculated from isotherm data.

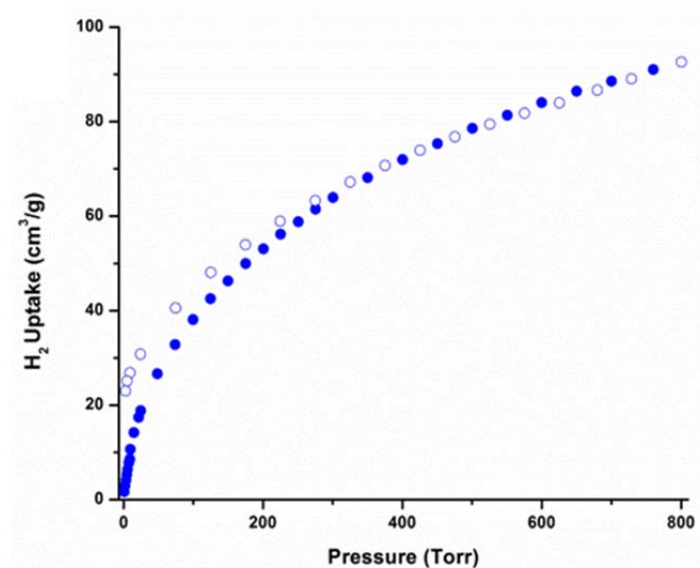


Figure 25. H₂ adsorption (filled symbols) and desorption (empty symbols) isotherm curve and surface area.

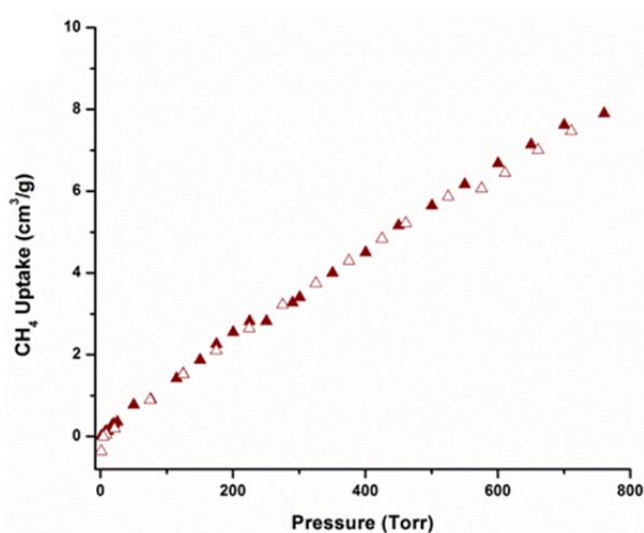


Figure 26. CH₄ adsorption (filled symbols) and desorption (empty symbols) isotherm curve and surface area.

2.1.4 Diffuse reflectance UV-Vis measurements of CoPc-PorDBA COF

The UV-Vis diffuse reflectance powder spectra of CoPc-PorDBA COF (Figure 32) showed strong absorption bands at 220 nm, 252nm, 282nm, 453nm, 590nm, 625nm, 730nm and CoPc showed absorption peaks at 280nm, 595nm, 650nm and 735nm. The CoPc electronic absorption spectrum (Figure 31) in dilute dichloromethane solution showed strong absorption bands at 295nm, 342nm,

443nm, 615nm and 740nm are typical of metallophthalocyanines. As explained in other reports¹⁴ the blue shift of solid state CoPc-PorDBA (35nm) of the B band when compared to that for CoPc(OMe)₈ in dichloromethane solution is due to the difference in aggregated phthalocyanines in the solution and in the solid state (liquid crystalline) while the red shift of the Q band is due to the differences in aggregation geometry as well as the electron-withdrawing nature of the boronate esters. The PorDBA solid-state diffuse reflectance spectra (Figure 32) show a low intense band at about 415 nm, typical of the Soret band of the UV–Vis absorption spectra of porphyrin in homogeneous solutions (Figure 31). The low intensity Soret band may possibly due to the stacking instead of aggregation of porphyrins in the COF. The CoPc-PorDBA COF showed some similarities when compared to individual electronic absorption spectra of CoPc(OMe)₈ and PorDBA.

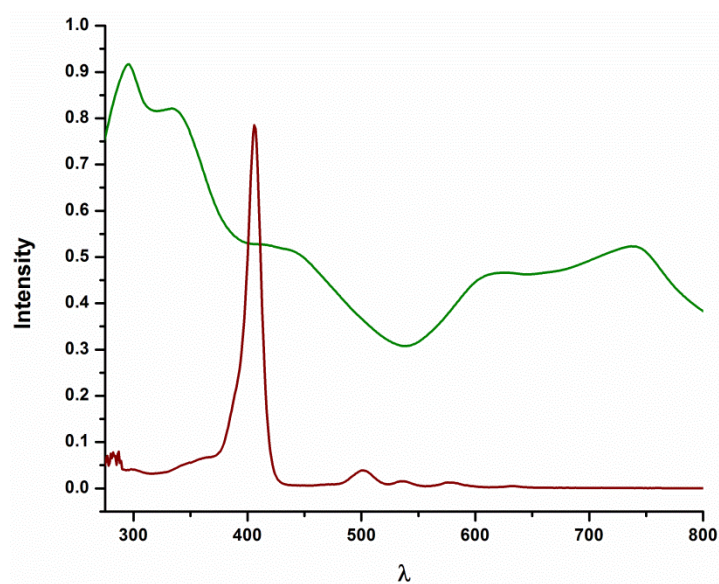


Figure 27. UV-Vis absorption spectra of CoPc (green curve) in dichloromethane and PorDBA (purple curve) in THF.

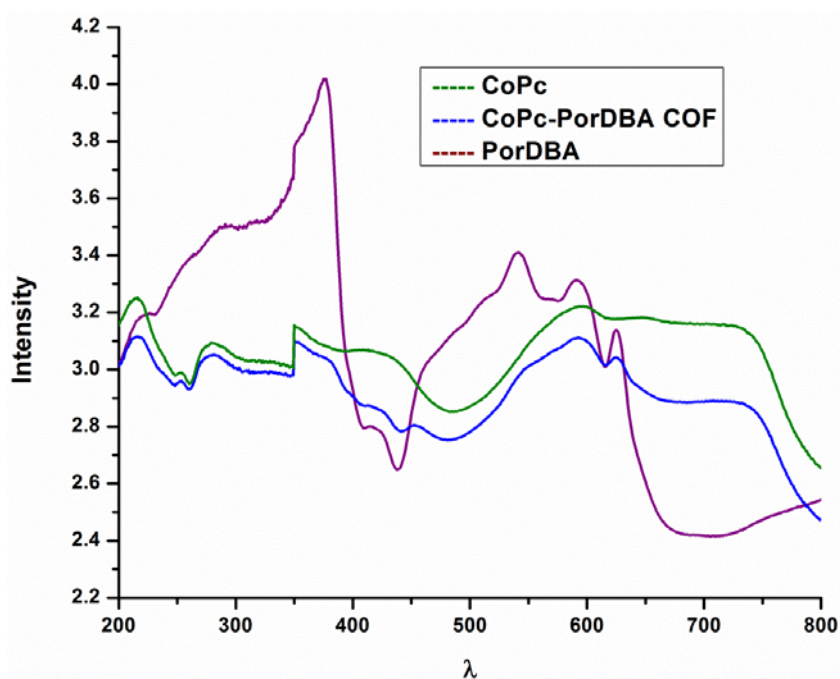


Figure 28: Solid-state absorption spectra CoPc-PorDBA COF (blue), CoPc (green) and PorDBA (purple) as powders using a praying mantis diffuse reflectance accessory. Small, jagged peaks around 340nm are due to instrument lamp shift.

2.1.5 Solid state NMR measurements of CoPc-PorDBA COF

The solid state ^{13}C with (CP/MAS) NMR spectrum (Figure 33) of the CoPc-PorDBA COF shows nine signals at $\delta = 173.44, 157.86, 143.95, 134.64, 127.72, 115.23, 106.06, 100.94$ and 97.11 ppm, which were assigned to the carbon atoms of the phthalocyanine and phenyl groups by comparison to the spectrum of octahydroxy phthalocyanine Co(II) (Figure 34). The ^{11}B magic angle spinning (MAS) NMR spectrum of the CoPc-PorDBA COF displays similar features to those of other reported COFs and to those of the starting materials.

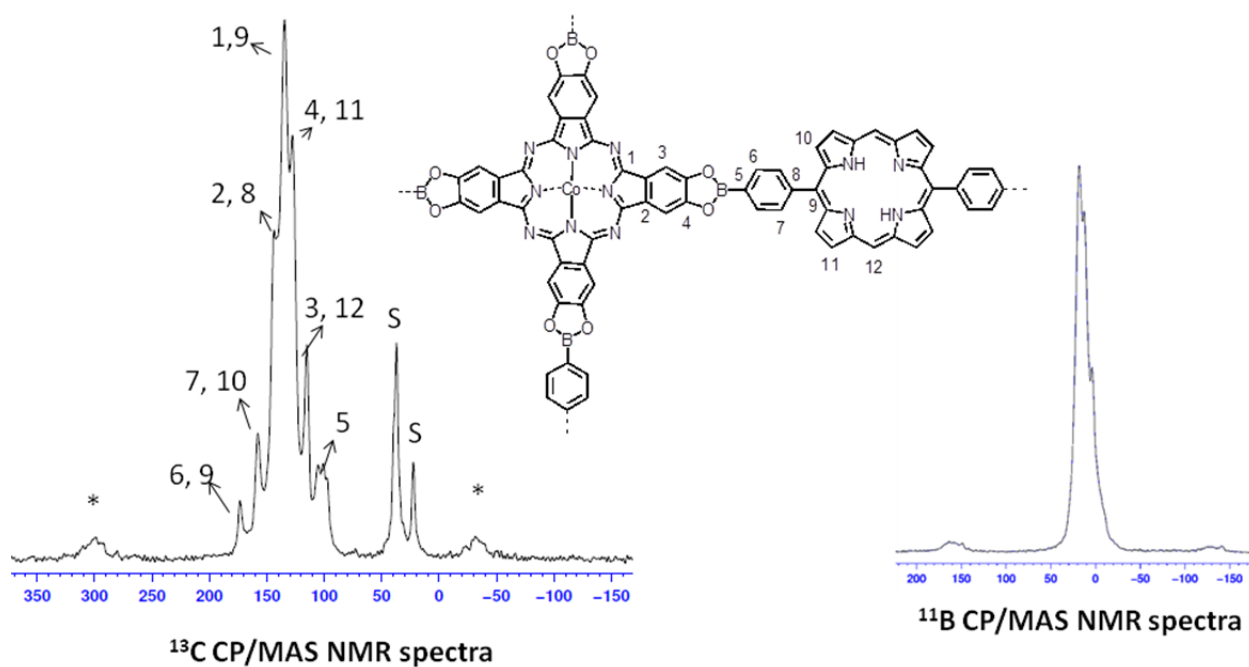


Figure 29. Solid state ^{13}C CP/MAS NMR and ^{11}B CP/MAS spectra of CoPc-PorDBA COF recorded at a MAS rate of 12.5 kHz. Signals with S and * are residual solvent and side bands.

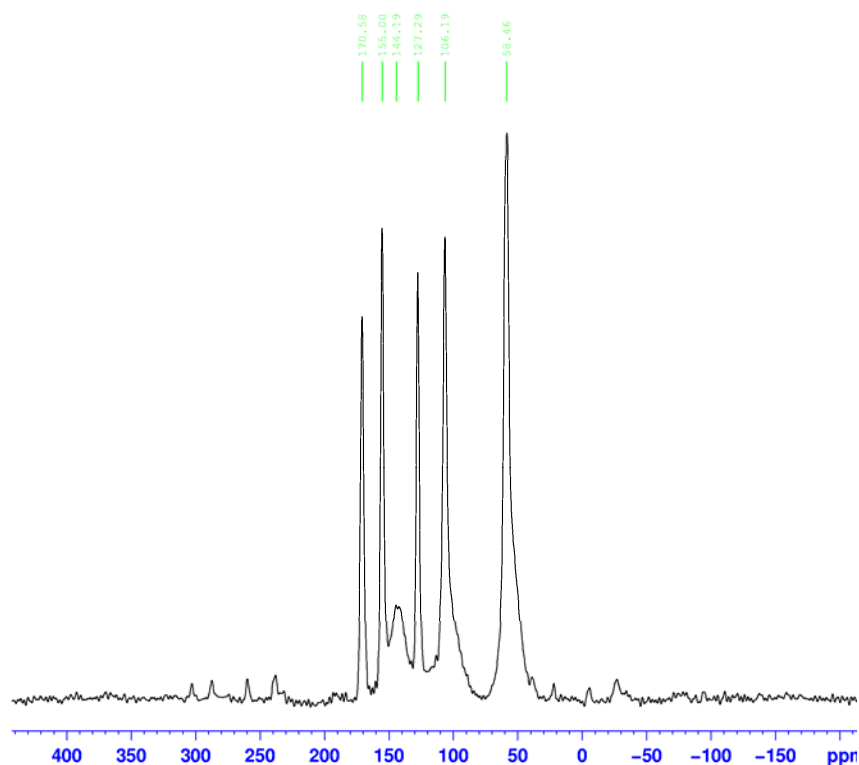


Figure 30. Solid state ^{13}C CP/MAS NMR spectra of CoPc (OMe)₈ recorded at a MAS rate of 12.5 kHz. Signals with * are side bands.

2.1.6 Scanning electron microscopy images of CoPc-PorDBA COF

The SEM image brought out its layered sheet structure (Figure 35) and flake like morphology.

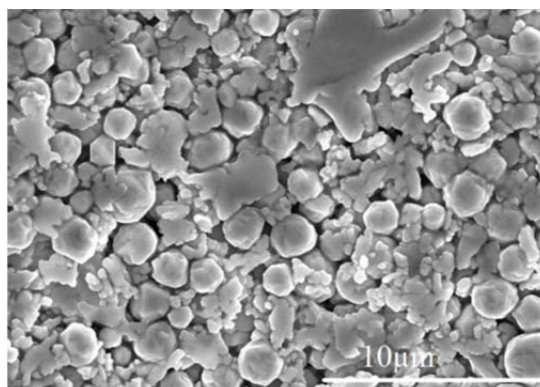


Figure 31. Scanning electron microscope (SEM) image of the CoPc-PorDBA COF grown under solvothermal conditions.

2.1.7 Thermogravimetric analysis of CoPc-BPDA COF

Thermogravimetric analysis (TGA) of the CoPc-PorDBA COF showed high thermal stability (Figure 36), retaining 90% of its mass at 300°C.

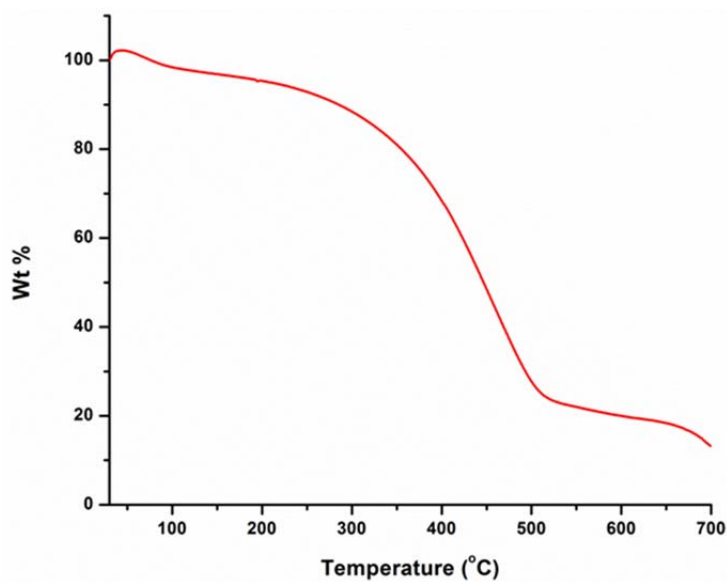
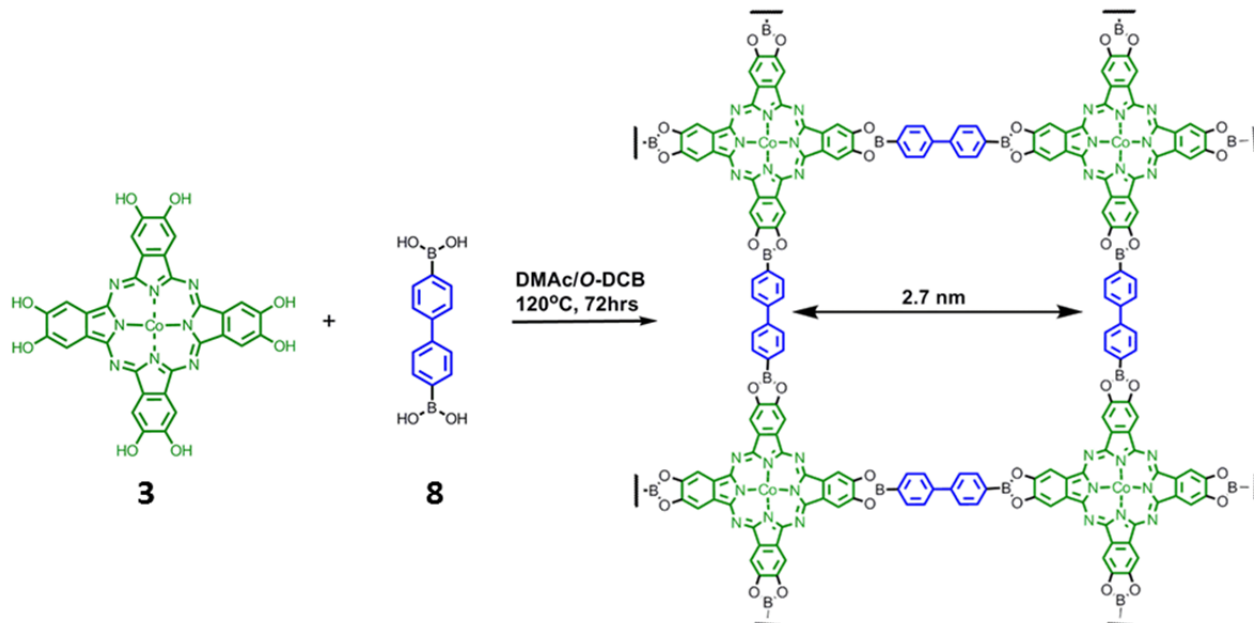


Figure 32. TGA of CoPc-PorDBA COF obtained up to 700°C using a linear 3 °C/min ramp method.

2.2 Synthesis and characterization of CoPc-BPDA COF

4, 4'-biphenyldiboronic acid (**8**, 14.51mg, 0.06 mmol) and $(\text{OH})_8\text{PcCo}$ (**3**, 21 mg, 0.03 mmol) were sonicated in a mixture of DMAc/*o*-dichlorobenzene (2/1 in vol.; 2 mL) in a glass vial, then the mixture was transferred into a glass ampoule. The ampoule was flash frozen in liquid N_2 bath and sealed off at the neck of the ampoule under vacuum (Scheme 6). The ampoule was placed in an oven at 120°C for 72hrs. Then the mixture was filtered off, washed with anhydrous toluene and dried at 150°C under vacuum for 12 h, to give a dark green powder in 80% isolation yield. Elemental analysis (%) calcd. for CoPc-BPDA COF $(\text{C}_{56}\text{H}_{24}\text{B}_4\text{N}_8\text{O}_8\text{Co})_n$ Theory: C (64.74), H (2.33), N (10.78), found C (57.05), H (3.26), N (9.76) respectively. Elemental analysis of boronate ester COFs generally give lowered carbon values from the formation of non-combustible boron carbide byproducts. The presence of boron was confirmed by ^{11}B MAS NMR spectroscopy.



Scheme 6. Synthesis of CoPc-BPDA COF from 4,4'-biphenylboronic acid and $(\text{OH})_8\text{Pc Co(II)}$.

2.2.1 Powder X-ray diffraction and simulation of CoPc-BPDA COF

Powder X-ray diffraction (Cu K α radiation) was employed to find out the crystalline nature of the as-synthesized CoPc-BPDA COF. The experimental diffraction pattern (Figure 37) displays an intense diffraction peak at a 2θ angle (d -spacing) of 3.23° (27.3 Å), and less intense peaks at 4.56° (19.3 Å), 6.46° (13.66 Å), 9.7° (9.10 Å), 12.95° (6.83 Å) and a broad peak at 24.4° (3.55 Å). With cell parameters of $a = 27.322$ Å and $c = 3.55$ Å, this pattern was manually indexed into a primitive tetragonal unit cell similar to other primitive tetragonal reported NiPc and ZnPc COFs. Using the Materials Studio modeling suite of programs, crystal models were generated, from eclipsed stacking sheets of CoPc-BPDA COF (Figure 37 inset) in a **sql** topology²⁰ using the space group $P4/mmm$, resulting in simulated cell parameters of $a = 27.30$ Å and $c = 3.652$ Å, which match the indexed values. The simulated powder X-ray diffraction pattern also matched well with the measured pattern (Figure 37). The powder XRD pattern of CoPc-BPDA COF was subjected to Pawley refinement which produced refined PXRD curves with lattice parameters of $a = 26.65$ Å and $c = 3.55$ Å with good residuals (see below).

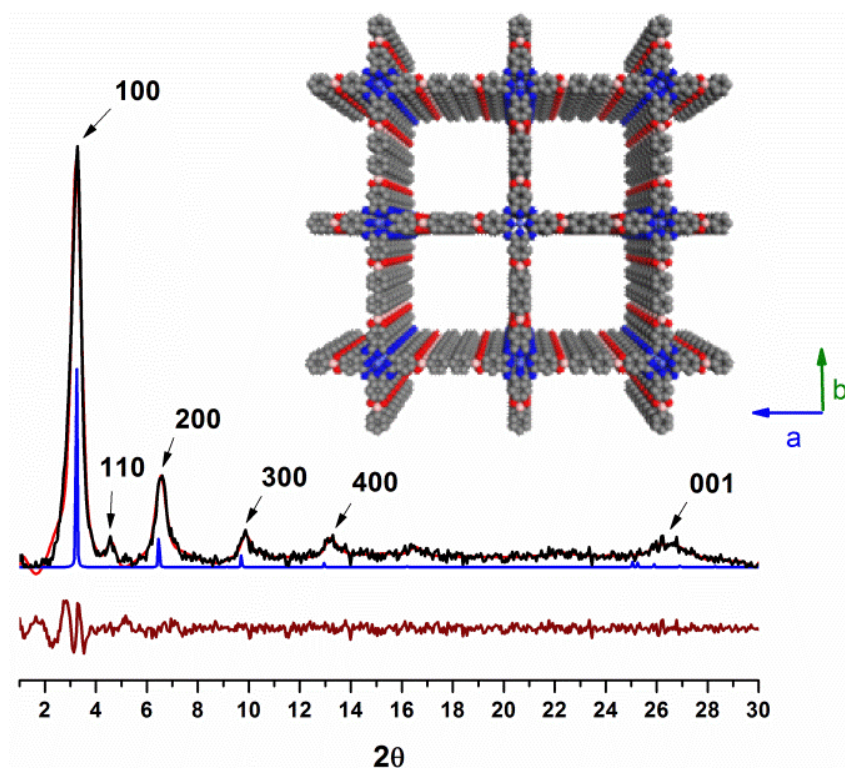
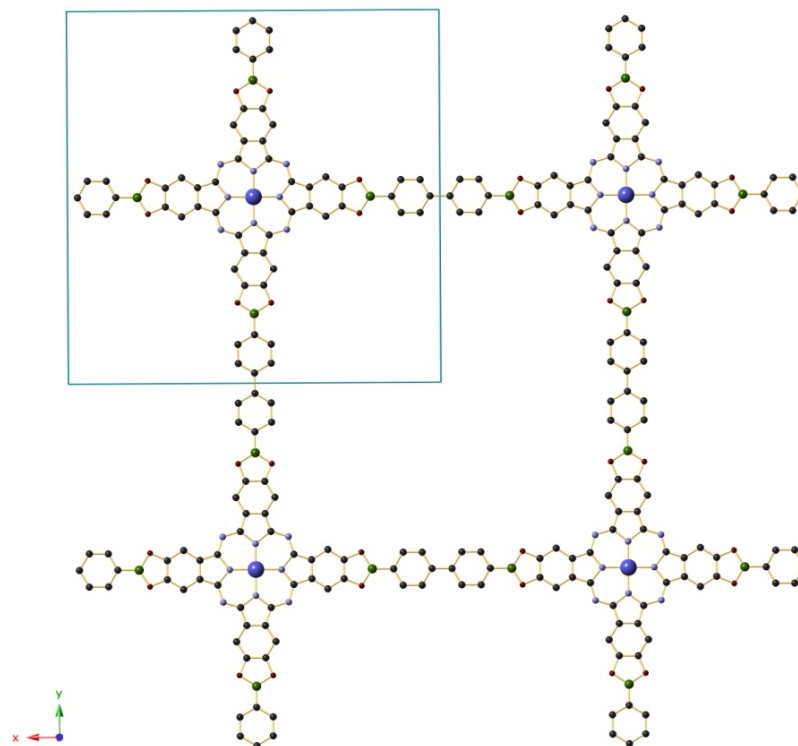


Figure 33. XRD pattern of CoPc-BPDA COF in black, Pawley refined profile in red, and the difference plot in purple (observed minus refined profiles). The calculated XRD pattern from the proposed models is shown in blue. Inset: Eclipsed stacking representation of CoPc-BPDA COF based on powder diffraction and modeling projected along the c-axis view (H atoms are omitted).

Simulation & Refinement of the CoPc-BPDA COF

Geometry optimization and Pawley refinement of the CoPc-BPDA COF was carried out with Accelrys MS Modeling 4.3 using Reflex module. The unit cell dimensions were calculated from the geometrical parameters from the optimized structure. Pawley refinement was performed to optimize the lattice parameters iteratively until the R_{WP} value converges. After Pawley refinement the peak profile was refined using the Pseudo-Voigt peak shape function and whole profile fitting was done using Berrar - Baldinozzi function for asymmetry correction during the refinement processes. The final R_{WP} and R_p values were 10.69% and 16.39%, respectively. The unit cell parameters were first calculated and then refined from the experimentally observed peak positions, as a result we obtained cell parameters of $a = b$

= 26.65 Å and $c = 3.55$ Å. Simulated PXRD patterns were calculated for an eclipsed arrangement of $P4/mmm$ space group, where all atoms in an each layer of the framework lay over one another.



Refined unit cell parameters and fractional atomic coordinates for CoPc-BPDA COF.

CoPc-BPDA COF	a (Å)	c (Å)
MS modeling	27.30	3.6235
Pawley refinement	26.65	3.55

	B	C	Co	N	O
C1	2	0.02713	0.5	0.5	0.25
B2	1	0.18692	0.5	0.5	0.25
N3	4	0.43026	0.5	0.5	0.25
C4	2	0.13009	0.5	0.5	0.25
C5	2	0.0533	0.45571	0.5	0.5
C6	2	0.10447	0.45571	0.5	0.5
C7	2	0.26281	0.47453	0.5	0.5
C8	2	0.30645	0.44741	0.5	0.5
C9	2	0.34987	0.47465	0.5	0.5

C10	2	0.39788	0.45912	0.5	0.5
O11	5	0.21603	0.45501	0.5	0.5
N12	4	0.41198	0.41198	0.5	0.25
Co13	3	0.5	0.5	0.5	0.0625

2.2.2 FT-IR measurements of CoPC- BPDA COF

The formation of boronate ester bonds between **3** and **8** (Figures 38 and 39) was first established by FT-IR which exhibited a new stretching frequency at 1330 cm^{-1} including attenuation of peaks at 3400cm^{-1} and 3350cm^{-1} , which correspond to hydroxyl groups of the phthalocyanine and boronic acids, respectively.

Peak (cm^{-1})	Assignments
1618	C=C vibration of phenyl ring
1483	C=N stretch of Pc macrocycles
1410	C=C vibration of phenyl ring
1344	B-O stretch, characteristic band of boroxoine compounds
1292	C-O stretch
1090	B-C stretch, characteristic band of boroxoine compounds
1055	Vibration and characteristic band of Pc macrocycles
747	Vibration and characteristic band of Pc macrocycles
662	Out-of-plane bending of the C-H bonds of phenyl rings

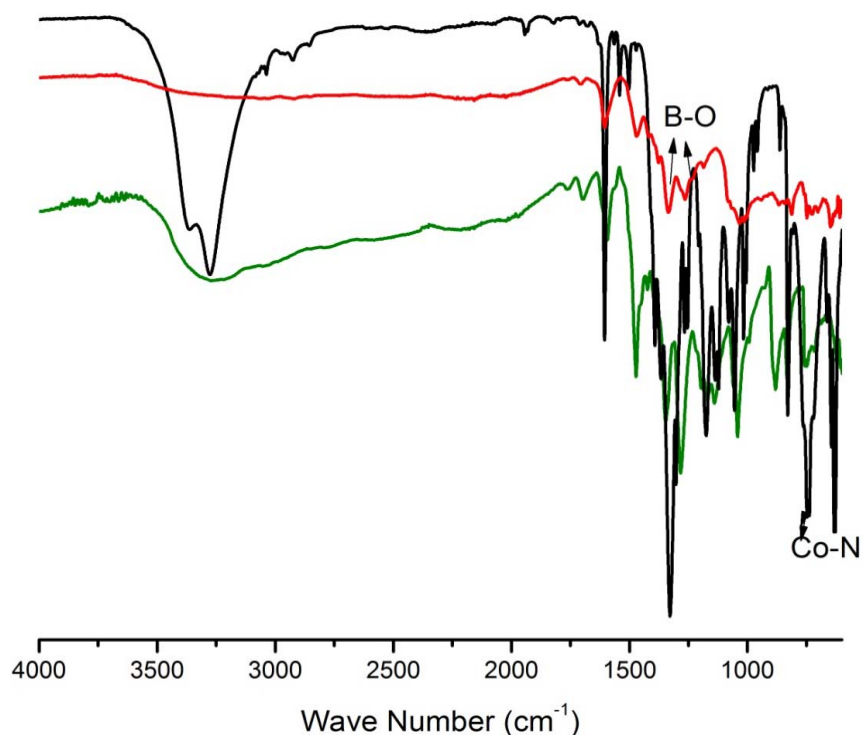


Figure 34. IR spectra of 4, 4'-Biphenyldiboronic acid (black curve), (OH)₈PcCo (green curve) and CoPc-BPDA COF (red curve).

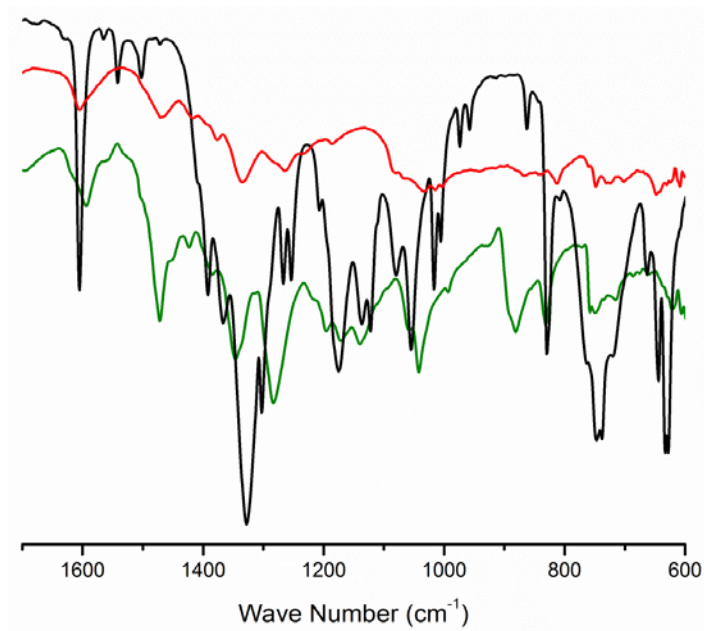


Figure 35. Expansion of 600-1700 cm^{-1} region of the above spectrum.

2.2.3 Gas adsorption measurements of CoPc- BPDA COF

To examine the permanent porosity of the CoPc-BPDA COF we measured the BET surface area using N₂ adsorption isotherms at 77K. The N₂ uptake displays a type IV isotherm (Fig. 40a), typical of mesoporous materials and with reversible sorption profiles with a Brunauer-Emmet-Teller (BET) surface area of 1087m²/g. The total pore volume was calculated to be 0.573cm³/g and the average pore size was calculated using nonlocal density functional theory (NLDFT), and found to be approximately 2.26 nm (Figure 41). As we have stated earlier, metallated or metal-doped COFs are among the most promising materials for gas storage, H₂ in particular. We evaluated the physisorption of H₂ and CH₄ on CoPc-BPDA COF at low pressures and different temperatures. The H₂ uptake of CoPc-BPDA COF at 77 K, 1bar is 1.2 wt% (Figure 40b) which is more than other crystalline 2D COFs such as COF-10¹² (0.8 wt% at 77K and 1bar). The H₂ isotherms are fully reversible with uptake ranges between 0.15–1.20 wt% at 77 K. We also measured CH₄ storage properties with CoPc-BPDA COF at 273K and 298K, which revealed an uptake of only 0.59 wt% at 273K and 0.45 wt% at 298 K and 1bar (Figure 40c).

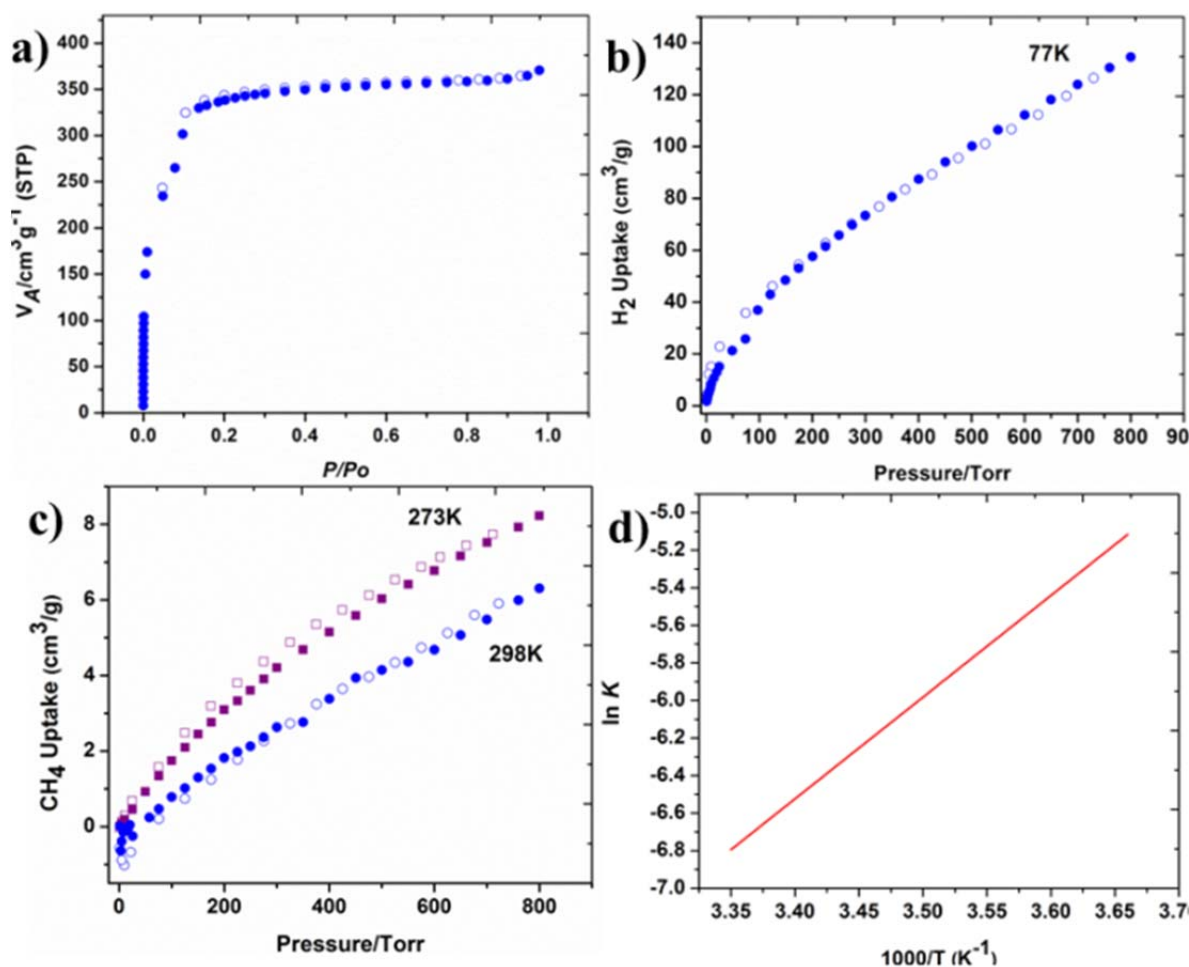


Figure 36. (a) Nitrogen at 77K (b) Hydrogen at 77K (c) Methane at 273K and 298K. Adsorption (filled symbols) and desorption (empty symbols) isotherm curves (d) Van't Hoff plot for CH₄ isotherms.

Calculation of isosteric heat of adsorption

The adsorption enthalpy at zero coverage was calculated from Henry constant using the Van't Hoff equation as

$$\ln K = -\frac{\Delta H}{RT} + \frac{\Delta S}{R}$$

K is Henry constant, T is temperature, plotting $\ln K$ vs $1000/T$

The isosteric heat of adsorption (Q_{st}) value was calculated (Figure 40d) at zero coverage by calculating Henry's constants and using the Van't Hoff equation from the CH₄ isotherms at 273K and 298K. The calculated Isosteric heat of adsorption (Q_{st}) value is 44.9 kJ mol⁻¹. The Q_{st} value is higher than those reported for 2D and 3D non-phthalocyanine based COFs.¹² The reversible

adsorption/desorption behavior and moderate Q_{st} values of CoPc-BPDA COF, indicate that CH_4 interactions with pore walls are sufficiently high to allow for material regeneration without applying heat. The relatively lower adsorption of CH_4 relative to the value obtained for H_2 may be due to size related effect.

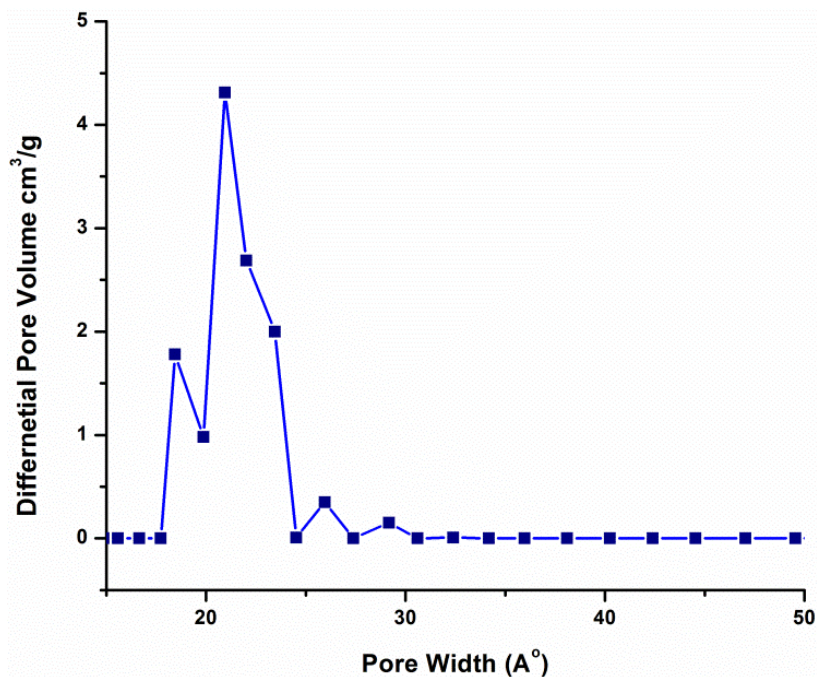


Figure 37. Differential pore size distribution plot of CoPc-BPDA COF from the application of the NLDFT model to the N_2 isotherm.

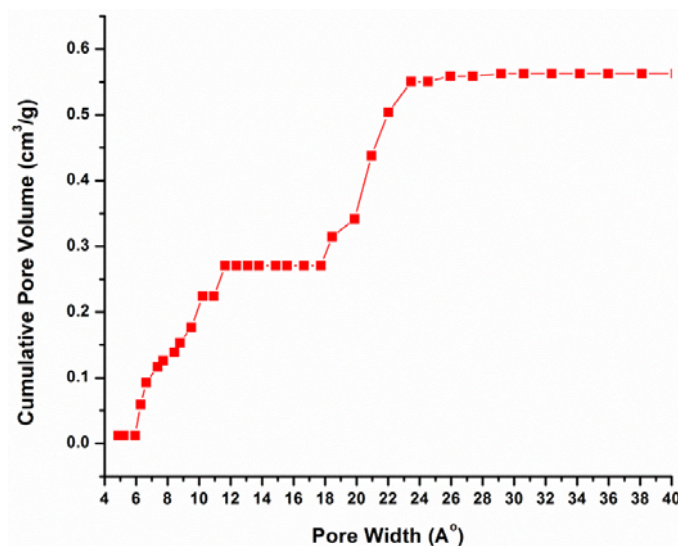


Figure 38. Cumulative pore size distribution plot of CoPc-BPDA COF from the application of the NLDFT model to the N_2 isotherm.

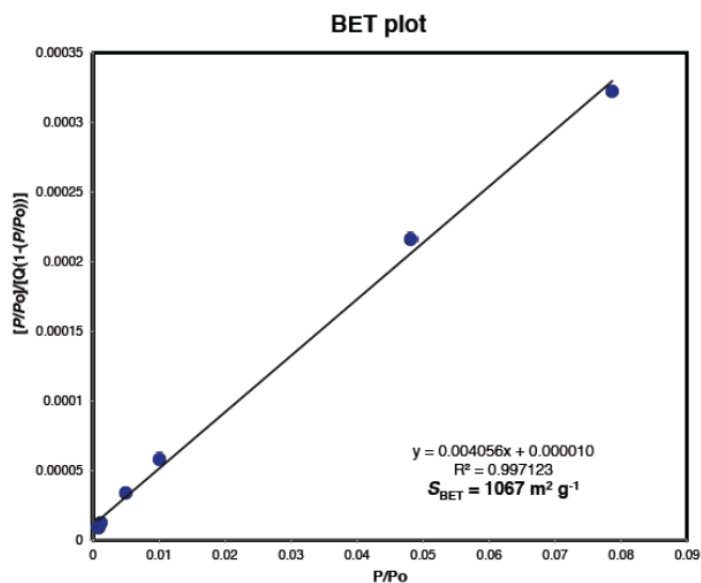


Figure 39. BET plot for CoPc-BPDA COF calculated from isotherm data.

2.2.4 Solid state NMR measurements of CoPc- BPDA COF

The solid-state ^{11}B and ^{13}C cross polarization with magic angle spinning (CP/MAS) NMR spectra (Figures 44 and 45) further support the formation of the boronate ester bond between **3** and **8** and the incorporation of phthalocyanine monomers into the CoPc-BPDA COF framework. Solid-state ^{13}C CP-MAS NMR spectra of the CoPc-BPDA COF show five signals at $\delta = 172.34$, 155.94 , 144.34 , 127.94 , and 105.28 ppm, which were assigned to the carbon atoms of the phthalocyanine and phenyl groups by comparing to the spectrum of octahydroxy phthalocyanine Co(II) (Figure 45).

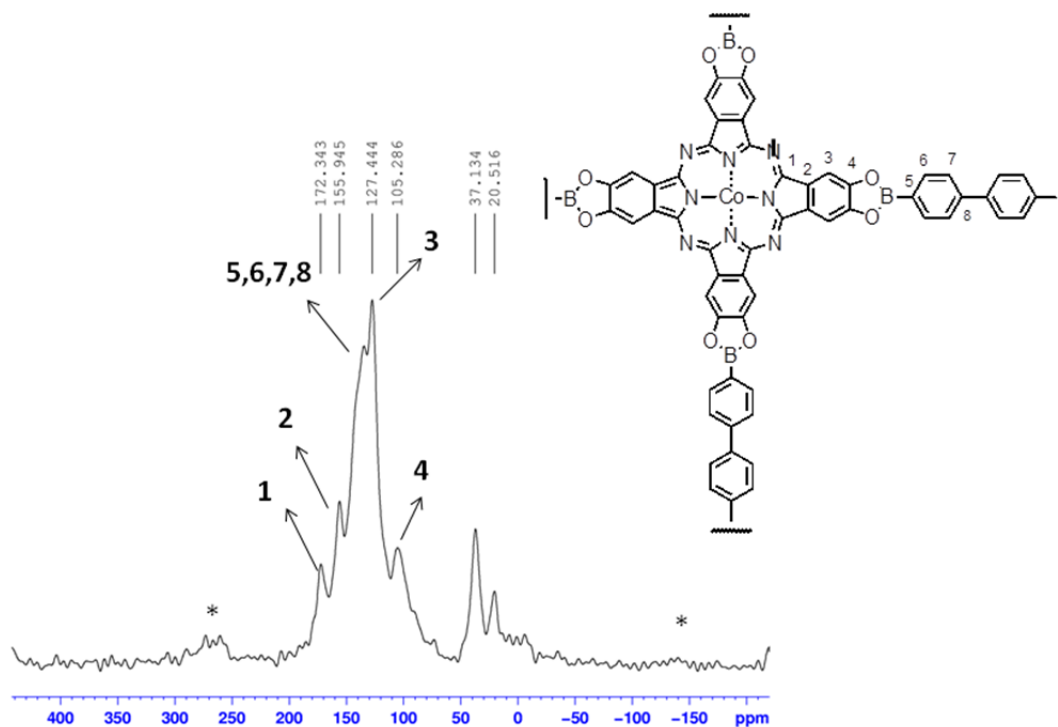


Figure 40. Solid state ^{13}C CP/MAS NMR spectra of CoPc-BPDA COF recorded at a MAS rate of 12.5 kHz. Signals with * are side bands.

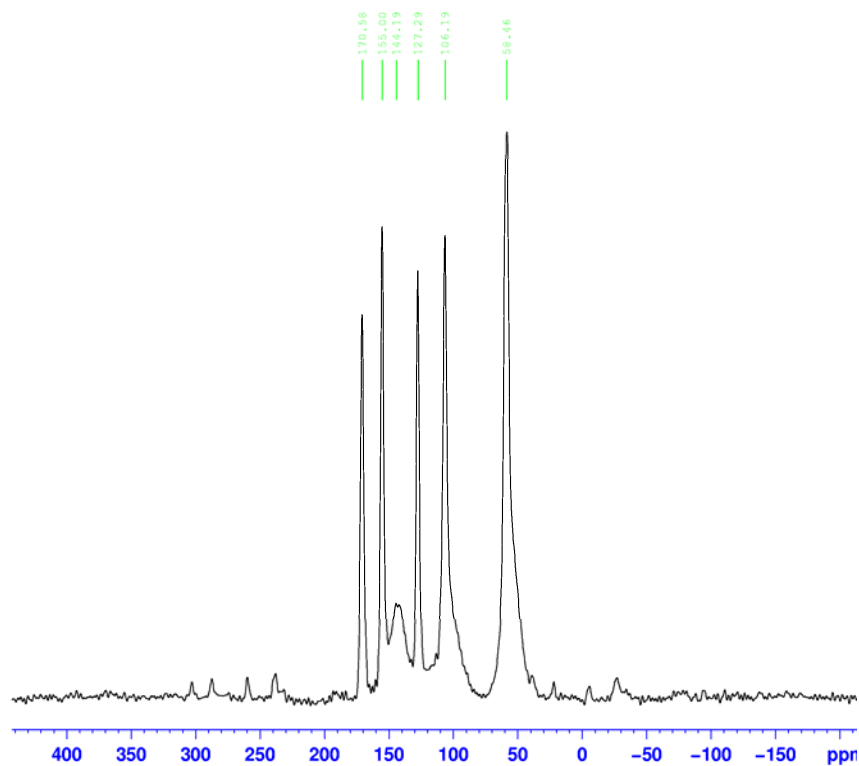


Figure 41. Solid state ^{13}C CP/MAS NMR spectra of CoPc (OMe)₈ recorded at a MAS rate of 12.5 kHz. Signals with * are side bands.

2.2.5 Scanning and Cryo electron microscopy images of CoPc- BPDA COF

The layered structure of the COF was also observed by scanning electron microscopy (SEM) and Cryo electron microscope (Cryo-EM). The SEM image revealed the superimposed sheet structure (Figure 46) and the Cryo-EM measurements showed the porous nature of the CoPc-BPDA COF (Figure 47).

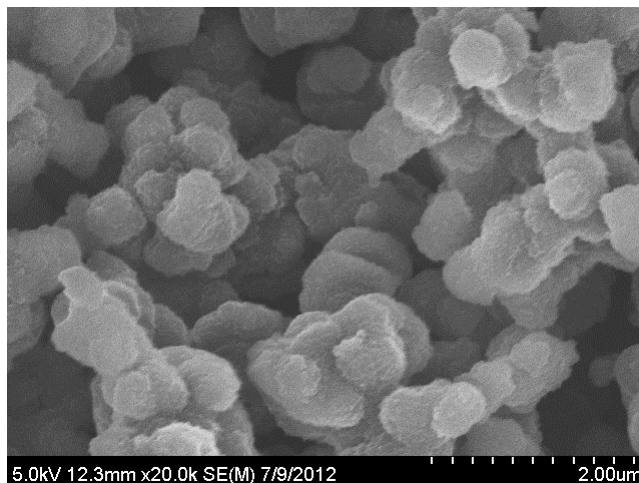


Figure 42. Scanning electron microscope (SEM) image CoPc- BPDA COF powder.

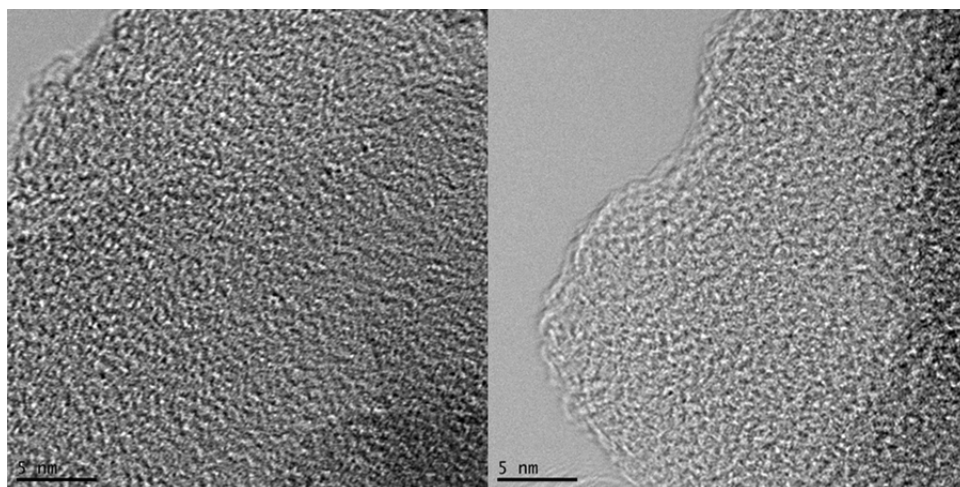


Figure 43. Cryo Electron Microscope Images of CoPc-BPDA COF.

2.2.7 Thermogravimetric analysis of CoPc- BPDA COF

To measure the thermal stability CoPc-BPDA COF, the as-synthesized sample was subjected to thermogravimetric analysis under a flow of N₂ (Figure 48). The TGA trace is typical of other reported boronate ester based COFs, retaining 80% of the mass at 300 °C.

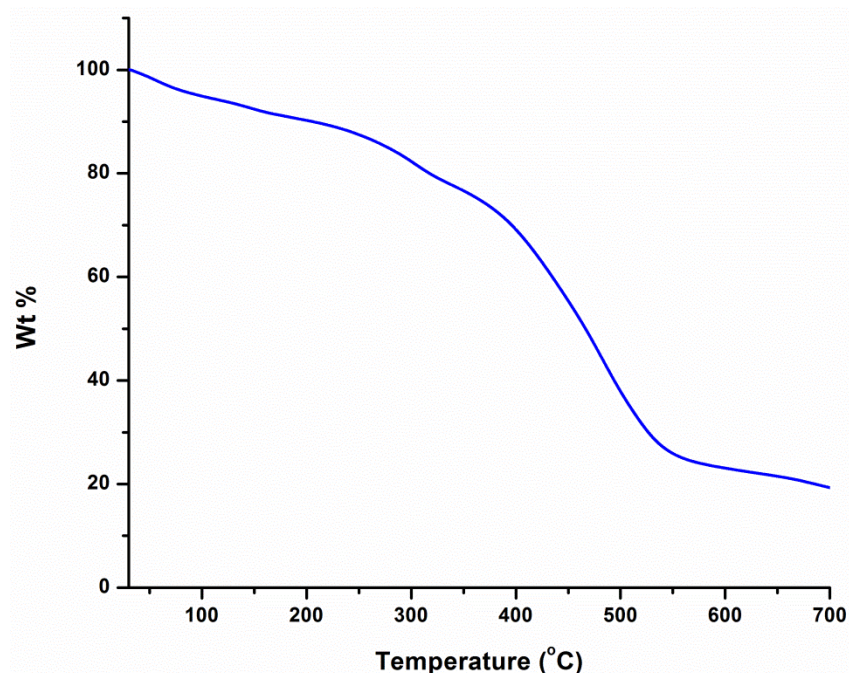
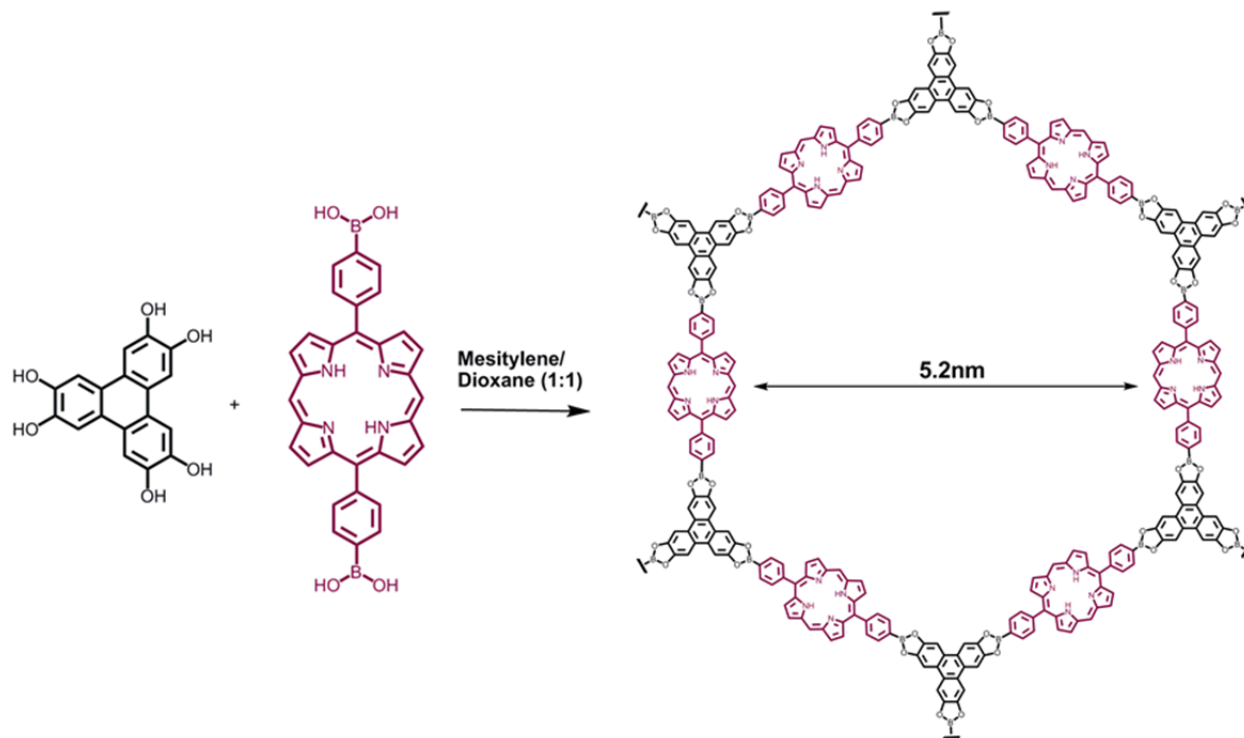


Figure 44. TGA of COF obtained up to 700°C using a linear 3 °C/min ramp method

2.3 Synthesis and characterization of HHTP-PorDBA COF

A Pyrex ampoule was charged with porphyrin diboronic acid (83 mg, 0.15 mmol), hexahydroxytriphenylene [(HHTP) 16 mg, 0.050 mmol] and 2 mL of a 1:1 (v:v) mixture of mesitylene: dioxane. The ampoule was flash frozen at 77 K (liquid N₂ bath) and evacuated and flame sealed. The reaction mixture was heated at 120 °C for 74 h to yield a free flowing purple powder. Isolated yield: 60 mg (79%). Elemental analysis (%) calcd. for HHTP-PorDBA COF [C₅₀H₂₆B₃N₄O₆]_n Theory: C, 74.03; H, 3.23; N, 6.91, found: C, 62.5; H, 3.96; N, 7.34. Elemental analysis of boronate COFs generally give lowered carbon values from the formation of non-combustible boron carbide byproducts.



Scheme 7. Synthesis of HHTP-PorDBA COF from 5, 15 porphyrin diboronic acid and HHTP.

2.3.1 Powder X-ray diffraction and simulation of HHTP-PorDBA COF

Powder X-ray diffraction (Cu K α radiation) was utilized to find out the crystalline nature of the as-synthesized HHTP-PorDBA COF. The experimental diffraction pattern (Figure 49) displays an intense diffraction peak at a 2θ angle (d -spacing) of 1.9° (45.7 \AA), and less intense peaks at 3.4° (26.3 \AA), 3.9° (22.8 \AA), 6.8° (13.19 \AA), and a broad peak at 25.2° (3.52 \AA). With the experimental cell parameters of $a = 51.8 \text{ \AA}$ and $c = 3.45 \text{ \AA}$, this pattern was manually indexed into a primitive hexagonal unit cell similar to other primitive hexagonal reported COF-5 and HHTP-DPB COFs. Using the Materials Studio modeling suite of programs, crystal models were generated, from eclipsed stacking sheets of HHTP-PorDBA COF (Figure 49 inset) in a **hnn** net using the space group $P6/mmm$, resulting in simulated cell parameters of $a = 52.7 \text{ \AA}$ and $c = 3.53 \text{ \AA}$, which match the indexed values. The simulated powder X-ray diffraction pattern also matched well with the measured pattern (Figure 49). The powder XRD pattern of

HHTTP-PorDBA COF was subjected to Pawley refinement which produced refined PXRD curves with lattice parameters of $a = 52.4 \text{ \AA}$ and $c = 3.48 \text{ \AA}$ with good residuals (see below).

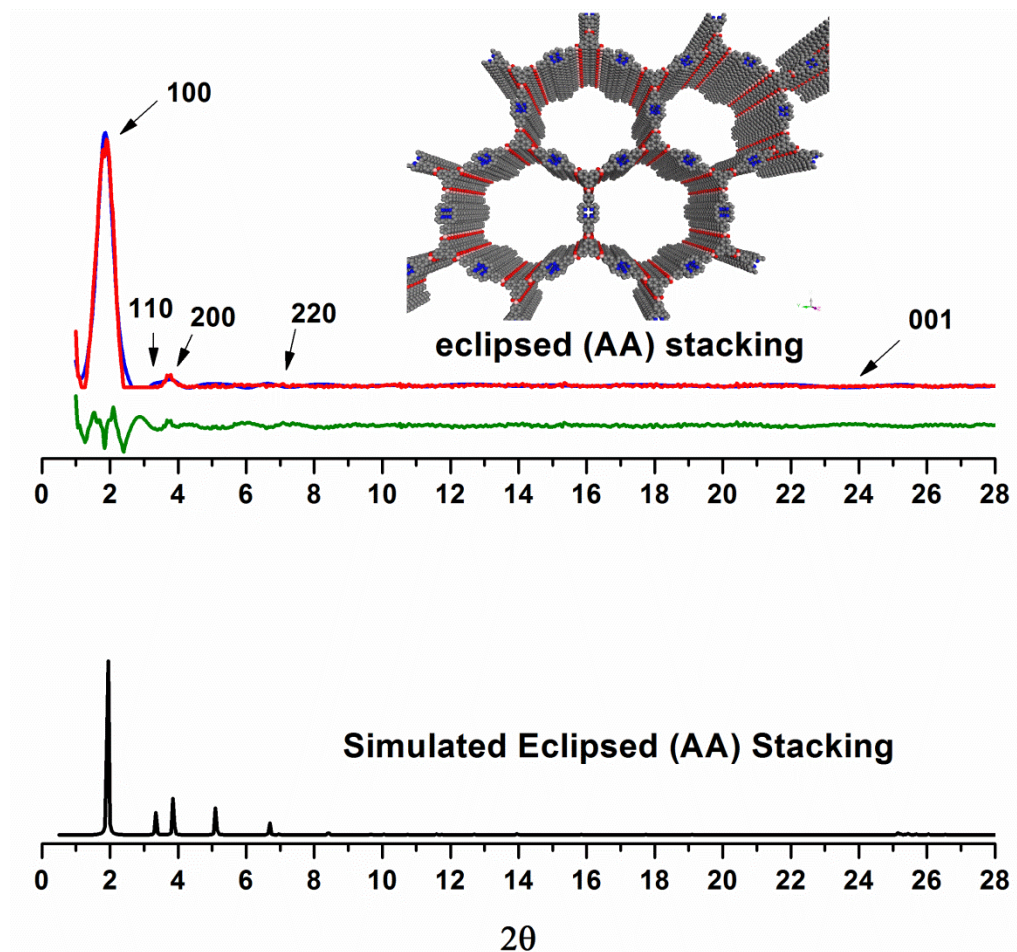
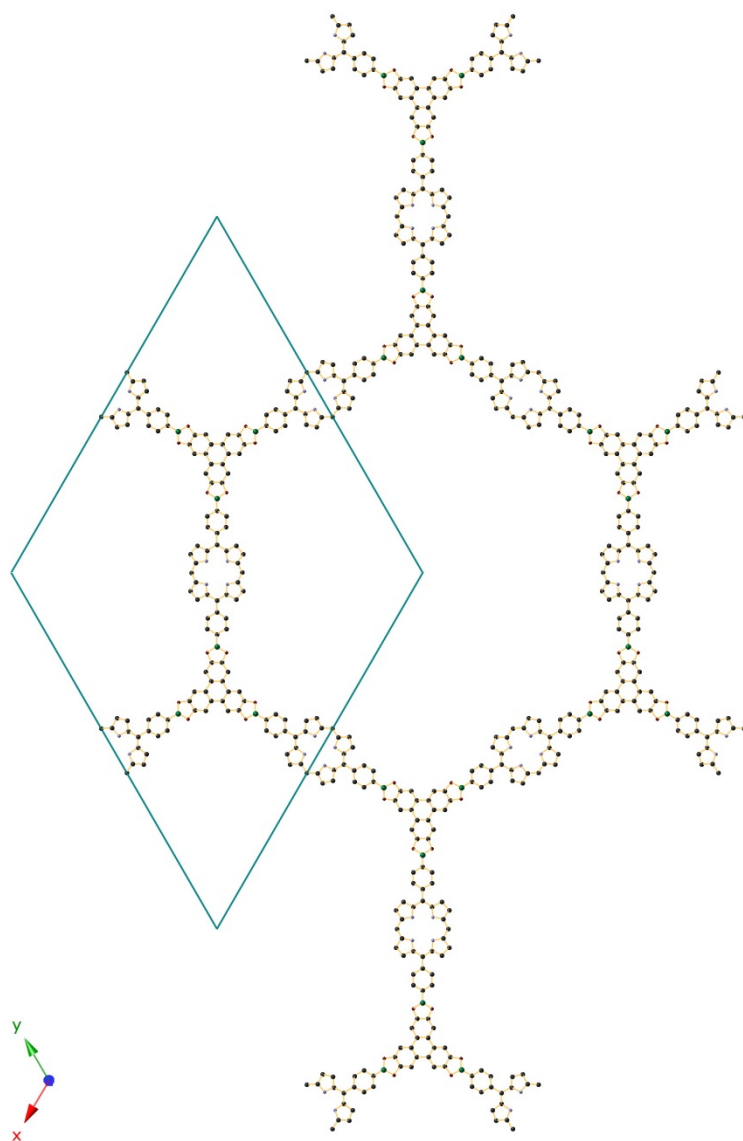


Figure 45. XRD pattern of HHTTP-PorDBA COF with the observed pattern in blue, Pawley refined profile in red, and the difference plot in green (observed minus refined profiles). The simulated XRD pattern from the proposed models is shown in black (below). Inset: Eclipsed stacking representation of HHTTP-PorDBA COF based on powder diffraction and modeling projected along the c axis.

Simulation and Refinement of the HHTTP-PorDBA COF

Geometry optimization and Pawley refinement of the HHTTP-PorDBA COF was carried out with Accelrys MS Modeling 4.3 using Reflex module. The unit cell dimensions were calculated from the geometrical parameters from the optimized structure. Pawley refinement was performed to optimize the lattice parameters iteratively until the R_{WP} value converges. After Pawley refinement the peak profile was refined using the Pseudo-Voigt peak shape function and whole profile fitting was done using Berrar

- Baldinozzi function for asymmetry correction during the refinement processes. The final R_{WP} and R_P values were 8.45% and 12.81%, respectively. The unit cell parameters were first calculated and then refined from the experimentally observed peak positions, as a result we obtained cell parameters of $a = b = 52.4 \text{ \AA}$ and $c = 3.48 \text{ \AA}$. Simulated PXRD patterns were calculated for an eclipsed arrangement of $P6/mmm$ space group, where all atoms in an each layer of the framework lay over one another.



Refined unit cell parameters and fractional atomic coordinates for HHTTP-PorDBA COF.

HHTTP-PorDBA COF	a (Å)	c (Å)
MS modeling	52.77	3.53
Pawley refinement	52.4	3.48

	B	C	N	O
C1	2	0.46101	0.53899	2.5
C2	2	0.44426	0.55574	0.5
C3	2	0.41319	0.58681	0.5
B4	1	0.39623	0.60377	0.5
C5	2	0.44366	0.60195	0.5
C6	2	0.4588	0.58654	0.5
C7	2	0.49224	0.55445	0.5
N8	3	0.50905	0.54174	0.5
C9	2	0.50987	0.58465	0.5
C10	2	0.53839	0.59086	0.5
C11	2	0.53685	0.56414	0.5
C12	2	0.33372	0.63935	0.5
C13	2	0.33386	0.61272	0.5
C14	2	0.36056	0.61342	0.5
O15	4	0.36427	0.58925	0.5
C16	2	0.56191	0.56191	0.5

2.3.2 FT-IR measurements of HHTTP-PorDBA COF

Fourier transform infrared spectroscopy (FTIR) indicated boronate ester formation, as evidenced by a sharp B–O stretch located at 1340 cm^{-1} not found in either of the reactants. The spectrum also showed strongly attenuated hydroxyl stretches. Spectra taken prior to activating the pores show intense

–CH₃ stretches of toluene or mesitylene, which disappear upon heating the COF at 90^oC under vacuum for 72 h.

Peak (cm ⁻¹)	Assignments
3400-3360 (w)	O–H stretch of the end-groups B(OH) ₂ or OH
1610 (s)	C=C stretch for phenyl ring
1480	C=N stretch of Pc macrocycles
1520 (w) 1490 (w)	Skeletal vibration of porphyrin ring
1340 (m)	C=C vibration of phenyl ring
1355 (s)	B–O stretch (boronic ester)
1260 (w)	C–B stretch
1201 (w)	C–H in plane deformation
1135 (s)	C–O stretch (characteristic band for boronic ester)
862 (w)	C–H out of plane deformation of <i>p</i> -substituted benzene
742 (w) 737 (w) 656 (w)	C–H out of plane deformation

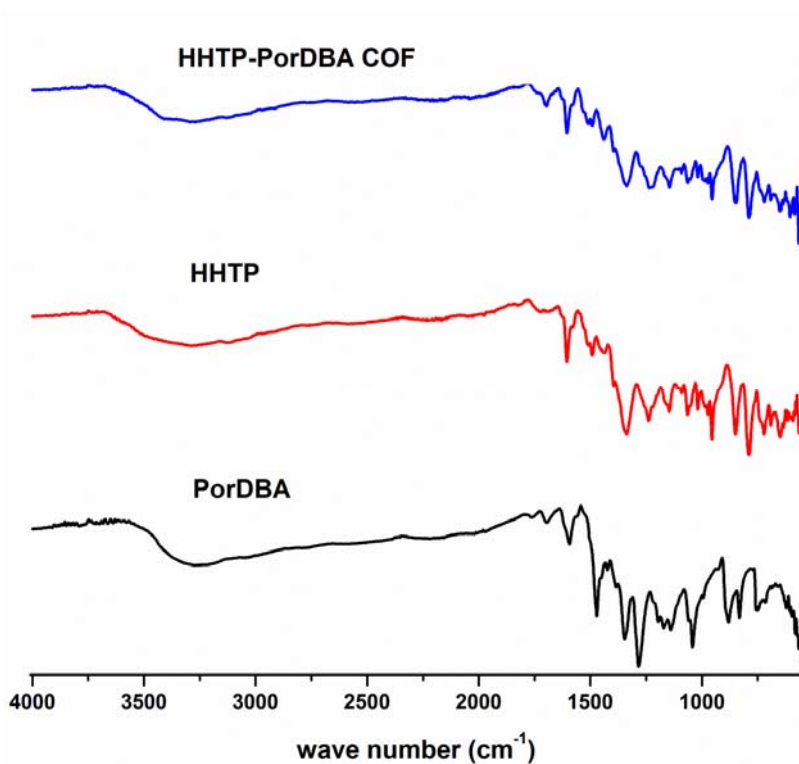


Figure 46. IR spectra of (OH)₈Pc Co(II) (blue), CoPc-PorDBA COF (black) and 5, 15 porphyrin diboronic acid (red).

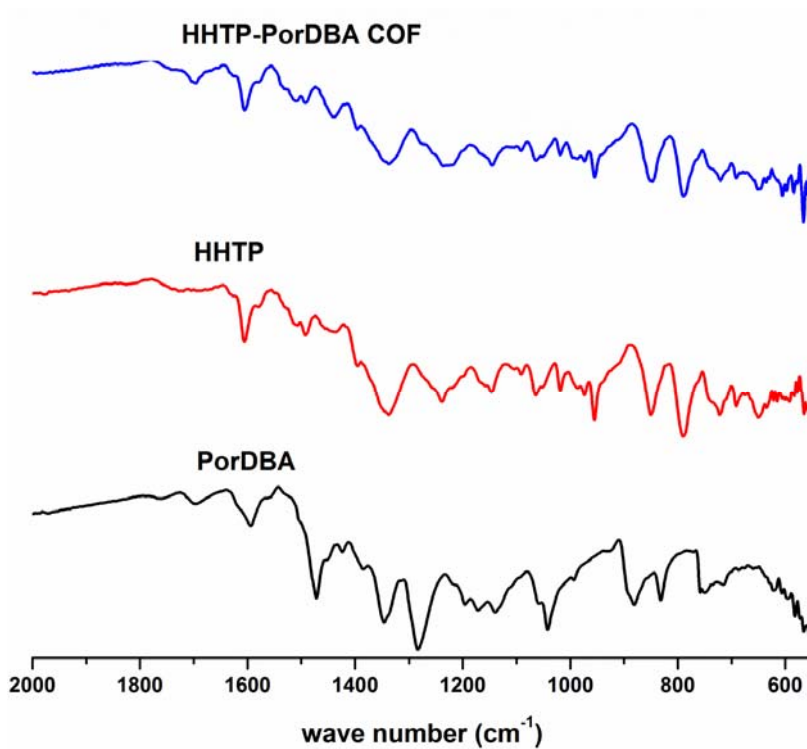


Figure 47. IR spectra of (OH)₈Pc Co(II) (blue), CoPc-PorDBA COF (black) and 5, 15 porphyrin diboronic acid (red).

2.3.3 Gas adsorption measurements of HHTP-PorDBA COF

The porous nature of the HHTP-PorDBA COF was further evaluated by N₂ and H₂ uptake measurements at 77 K/1 bar and CH₄ and CO₂ at 273K, 298K /1bar. The fully reversible N₂ isotherm depicted in Figure 52a shows a steady uptake at low pressure (0–0.1 bar) with a step size at around 0.43 indicating a permanent mesoporous nature and a gradual increase at higher pressures (0.1–1bar). A surface area of 205 m² g⁻¹ was obtained by applying the BET (Brunauer-Emmett-Teller) model within the pressure range of 0–1bar. These values are lower than those of mesoporous boronate ester based covalent organic frameworks such as HHTP-DPB COF. Pore size distribution was estimated by fitting the N₂ uptake isotherms using NLDFT and found the pore size value around 50 Å (Figure 53) and the pore volume from single point measurements was calculated to be 0.55cm³ g⁻¹(P/P₀ = 0.1). As we stated earlier, crystalline boronate ester based COFs were not explored for CO₂ adsorption properties. To investigate the impact of these parameters on the uptake of small gases such as H₂, CH₄ and CO₂ and the selective CO₂ adsorption over CH₄, we measured isotherms (Figure 52) and calculated their isosteric enthalpies of adsorption (Q_{st}) from Henry's constants (Figure 53) and compared these values to those of recently reported boronate ester based covalent organic frameworks such as COF-103.

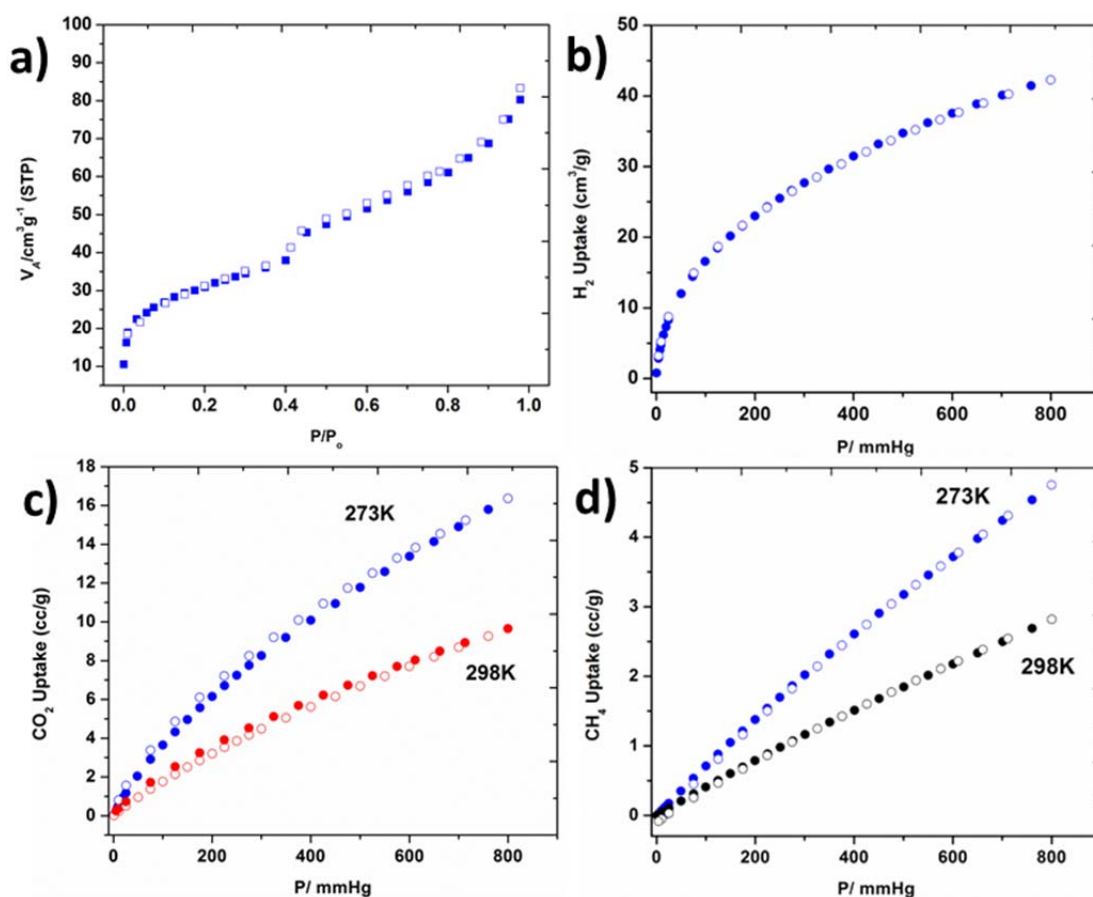


Figure 48. (a) N₂ at 77K (b) Hydrogen at 77K (c) CO₂ at 273K and 298K (d) CH₄ at 273K and 298K adsorption (filled symbols) and desorption (empty symbols) isotherm curves.

The H₂, CO₂ and CH₄ isotherms are fully reversible and exhibit a gradual rise at low pressures. The HHTP-PorDBA showed a low CO₂ uptake of 3.1 wt% at 273 K/1 bar which is lower than that of 2D and 3D boronate ester based COFs measured at 298K/60 bar.¹² To determine the binding affinity of HHTP-PorDBA COF for CO₂, we calculated the Q_{st} using the Van't Hoff equation (20.4kJ mol⁻¹). These values are slightly lower than those reported for 2D and 3D COFs in general but considerably lower than those of nitrogen-rich MOFs. The readily reversible sorption/desorption behavior and moderate Q_{st} indicate that CO₂ interactions with pore walls are weak enough to allow for material regeneration without applying heat. We have also measured the H₂ and CH₄ storage properties of HHTP-PorDBA COF. The H₂ uptake was only 0.35 wt % at 77 K and 1 bar (Figure 52b), which is lower

than for other reported boronate and imine linked covalent organic frameworks. Similarly, the measured CH₄ uptake was 0.34 wt% at 273K and 1 bar (Figure 52d).

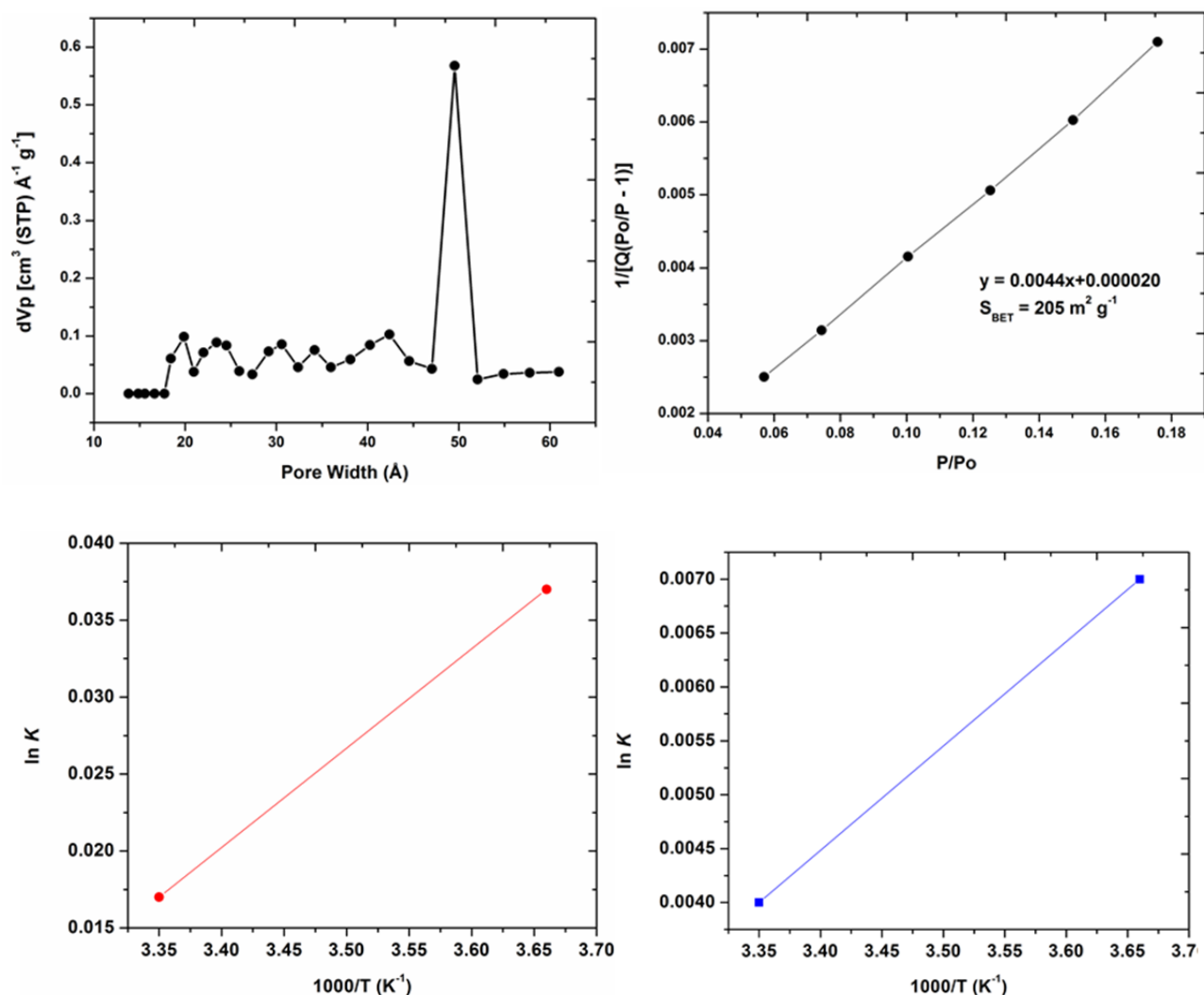


Figure 49. Van't Hoff plots of CO₂ (red) and CH₄ (blue).

Both isotherms are completely reversible and exhibit a gradual rise at low pressure and reach maxima of 12–31 mg g⁻¹ at 273 K and 7–18 mg g⁻¹ at 298 K. The Q_{st} for CH₄ was calculated by using adsorption data collected at 273K. At zero coverage, the Q_{st} is 16.2 kJ mol⁻¹. Based on these values we compared the CO₂ uptake and selectivity over CH₄ to evaluate the potential use of HHTP-PorDBA COF for CO₂ adsorption. At 273 K and 1bar, the CO₂ uptake is 3.1 wt%, whereas that of CH₄ is only 0.34 wt%. This preferential higher affinity for CO₂ could be potentially useful for CO₂ capture. We

calculated the gas adsorption selectivities from the initial slope ratios estimated from Henry's constants (Figure 53).

Calculation of isosteric heat of adsorption

The adsorption enthalpy at zero coverage was calculated from Henry constant using the Van't Hoff equation as

$$\ln K = -\frac{\Delta H}{RT} + \frac{\Delta S}{R}$$

K is Henry constant, T is temperature, plotting $\ln K$ vs $1000/T$

2.3.4 Diffuse reflectance UV-Vis measurements of HHTP-PorDBA COF

The UV-Vis diffuse reflectance spectra (Figure 54) showed broad peaks between 200 and 800 nm with maximum at 420 nm, which is a characteristic for porphyrins, whereas three separated bands with maxima at 560 nm, 590 and 620nm were observed. The presence of porphyrin units in the HHTP-PorDBA was confirmed by the appearance of Soret (450nm) and Q bands (510, 550, 582, and 638nm).

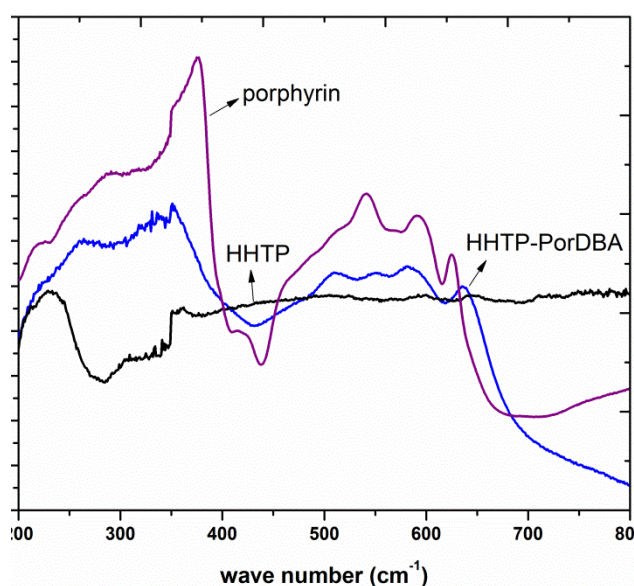


Figure 50. Solid-state absorption spectra HHTP-PorDBA COF (blue), HHTP (black) and PorDBA (purple) as powders using a praying mantis diffuse reflectance accessory. Small, jagged peaks around 340nm are due to instrument lamp shift.

2.3.5 Scanning electron microscopy images of HHTP-PorDBA COF

The HHTP-PorDBA COF particles were uniform spheres with 1 μm diameters, as observed by scanning electron microscopy (SEM, Figure 55).

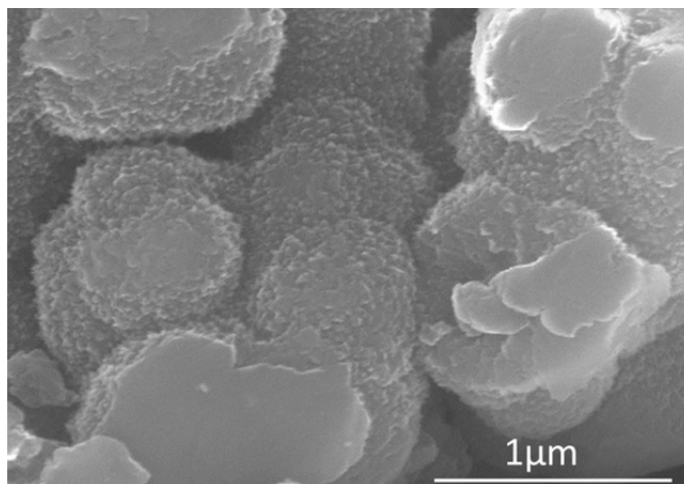


Figure 51. Scanning electron microscope image of the HHTP-PorDBA COF.

2.3.6 Thermogravimetric analysis of HHTP-PorDBA COF

The HHTP-PorDBA COF retained 92% of its mass up to 350 $^{\circ}\text{C}$ by thermal gravimetric analysis (TGA, Figure 56).

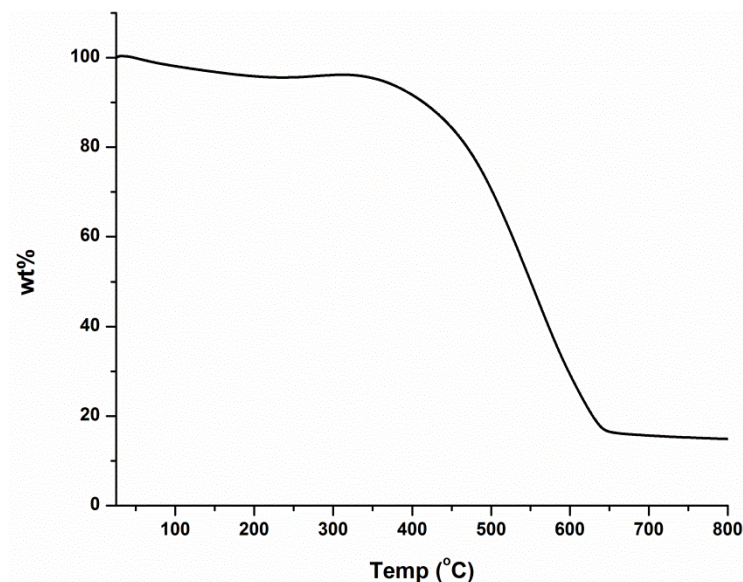


Figure 52. TGA of HHTP-PorDBA COF obtained up to 700 $^{\circ}\text{C}$ using a linear 10 $^{\circ}\text{C}/\text{min}$ ramp method.

2.4 H₂ and CH₄ storage properties of CoPc-PorDBA, CoPc-BPDA and HHTP-PorDBA COFs

COF	H ₂	CH ₄	PORE VOLUME	PORE SIZE
CoPc-PorDBA	0.8 wt%	0.6 wt%	0.88cm ³ g ⁻¹	35nm
CoPc-BPDA	1.2 wt%	0.45	0.573cm ³ g ⁻¹	27nm
HHTP-PorDBA	0.35 wt%	0.21 wt%	0.35cm ³ g ⁻¹	52nm

Conclusions

The syntheses of the following COFs CoPc-PorDBA, CoPc-BPDA, and HHTP-PorDBA were achieved and these were shown to possess crystalline frameworks under solvothermal conditions. We have prepared three boronate ester based covalent organic frameworks and investigated their potential for H₂ storage. Also, we connected two very good electron donors, a phthalocyanine and a porphyrin, both of which are able to absorb in the UV-Vis spectrum. By varying the pore sizes we obtained crystalline frameworks with different pore volumes and good surface areas. The resulting COFs are chemically and thermally stable and exhibit good H₂ uptake (up to 1.25 mmol g⁻¹). The pore sizes of the frameworks were shown to have a profound effect on the H₂ and CH₄ storage properties. This study also suggests that the difference in the H₂ uptake ability between the three COF structures can be attributed to their pore volumes (Table 2.4) as well as to the degree of gas–solid interactions, which is indicated by the isosteric heats of adsorption (Q_{st}), calculated based on the Van't Hoff equation.

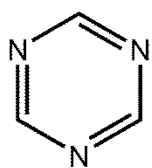
References

- 1) W. C. Sailor, D. Bodansky, C. Braun, S. Fetter, B. van der Zwaan, *Science.*, 2000, **288**, 1177.
- 2) J. A. Turner, *Science.*, 1999, **285**, 687.
- 3) L. Pan, M. B. Sander, X. Huang, J. Li, M. Smith, E. Bittner, B. Bockrath, J. K. Johnson, *J. Am. Chem. Soc.*, 2004, **126**, 1308.
- 4) L. Pan, H. Liu, X. Lei, X. Huang, D. H. Olson, N. J. Turro, J. Li, *Angew. Chem., Int. Ed.*, 2003, **42**, 542.
- 5) J-Y. Lee, L. Pan, S. P. Kelly, J. Jagiello, T. J. Emge, J. Li, *Adv. Mat.*, 2005, 17, 2703.
- 6) S. B. Kalidindi, H. Oh, M. Hirscher, D. Esken, C. Wiktor, S. Turner, G.V. Tendeloo, and R. A. Fischer, *Chem. Eur. J.*, 2012,18, 10848
- 7) J. L. Mendoza-Cortes, W. A. Goddard, H. Furukawa and O. M. Yaghi, *J. Phys. Chem. Letts.*, 2012, **3**, 2671.
- 8) Han, S. S.; Goddard, W. A., *J. Am. Chem. Soc.*, 2007, **129**, 8422.
- 9) J-H. Guo, H. Zhang, Z-P. Liu, and X-L. Cheng, *J. Phys. Chem., C* 2012, 116, 15908.
- 10) J-H. Guo, H. Zhang, and Y. Miyamoto, *Phys. Chem. Chem. Phys.*, 2013, **15**, 8199.
- 11) J. Xia, S. Yuan, Z. Wang, S. Kirklin, B. Dorney, D-J Liu, and L. Yu, *Macromolecules.*, 2010, **43**, 3325.
- 12) H. Furukawa and O. M. Yaghi, *J. Am. Chem. Soc.*, 2009, **131**, 8875.
- 13) J. Metz, O. Schneider, and M. Hanack, *Inorg. Chem.*, 1984, **23**, 1065.
- 14) E. L. Spitler and W. R. Dichtel, *Nat. Chem.*, **2010**, 2, 672.
- 15) X. Ding, J. Guo, X. Feng, Y. Honsho, J. Guo, S. Seki, P. Maitarad, A. Saeki, S. Nagase, and D. Jiang, *Angew. Chem., Int. Ed.*, 2011, **50**, 1289.
- 16) E. L. Spitler, J. W. Colson, F. J. Uribe-Romo, A. R. Woll, M. R. Giovino, A. Saldivar, and W. R. Dichtel, *Angew. Chem., Int. Ed.*, 2012, **51**, 2623.

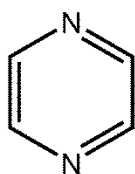
- 17) V. S. P. K. Neti, X. Wu, S. Deng and L. Echegoyen, *CrystEngComm.*, 2013, **15**, 6892.
- 18) V. S. P. K. Neti, X. Wu, M. Hosseini, R. Bernal, S. Deng and L. Echegoyen, *CrystEngComm.*, 2013, **15**, 7157.
- 19) V. S. P. K. Neti, X. Wu, S. Deng and L. Echegoyen, *manuscript in preparation*
- 20) M. O’Keeffe, M. A. Peskov, S. J. Ramsen, O. M. Yaghi *Acc. Chem. Res.*, 2008, **41**, 1782.

Chapter 3

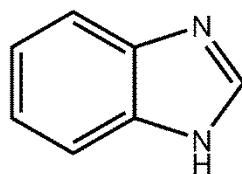
Impact of basicity on CO₂ adsorption of porous organic polymers



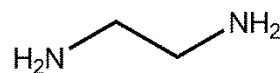
1,3,5 triazine
barely basic



pyrazine
pKa = 0.65



benzimidazole
pKa = 5.53



ethane 1,4-diamine
pKa = 10.7

Introduction

A sub-group of porous organic polymers (POPs) with pore dimensions less than 2 nm are referred to as microporous organic polymers.¹⁻⁵ They exhibit similar sorption properties to other porous materials such as metal organic frameworks (MOFs) and covalent organic frameworks (COFs) and zeolites.⁶⁻¹⁰ However, they exhibit some advantageous features over COFs and MOFs.¹¹⁻¹² For example, POPs can incorporate nitrogen rich building blocks that adsorb CO₂ more strongly than other types of sorbents.¹³⁻¹⁵ These materials have attracted significant attention due to their ability to capture CO₂ through R=N(δ^-)-C(δ^+)O₂ interactions.¹⁶ C-N linkages can also be found in other types of crystalline and amorphous materials such as triazine¹⁷ and hydrazone¹⁸ based frameworks. These also contain micro or meso pores that allow CO₂ to effectively access the interior space. The synthesis of these POPs is simple, highly reproducible and cost-effective.¹⁹ Additionally, the pore properties can be modified systematically to develop these materials for H₂ and CH₄ storage as well.

Recent simulations have proposed benzimidazole linked porous polymers (BILPs) as promising candidates for CO₂ adsorption.²⁰⁻²² Although high pressures are typically needed for relatively high gravimetric and volumetric H₂ and CH₄ storage, this is not necessary for CO₂ capture. MOFs²³ and some of the POPs²⁴ have already achieved enhanced gas storage values at low and high pressures, hence the development of robust π -electron rich and nitrogen containing conjugated materials with relatively high gas uptake capacities is a promising endeavor. Even though MOFs possess many advantages such as large surface areas, tunable structures and convenient post-synthetic modifications, they suffer from limited stability, which limit their practical applications.

The POPs presented in this chapter have both interpenetrated and non-interpenetrated two dimensional (2D) micro and meso porous structures. All of these materials have 2D open channels but

their pore size varies. This chapter is focused on the rational design and synthesis of three porous organic polymers using porphyrin, triphenylbenzene, and phthalocyanine building blocks connected through imine, bisbenzothiazole, and triazole linkages. The studies are based upon a synthetic strategy to achieve materials having high nitrogen content and various types of linkages lacking the frameworks to differ basicity of the framework. The formation of frameworks using imine, imine-benzothiazole, and triazole linkages affects the porosity and the amount of CO₂ adsorption. The CuPor-BPDC (copper porphyrin-biphenyl dicarboxaldehyde), IBTP (imine benzothiazole polymer) polymers were constructed from the Schiff base condensation reaction between meso-tetraphenylamino porphyrin and 4, 4'-biphenyl dicarboxaldehyde (CuPor-BPDC, Scheme 5) and 1,3,5 tris (4-formylphenyl)-benzene and 2,6-diaminobenzo bithiazole (IBTP, Scheme 9). The Pc-POP was obtained from the “click” chemistry reaction between tetraazidophthalocyanine Co(II) and diethynylbenzene (Scheme 12).

The synthesis of CuPor-BPDC was carried out solvothermally in a mixture of mesitylene and dioxane (1:1, v:v) in a sealed glass ampoule at 120 °C for 72 h. Whereas the IBTP and Pc-POP were synthesized in dimethylsulfoxide (DMSO) and dimethylformamide (DMF) mixtures under reflux conditions. The chemical connectivity and composition of all the POPs presented here were characterized by several analytical methods such as Fourier-Transform infrared spectroscopy (FT-IR), solid-state ¹¹B and ¹³C CP-MAS NMR, powder X-ray diffraction (PXRD), BET surface area measurements, scanning electronic microscopy (SEM), diffuse reflectance UV-Vis, and elemental analysis.

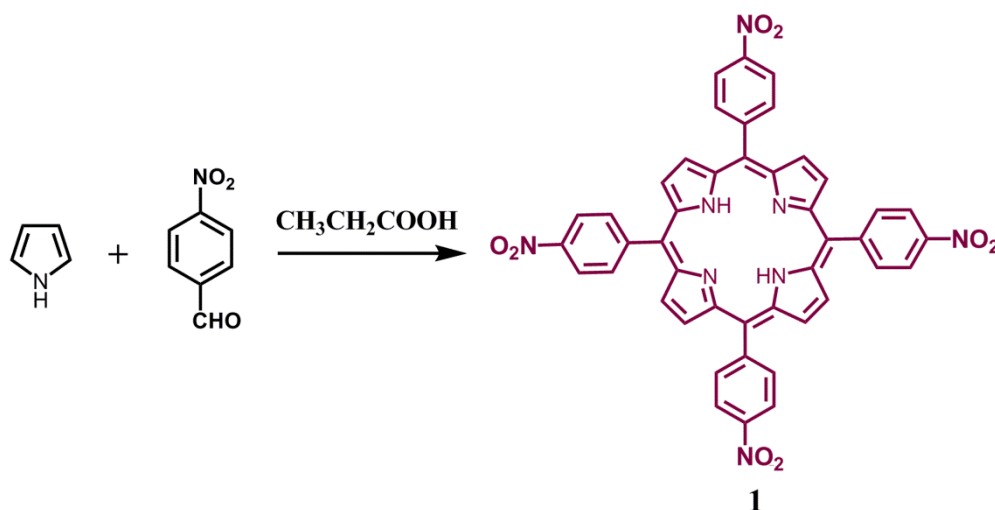
Experimental Methods

All chemicals and solvents were purchased from Sigma-Aldrich or Alfa Aesar. Fourier transform Infrared (FT-IR) spectra were recorded on a Perkin-Elmer Spectrum one infrared spectrometer (ATR). ^1H NMR spectra were recorded on JEOL 600MHz spectrometer, where chemical shifts (δ in ppm) were determined with a residual proton of the solvent as standard. Matrix-assisted laser desorption ionization time-of-flight mass (MALDI-TOF MS) spectra were recorded on Bruker benchtop microflex model using matrix trihydroxyanthracene. Field-emission scanning electron microscopy (FE-SEM) was performed on a Hitachi S-4800 fitted with an EDAX energy-dispersive spectrometry system by adhering sample on a sampling platform. Powder X-ray diffraction (PXRD) data were recorded on a Bruker DiscoverD8 model diffractometer by depositing powder on plastic substrate, from $2\theta = 1^\circ$ up to 30° with 0.05° increment. In order to determine pore textural properties including the specific Brunauer–Emmet–Teller (BET) surface area, pore volume and pore size distribution, nitrogen adsorption and desorption isotherm on CuPor-BPDC, IBTP, and Pc-POP samples at 77 K were measured in an ASAP-2020 adsorption apparatus (Micromeritics). The as-synthesized samples were degassed in situ at 150°C with a heating rate of $3^\circ\text{C}/\text{min}$ under a vacuum (0.0001 mmHg) for 12 h before nitrogen adsorption measurements in order to ensure the micro-channels in the structure were guest-free. The Brunauer–Emmett–Teller (BET) method was utilized to calculate the specific surface areas by using the non-local density functional theory (NLDFT) model, the pore volume was derived from the sorption curve. Thermogravimetric analysis from $30\text{--}700^\circ\text{C}$ was carried out on a Mettler-Toledo thermogravimetric analyzer in an N_2 atmosphere using a $3^\circ\text{C}/\text{min}$ ramp time.

3.1 Synthesis and characterization of precursors of CuPor-BPDC

Synthesis of meso-tetra (4-nitrophenyl) porphyrin (1):

4-Nitrobenzaldehyde (22.0 g, 1.45×10^{-1} mol) and acetic anhydride (24.0 mL, 2.54×10^{-1} mol) was dissolved in propionic acid (600 mL). The solution was then refluxed, to which pyrrole (10.0 mL, 1.44×10^{-1} mol) was slowly added. After refluxing for 30 min, the resulting mixture was cooled to give a precipitate which was collected by filtration, washed with H₂O and methanol, and dried under vacuum. The resulting powder was dissolved in pyridine (160 mL) which was refluxed for 1 h. After cooling, the precipitate was collected by filtration and washed with acetone to give 5,10,15,20-tetrakis(4-nitrophenyl)-21*H*,23*H*-porphine (**1**) as a purple crystals in 14% yield.

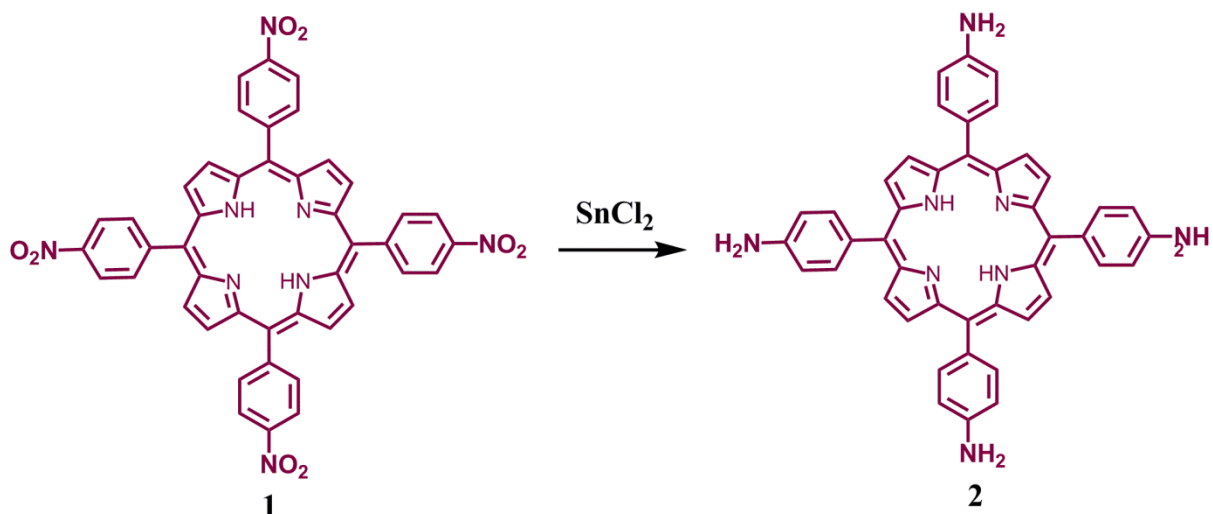


Scheme 1. Synthesis of meso-tetra (4-nitrophenyl) porphyrin from 4-nitrobenzaldehyde and pyrrole.

Synthesis of meso-tetra (4-aminophenyl) porphyrin (2):

The product (**1**, 4.13 g, 5.19×10^{-3} mol) was dissolved in hot HCl (500 mL) at 70°C, to which was added SnCl₂·2H₂O (18.0 g, 7.97×10^{-2} mol). The resulting mixture was stirred at 70°C for 30 min and then cooled to 0°C. After neutralization with aqueous NH₃, the resulting gray crystalline product was collected by filtration and dissolved in acetone. Rotary evaporation of the solution followed by drying under vacuum yielded **2** as a purple crystal. Yield: 92%. ¹H NMR (CDCl₃, 300 MHz, ppm): δ -

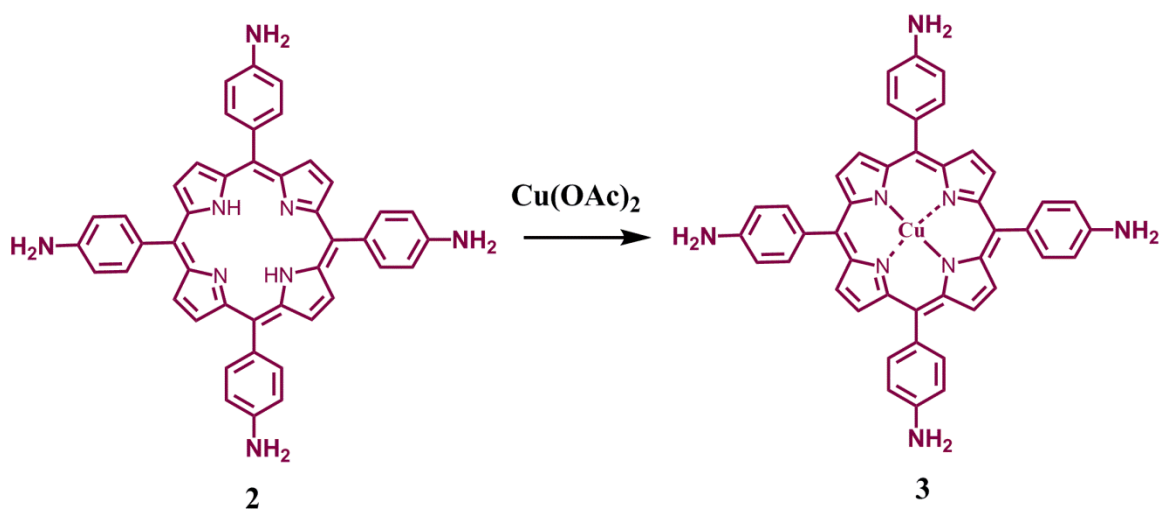
2.7 (s, 2H), 4.0 (s, 8H), 7.1–8.0 (m, 16H), 8.9 (s, 8H). MALDI-MS (trihydroxyanthracene, m/z): Calcd for M^+ 674.8; Found 675.



Scheme 2. Synthesis of meso-tetra (4-aminophenyl) porphyrin from meso-tetra (4-nitrophenyl) porphyrin.

Synthesis of meso-tetra (4-nitrophenyl) porphyrin Cu(II) (3):

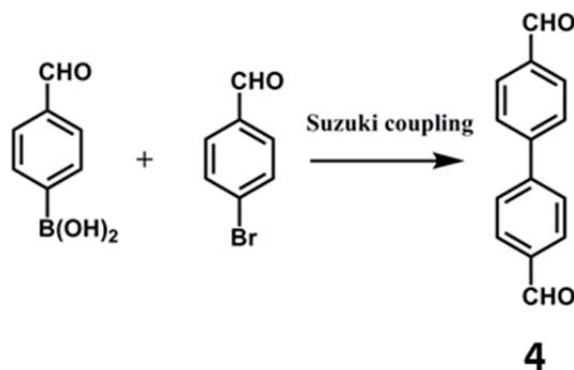
The ligand **2** (100 mg, 6.84×10^{-5} mol) and $(\text{CH}_3\text{COO})_2\text{Cu} \cdot 4\text{H}_2\text{O}$ (20.5 mg, 8.20×10^{-5} mol) were dissolved in DMF (20 mL), and the solution was refluxed for 1 h under argon. After cooling to room temperature, the resulting precipitate was collected by filtration, washed with H_2O and CH_3OH , and dried under vacuum to yield CuTAPP (**3**) as red crystals. Yield: 84%.



Scheme 3. Synthesis of CuTAPP from meso-tetra (4-aminophenyl) porphyrin.

Synthesis of 4,4'-biphenyldicarboxaldehyde (4):

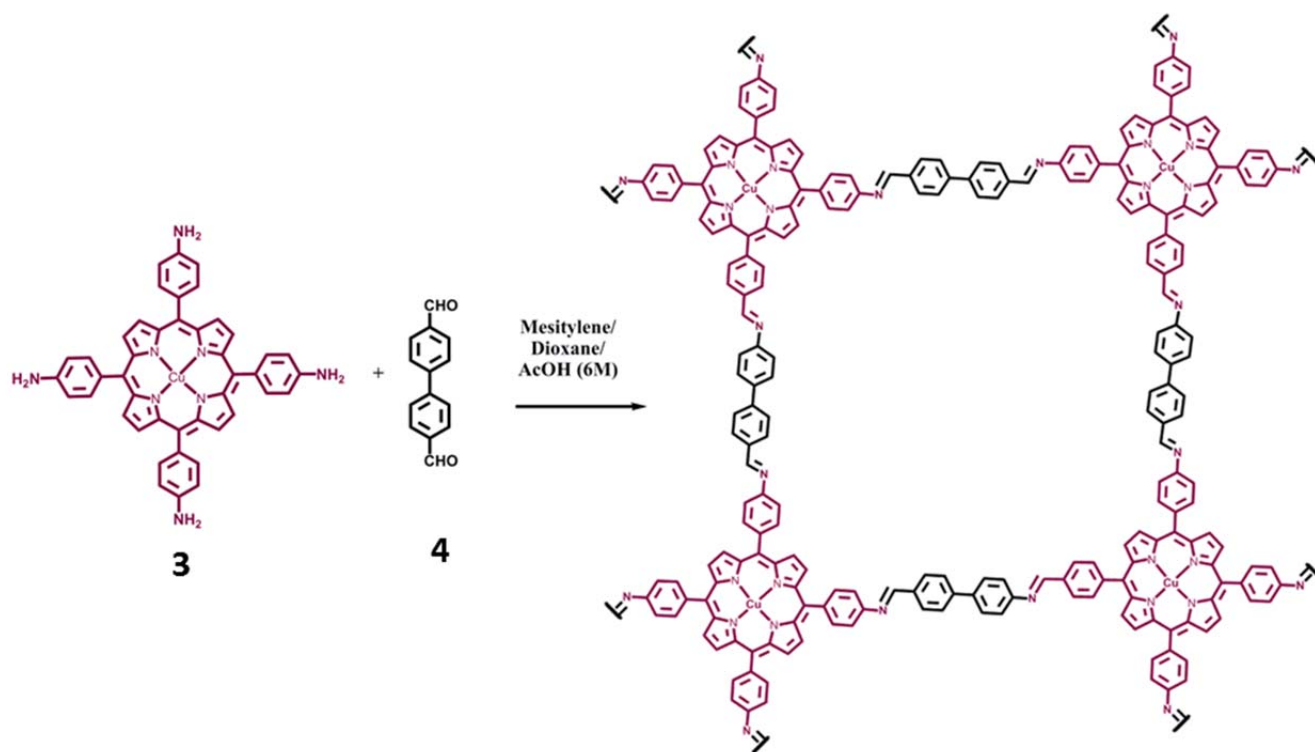
4-formylbromobenzene (5.0 g, 15.9 mmol), 4-formylphenyl boronic acid (14.3 g, 95.3 mmol), K_2CO_3 (13.2 g, 95.3 mmol), and palladium tetrakis (triphenyl phosphine) (0.92 g, 0.794 mmol) were added to a 200 mL dry tetrahydrofuran round bottom flask equipped with a stir bar and condenser. The flask was purged with N_2 after adding H_2O (30 mL). The resulting suspension was then heated to reflux for 48 h. The reaction mixture was cooled to r.t, and then added to dichloromethane. Organic phases were separated and concentrated. This solid was separated as a white solid after column chromatography with dichloromethane. These isolated white solids were combined to yield **2** (3.83 g, 62%). ^1H NMR matched with the reported one.



Scheme 4. Synthesis of 4,4'-biphenyldicarboxaldehyde from 4-formyldiboronic acid and 4-bromobenzaldehyde.

Synthesis and characterization of CuPor-BPDC

0.5ml of Mesitylene/0.5ml of absolute ethanol/0.1 ml of 6 M acetic acid were added to the mixture of CuPor (**3**, 0.02 mmol, 14.7 mg) and BPDC (**4**, 8.4 mg, 0.04 mmol), sonicated and degassed in a Pyrex ampoule (5 mL) using liquid N_2 bath. The ampoule was sealed off and heated at 120°C for 3 days. The precipitate at the bottom was filtered and washed with anhydrous dioxane and THF. The purple powder was dried at 100°C under vacuum overnight to give the corresponding partially crystalline polymer in 69% yield. Elemental analysis (%) calcd. for CuPor-BPDC ($\text{C}_{116}\text{H}_{68}\text{N}_{16}\text{Cu}$)_n. Theory: C, 76.85; H, 3.78; N, 12.36; found C, 75.95; H, 4.30; N, 11.48, respectively.



Scheme 5. Synthesis of CuPor-BPDC from 4,4'-biphenylboronic acid and CuTAPP.

3.1.1 Powder X-ray diffraction and simulation of CuPor-BPDC

Powder X-ray diffraction (Cu K α radiation) was employed to probe the solid-state packing and crystallinity of the as-synthesized CuPor-BPDC. The diffraction pattern (Figure 57) displays a low intensity diffraction peak at a $2\theta = 3^\circ$, and another very weak intense peak at 5.8, reflecting a mostly amorphous or partially crystalline CuPor-BPDC.

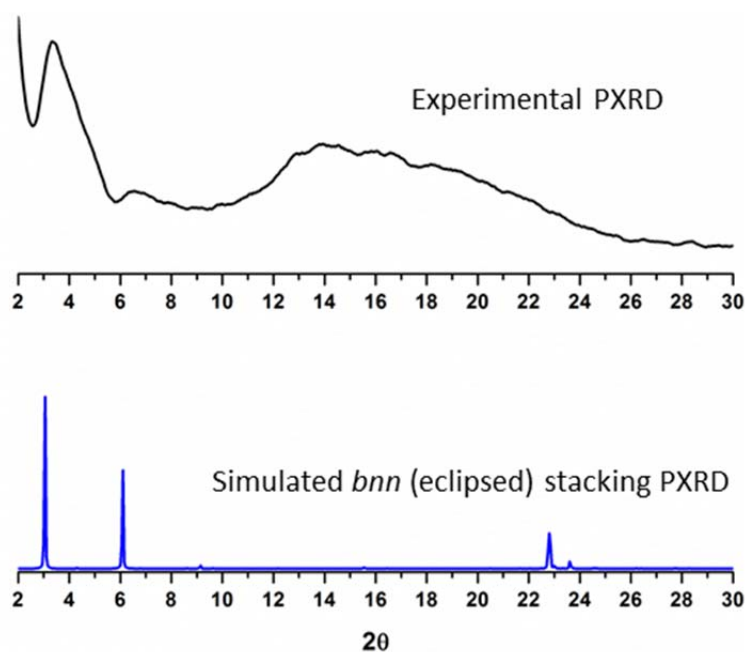


Figure 53. Powder X-ray diffraction pattern of CuPor-BPDC (above) and eclipsed stacking simulated PXRD pattern (below).

3.1.2 FT-IR measurements of CuPor-BPDC

The formation of imine bonds between **3** and **4** (see SI) was confirmed by FT-IR spectroscopy which exhibited a new characteristic C=N stretching frequency at 1690 cm^{-1} (Figures 58 and 59). The FT-IR spectrum showed highly attenuated -N-H and -C=O stretching frequencies from the meso-tetraphenylamino porphyrin and 4, 4' - biphenyl dicarboxaldehyde at 1500 cm^{-1} and 1740 cm^{-1} .

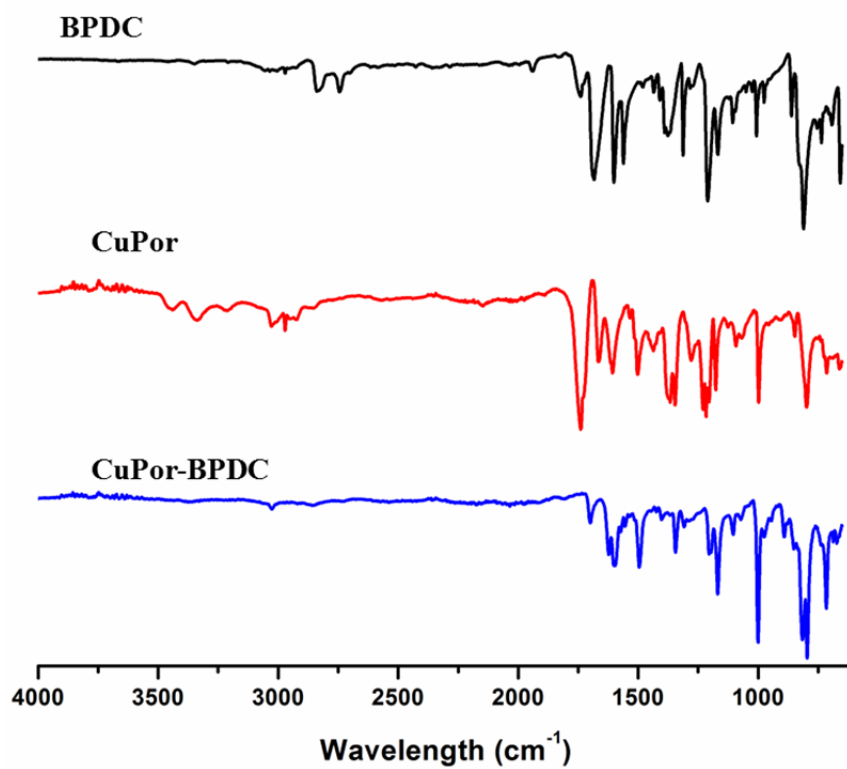


Figure 54. IR spectra of BPDC, meso-tetraphenylamino porphyrin, and CuPor-BPDC.

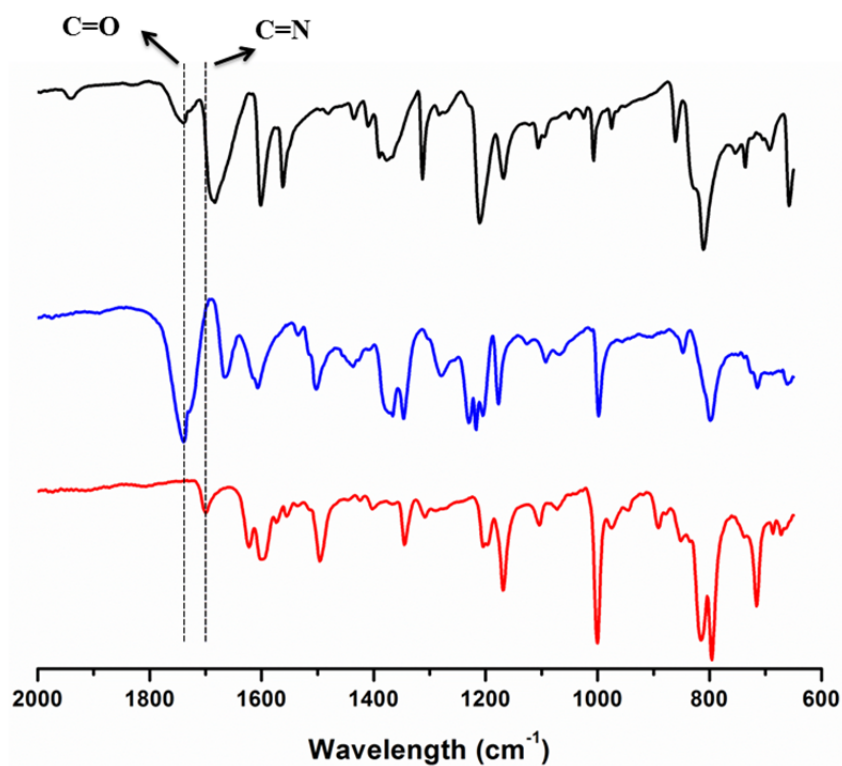


Figure 55. Expanded IR spectra of BPDC (black), meso-tetraphenylamino porphyrin (blue) and CuPor-BPDC (red).

3.1.3 Gas adsorption measurements of CuPor-BPDC

The gas adsorption capacities of CuPor-BPDC were found by measuring N₂ and H₂ adsorption/desorption isotherms at 77K, 1bar and 273K and 298K, 1 bar in the case of CH₄ and CO₂. The steady rise in N₂ uptake at low pressure (0–0.1bar) and the gradual increase at higher pressures (0.1–1bar) result in a type II shaped isotherm (Figure 60a), which is typical for microporous materials that show permanent microporosity. A surface area of 442 m² g⁻¹ was obtained by applying the Brunauer-Emmett-Teller (BET) model and a surface area of 933m² g⁻¹ was obtained by applying the Langmuir model within the pressure range of P/P₀ = 0–1bar. These values are comparable to those for other amorphous nanoporous organic polymer networks. The total pore volume and average pore size were calculated from the nitrogen isotherms by applying the nonlocal density functional theory (NLDFT) method, and found to be approximately 0.41cm³/g at single point adsorption (P/P₀ = 0.97) and 21 Å, (Figure 61). Efficient and selective separation of CO₂ from other gases in the atmosphere continues to be a major challenge. At present, organo amine solutions are commercial products used to capture CO₂. Porous solid adsorbents such as porous organic polymers are an alternative approach to amine solutions, because regeneration of the amine solutions requires considerable energy and they are also highly corrosive. We evaluated the adsorption properties and selectivity of CO₂, CH₄ and H₂ uptake by CuPor-BPDC at low pressures and different temperatures. At 273K/298K, 1.0 bar, CuPor-BPDC stores up to 5.5/3.2 wt% of CO₂ with good selectivity (5.6/4.7) over CH₄ under same conditions.

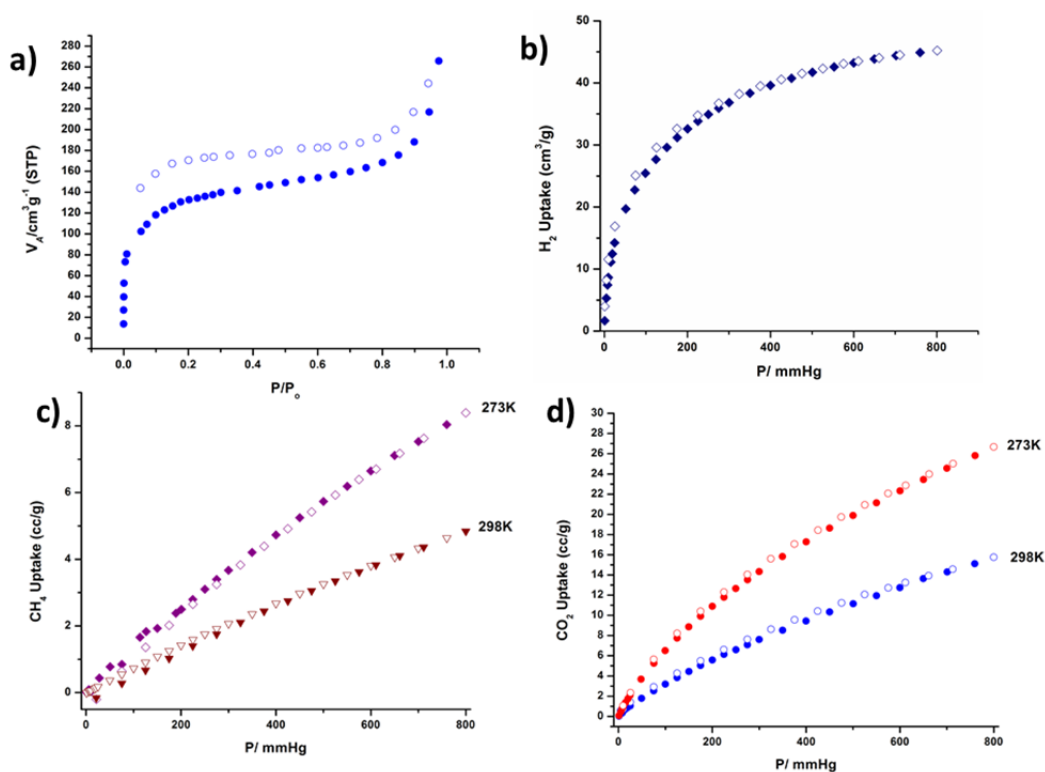


Figure 56. (a) Nitrogen at 77 K (b) Hydrogen at 77 K (c) CO_2 at 273 K and 298 K (d) CH_4 at 273 K and 298 K adsorption (filled symbols) and desorption (empty symbols) isotherm curves.

These likely results by donation of the nitrogen lone pair in the imine bond to carbon dioxide. The electron rich building blocks of CuPor-BPDC, connected by the imine bond pore walls are also interaction sites for CO_2 binding. Increasing the internal molecular free pore volume by expanding the length of the building blocks could enhance the porosity for the uptake of CO_2 . The CuPor-BPDC CO_2 uptake (1.25 mmol g^{-1}) is only slightly lower than for other imine-linked COFs ($1.36 \text{ mmol g}^{-1}/273\text{K}$, 1 bar), and significantly lower than for benzimidazole polymers which can store up 5.12 mmol g^{-1} at 273 K/1 bar. Low adsorption levels for H_2 (0.4 wt%, 77 K) and CH_4 (0.32 wt%, 298 K), as shown in Figures 60b and 60d, precluded its use as energy storage material. The H_2 uptake is lower than for many of the reported imine linked porous organic polymers under similar conditions, but considerably lower than those of the best performing metal organic frameworks and metal doped 2D or 3D COFs. The lower H_2 and CH_4 uptake capacity of CuPor-BPDC is consistent with its microporous nature that does not facilitate gas storage under low pressure.

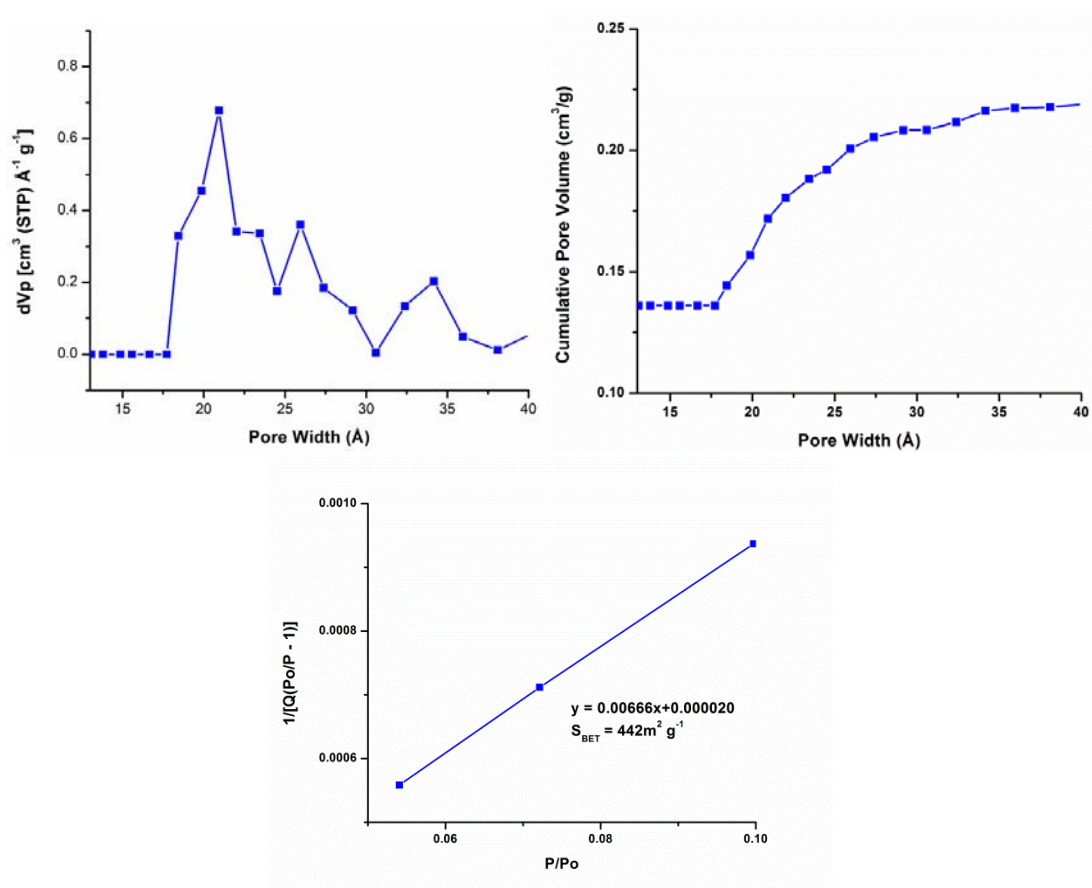


Figure 57. Differential (top left) and cumulative (top right) pore size distribution plot of CuPor-BPDC from the application of the NLDFT model to the N₂ isotherm. BET plot (below) for CuPor-BPDC calculated from isotherm data.

The isosteric heats of adsorption (Q_{st}) values were calculated (Figure 62) at zero coverage by calculating Henry's constants and using the Van't Hoff equation from the CO₂ and CH₄ isotherms at 273K and 298K. The Q_{st} values for CO₂ and CH₄ are 20.6 kJ mol⁻¹ and 15.7 kJ mol⁻¹, slightly higher than for other reported imine linked polymers and COFs. The reversible adsorption/desorption behavior and moderate Q_{st} values of CuPor-BPDC indicate that CO₂ and CH₄ interactions with the pore walls are weak enough to allow for material regeneration without applying heat. The relatively lower adsorption of CH₄ relative to the value obtained for H₂ may be size related.

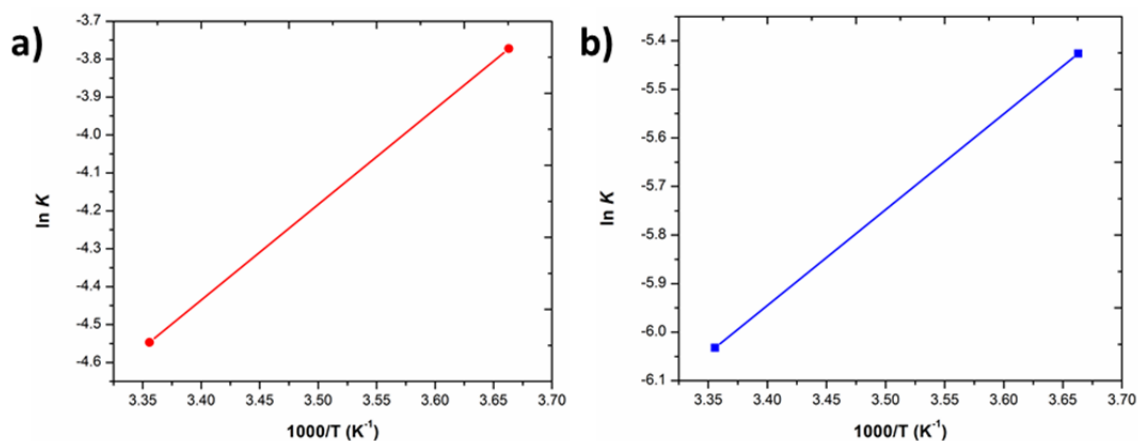


Figure 58. Van't Hoff plots of CO₂ (red) and CH₄ (blue).

3.1.4 Diffuse reflectance UV-Vis measurements of CuPor-BPDC

The solid-state UV-vis diffuse reflectance spectra of CuPor-BPDC provides an insight of the molecular organization of the porphyrin chromophores in the CuPor-BPDC polymer network which is evident from the slightly faded purple color of the polymer samples. The UV-Vis diffuse reflectance spectra (Figure 63) of CuPor-BPDC showed broad peaks from 200 to 800 nm with maxima at 410 nm, whereas two separated bands with maxima at 474 and 560 nm were observed.

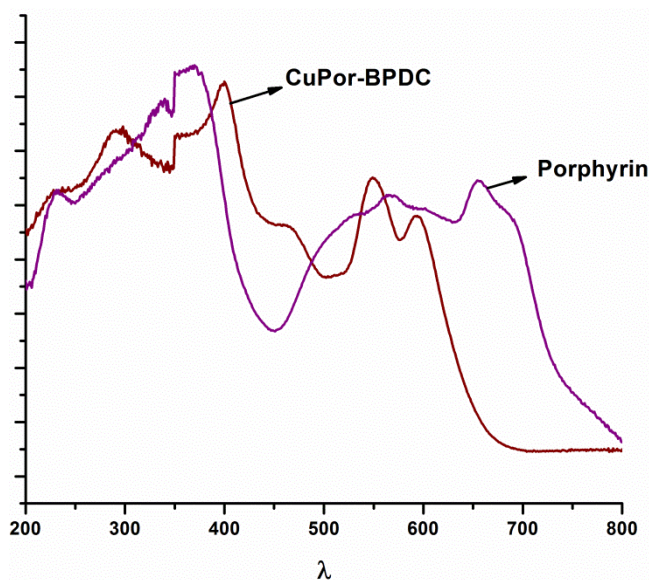


Figure 59: Solid-state absorption spectra CuPor-BPDC (wine), CuPor (purple) as powders using a praying mantis diffuse reflectance accessory. Small, jagged peaks around 340nm are due to instrument lamp shift.

3.1.5 Solid state NMR measurements of CuPor-BPDC

The solid-state ^{13}C cross polarization, magic angle spinning (CP-MAS) NMR spectra (Figure 64) further support the formation of the imine bond formation between **3** and **4** and the incorporation of these monomers into the framework of CuPor-BPDC. The solid-state ^{13}C CP-MAS NMR spectrum of the CuPor-BPDC showed a new C=N bond characteristic signal at $\delta = 158.41$ which was not present in the solid-state NMR spectrum of the tetrakis (*p*-tetraphenylamino) porphyrin Cu (II). Other peaks at $\delta = 173.56, 137.51, 128.66, 105.85$ ppm, were assigned to the carbon atoms of the CuPor-BPDC by comparison with the spectrum of the porphyrin (Figure 65). The ^{13}C CP-MAS spectra of the CuPor-BPDC and meso-tetraphenylamino porphyrin copper display similar chemical shifts to those of other reported COFs and starting materials.

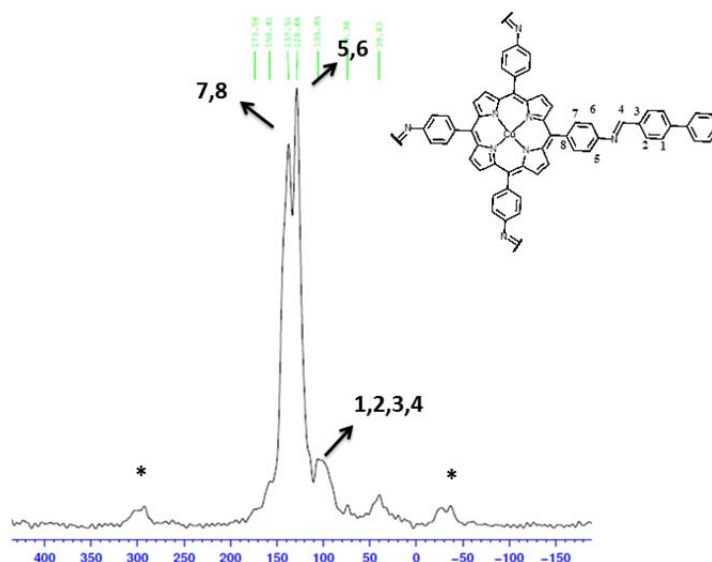


Figure 60. Solid state ^{13}C CP-MAS NMR spectrum of CuPor-BPDC recorded at a MAS rate of 10 kHz. Signals with * are residual solvent and side bands.

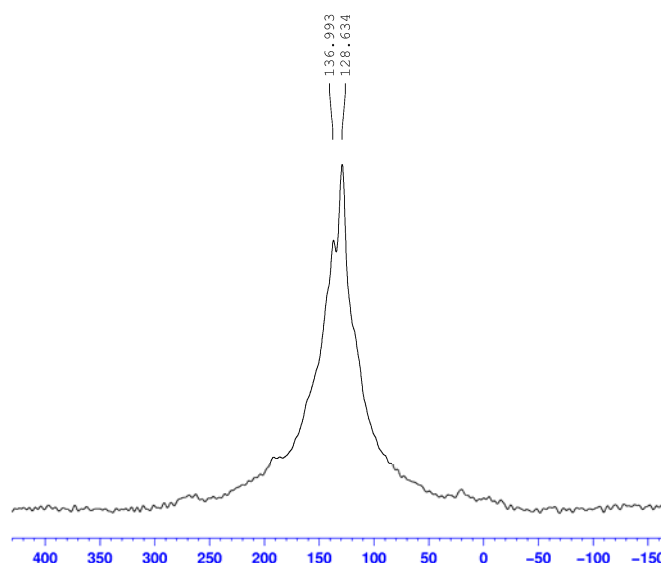


Figure 61. Solid state ^{13}C CP-MAS NMR spectra of meso-tetraphenylamino porphyrin recorded at a MAS rate of 10 kHz.

3.1.6 *Scanning electron microscopy images of CuPor-BPDC*

The porous morphology of CuPor-BPDC was also observed by scanning electron microscopy (SEM). The SEM image revealed randomly aggregated particles and a flake-like morphology of the purple CuPor-BPDC powder (Figure 66).

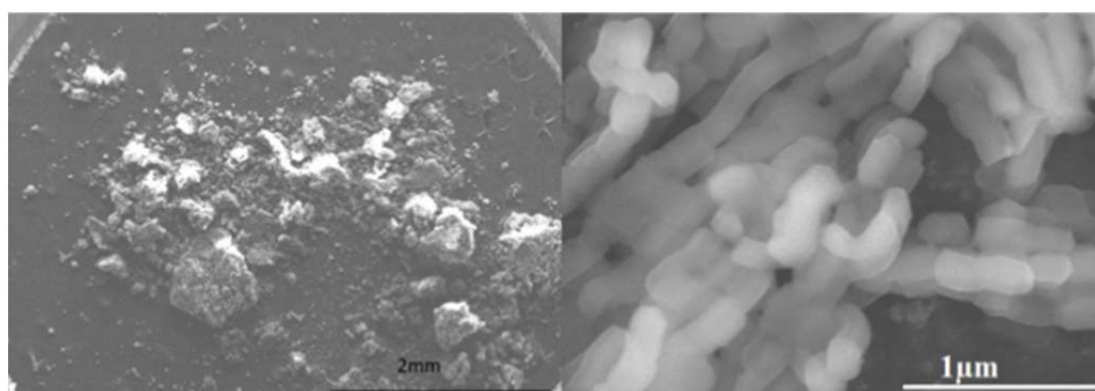


Figure 62. Scanning electron microscope image of the CuPor-BPDC.

3.1.7 Thermogravimetric analysis of CuPor-BPDC

To measure the thermal stability of CuPor-BPDC, the as-synthesized sample was subjected to thermogravimetric analysis under a flow of nitrogen (Figure 67). The TGA trace is similar to those of other reported imine linked porous organic polymers and COFs, retaining 80% of the mass at 300°C.

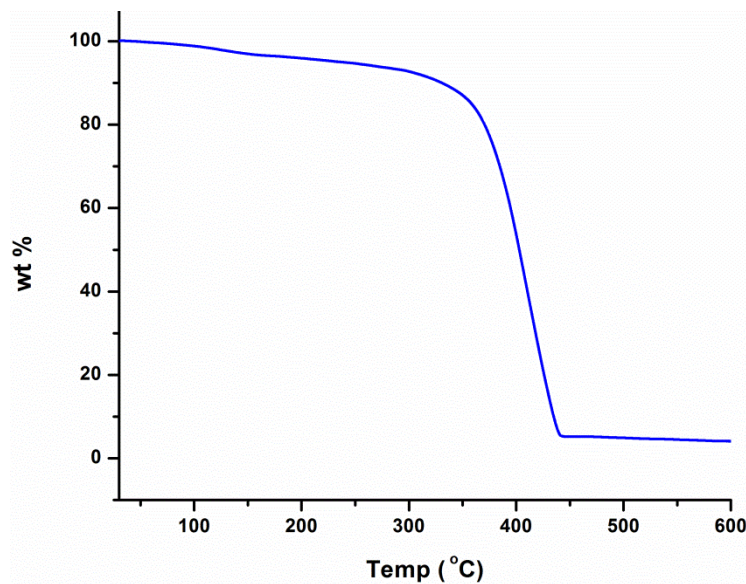


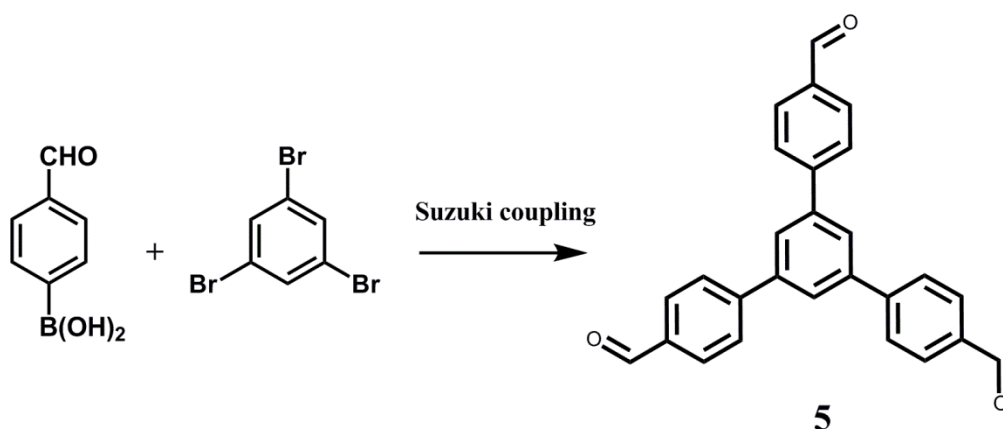
Figure 63. TGA of CuPor-BPDC obtained up to 600°C using a linear 3°C/min ramp method.

3.2 Synthesis and characterization of precursors of IBTP

Synthesis of 1,3,5 tris (4-formylphenyl) benzene (5):

Tribromobenzene (5.0 g, 15.9 mmol), 4-formylphenyl boronic acid (14.3 g, 95.3 mmol), potassium carbonate (13.2 g, 95.3 mmol), and palladium tetrakis (triphenyl phosphine) (0.92 g, 0.794 mmol) were added to a 300 mL round bottom flask equipped with a stir bar and condenser. The flask was evacuated and backfilled with N₂ three times. Dioxane (133 mL) and H₂O (27 mL) were mixed and then added to the flask. The resulting suspension was subjected to three freeze pump-thaw cycles. The reaction mixture was then heated to reflux for 48 h. The reaction mixture was cooled to r.t, after which a precipitate formed that was washed with ethyl acetate and collected. This solid was saved and later

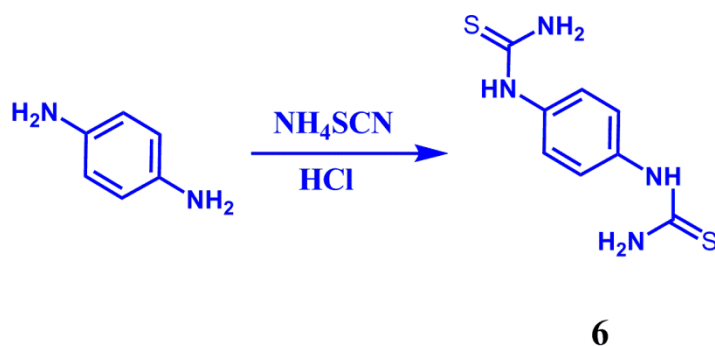
identified as pure **2**. The supernatant was washed with H₂O, then brine, finally dried with MgSO₄, filtered, and the solvent was removed. The crude product isolated from the supernatant was then dissolved in DCM and run through a plug of SiO₂. The solvent was next evaporated and the resulting solid was recrystallized from MeCN. These isolated white solids were combined to yield **2** (3.83 g, 62%). ¹H NMR (600 MHz, 298K, CDCl₃): δ 10.15 (s, 3H), 8–8.1 (dd, 6H), 7.89 (3H, s), 7.81–7.89 (dd, 6H).



Scheme 6. Synthesis of 1,3,5 tris (4-formylphenyl) benzene from 4-formylphenyl boronic acid and 1,3,5 tribromobenzene.

Synthesis of p-Phenylene bis-thiourea (6):

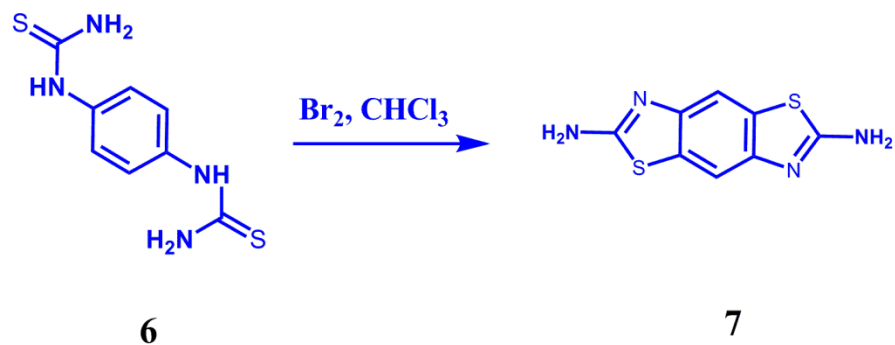
To a 250ml flask were added 8.5 g (1.57 mol) of *p*-phenylenediamine, 70 mL of deaerated water, 150 mL of concentrated hydrochloric acid, and 0.5g of activated charcoal. The mixture warmed to 50°C and transferred with filtration into another 250ml flask. Ammonium thiocyanate (2.4 g) was added and the mixture was stirred at a pot temperature of 90-100°C for 20-24 h. The yellow, granular product began to precipitate after 2 h of reaction. The mixture was allowed to cool, and the product was collected by filtration. The product was washed with 800mL of hot water and then dried at 100°C under reduced pressure. The yield was 17 g (95.6%) of a light yellow, granular solid of purity suitable for the next step.



Scheme 7. Synthesis of *p*-Phenylene bis-thiourea from *p*-phenylenediamine.

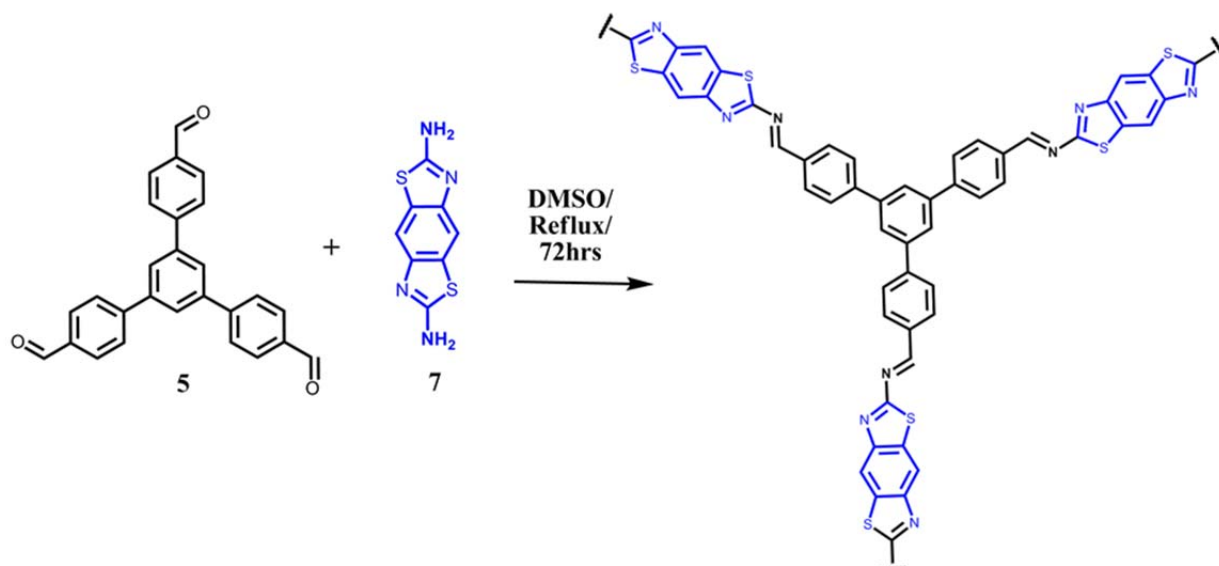
Synthesis of 2,6-Diaminobenzobisthiazole (7):

To a stirred suspension of 3g (0.13mol) of 7 in 140 mL of dry chloroform was added a solution of 4.9 g (0.3mol of Br₂) of bromine in 20mL of chloroform such that the pot temperature did not rise above 50°C. The orange slurry was stirred at room temperature overnight and then heated at reflux for 24 h. The mixture was allowed to cool under a slow stream of argon. The granular orange solid was then collected by filtration. The crude product was washed with 60 mL of chloroform, dried in air, and stirred with aqueous sodium bisulfite (20 g of NaHSO₃/150L of water). The yellow solid was collected by filtration, washed with 50 mL of concentrated ammonium hydroxide, and then washed with 100 mL of water. The crude was recrystallized twice from 140 mL of glacial acetic acid. After drying to constant weight at 85°C under reduced pressure, 1.6 g (54.3%) of 6 was obtained as feathery needles. ¹H NMR (600 MHz, 298K, DMSO-*d*₈): δ 7.25 (br, 4H), 7.57 (s, 2H).



Scheme 8. Synthesis of 2,6-Diaminobenzobisthiazole from *p*-Phenylene bis-thiourea.

Synthesis of IBTP: 5ml of DMSO was added to the mixture of 1,3,5 tris (4-formylphenyl)-benzene (0.2 mmol, 78 mg) and 2,6-diaminobenzo bisthiazole (66 mg, 0.3 mmol) and then refluxed the yellow color homogeneous mixture for 3 days. The dark brown precipitate was filtered and washed with DMSO, dichloromethane, acetone and tetrahydrofuran. The brown powder was dried at 120°C under vacuum overnight to give the corresponding polymer in 72% yield. Elemental analysis (%) calcd. for IBTP, theory: C, 67.8; H, 2.65; N, 11.40; found C, 69.57; H, 2.43; N, 12.86, respectively.



Scheme 9. Synthesis of IBTP from 1,3,5 tris (4-formylphenyl)-benzene and 2,6-diaminobenzo bithiazole.

3.2.1 Powder X-ray diffraction and simulation of IBTP

Powder X-ray diffraction (Cu K α radiation) did not exhibit any intense diffraction peaks, as commonly observed for amorphous porous organic polymers (Figure 68).

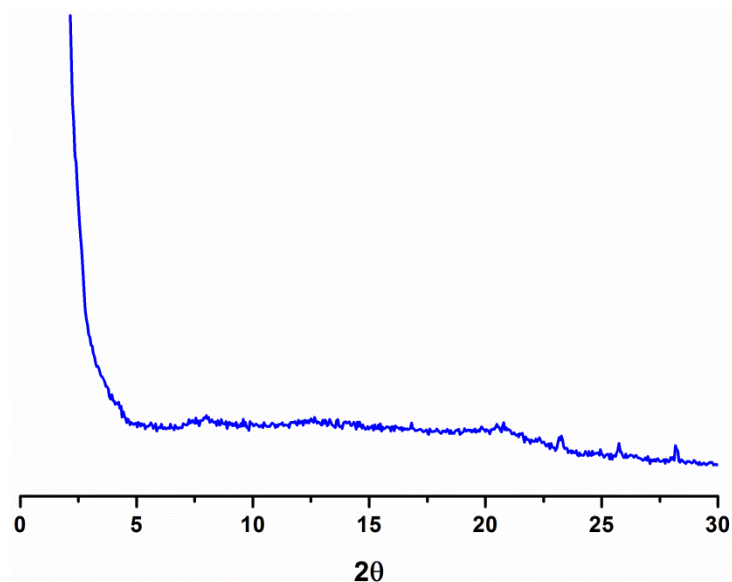


Figure 64. Powder X-ray diffraction pattern of IBTP. No intensive diffraction peaks were observable.

3.2.2 *FT-IR measurements of IBTP*

The FT-IR spectrum of IBTP showed highly attenuated -N-H and -C=O stretching frequencies from the 1,3,5 tris (4-formylphenyl)-benzene and 2,6-diaminobenzo bisthiazole at 3400cm^{-1} , 3280cm^{-1} and 1740 cm^{-1} (Figures 69 and 70). The formation of imine bonds between **1** and **2** were confirmed by FT-IR which exhibited a new characteristic -C=N stretching frequency at 1690 cm^{-1} (Figures 69 and 70).

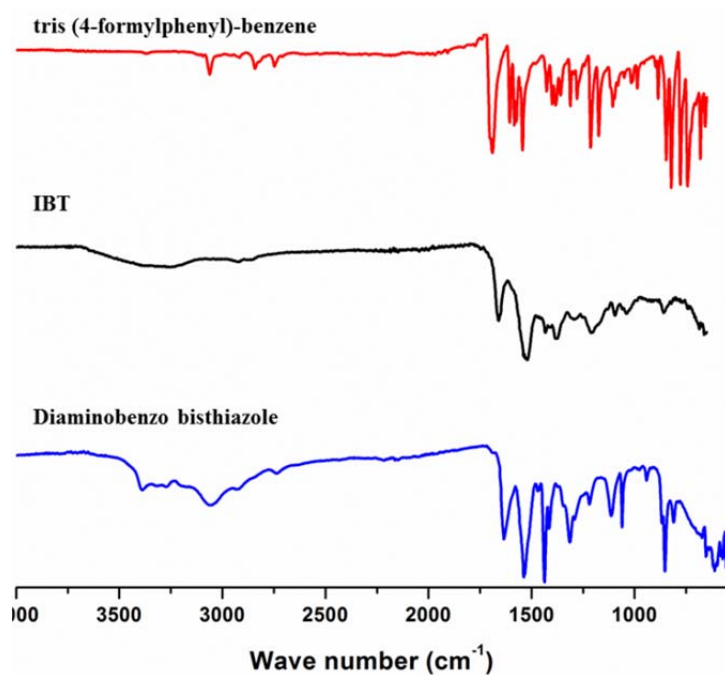


Figure 65. IR spectra of 1,3,5 tris (4-formylphenyl)-benzene and 2,6-diaminobenzo bisthiazole and IBTP.

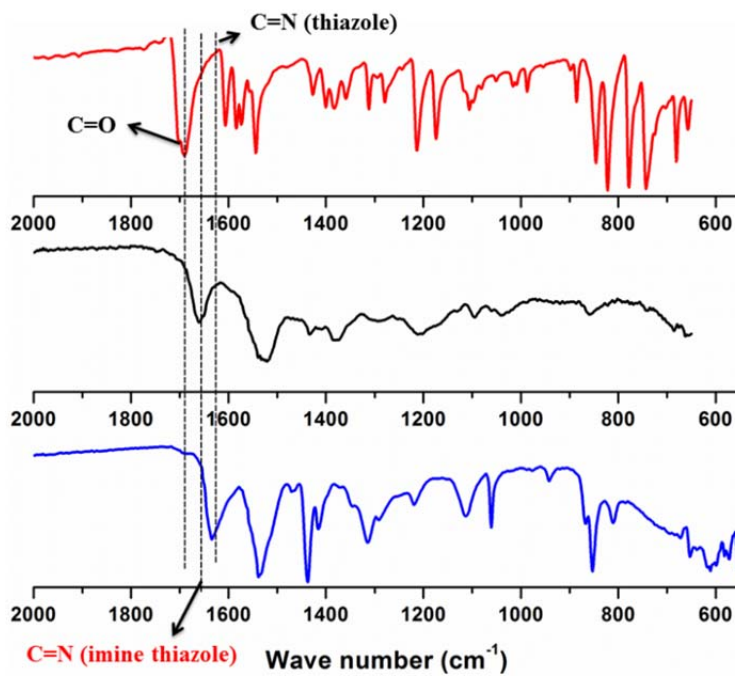


Figure 66. Expanded IR spectra of 1,3,5 tris (4-formylphenyl)-benzene and 2,6-diaminobenzo bisthiazole and IBTP.

3.2.3 Gas adsorption measurements of IBTP

N₂ gas adsorption/desorption measurements of degassed IBTP confirmed its microporosity at 77K (Figure 71). The apparent Brunauer–Emmett–Teller (BET) surface area was 328 m² g⁻¹ and a surface area of 1705 m² g⁻¹ was obtained by applying the Langmuir model. The steady N₂ uptake at low pressure (0–0.1bar) and the gradual increase at higher pressures (0.1–1bar) result in a type I isotherm (Figure 71a), which is typical for microporous frameworks that show permanent microporosity. This surface area is lower than others reported for imine linked polymers. Pore size distribution curves were analyzed by fitting the uptake of the N₂ isotherm using the nonlocal density functional theory (NLDFT) method, and were found to be around 15 Å (Figure 72) and the pore volume was calculated to be 0.81cm³ g⁻¹. Hysteresis was observed with the desorption low lying above the adsorption, which could be due to the presence of micropores and diffusion of gas through micropores to mesopores that are also present in the framework and vice versa. To find the possible impact of the microporosity and nitrogen rich pore walls of IBTP, we measured CO₂, CH₄, N₂ and H₂ adsorption capacities and selectivity and calculated their respective isosteric enthalpies (Q_{st}). All CO₂, CH₄ and N₂ isotherms were measured at 273 and 298 K from 0–1 bar (Figures 71c-d). Both CO₂ and CH₄ isotherms are reversible and exhibit a steep rise at P = 0–1bar, the CO₂ capture capacity of IBTP was 7.8 wt% at 273K and 5wt% at 298K, respectively. The Q_{st} value for CO₂ was estimated from data collected under these conditions using the Van't Hoff equation. At zero coverage, the Q_{st} is 37.4 kJ mol⁻¹ (Figure 73). The CO₂ uptake and Q_{st} are higher than the corresponding value for most COFs and for imine POPs and comparable to ZIFs containing nitrogen functionalized pores. The relatively high binding capacity of IBTP for CO₂ is likely due to favorable interactions between CO₂ molecules and the nitrogen rich imine and benzothiazole units in the

framework. The reversible adsorption-desorption behavior indicates that CO₂ interactions with pore walls are weak enough to allow for IBTP regeneration without applying heat. Usually materials that have strong basic sites display high CO₂ affinities and require energy input in the form of heat to regenerate their active sites as in the case of commercial amine solutions. In addition to CO₂ adsorption, we have evaluated the adsorption properties of N₂, H₂ and CH₄ on IBTP at low pressures and different temperatures due to their potential use in automobile applications.

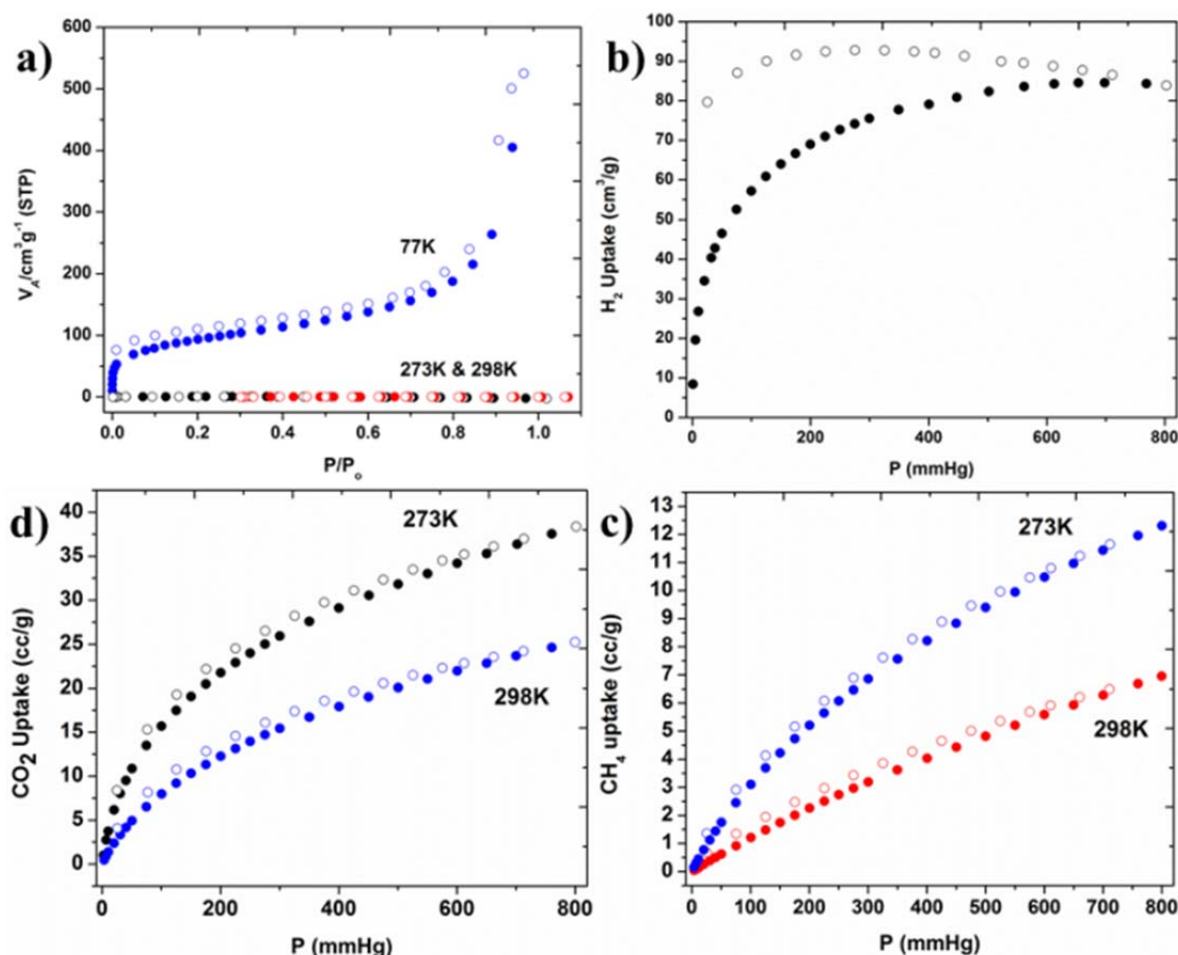


Figure 67. (a) Nitrogen at 77K (b) Hydrogen at 77K (c) CO₂ at 273K and 298K (d) CH₄ at 273K and 298K adsorption (filled symbols) and desorption (empty symbols) isotherm curves.

The H₂ uptake of IBTP shown in Figure 71b, exhibited a reversible profile and pronounced hysteresis that we believe is due to the sulfur-hydrogen interactions. At 77K, 1bar, IBTP exhibited an uptake of 0.78 wt % which is comparable to other crystalline 2D COFs such as COF-10 (0.8 wt% at 77K

and 1bar). Similarly, we measured CH₄ and N₂ storage properties on the IBTP polymer at both 273K and 298K, which revealed an uptake of 0.9 and 0.5 wt% for CH₄ at 273K and 298 K/1bar and almost zero for N₂ at 273K and 298 K/1bar (Fig. 71d). Once again, both isotherms are reversible and exhibit a steep rise at low pressure for CH₄ and then reach maxima at 1bar, 273 and 298 K, respectively. The Q_{st} for CH₄ was calculated using adsorption data collected at 273 and 298 K. At zero coverage, the Q_{st} for CH₄ is 20.7 kJ mol⁻¹ which is higher than for most COFs and POPs (Figure 73). A higher Q_{st} value for CO₂ compared to that of CH₄ is likely due to the polar nature of CO₂. Furthermore, the selectivity of IBTP towards CO₂ over N₂/CH₄ was investigated by collecting isotherms at 273 and 298 K (Figure 71c). At 273 K and 1 bar, the CO₂ uptake is 7.8wt% whereas that of CH₄ is only 0.9wt%. On the basis of Henry's constant calculations in the pressure range of 0 to 1 bar, the estimated adsorption selectivity for CO₂/N₂ is 51 and for CO₂/CH₄ it is 6.3 at 273K/298K/1bar, and we believe this value will be higher at 0.15bar which is the pressure of flue gas. These values exceed those reported for other COFs and POPs.

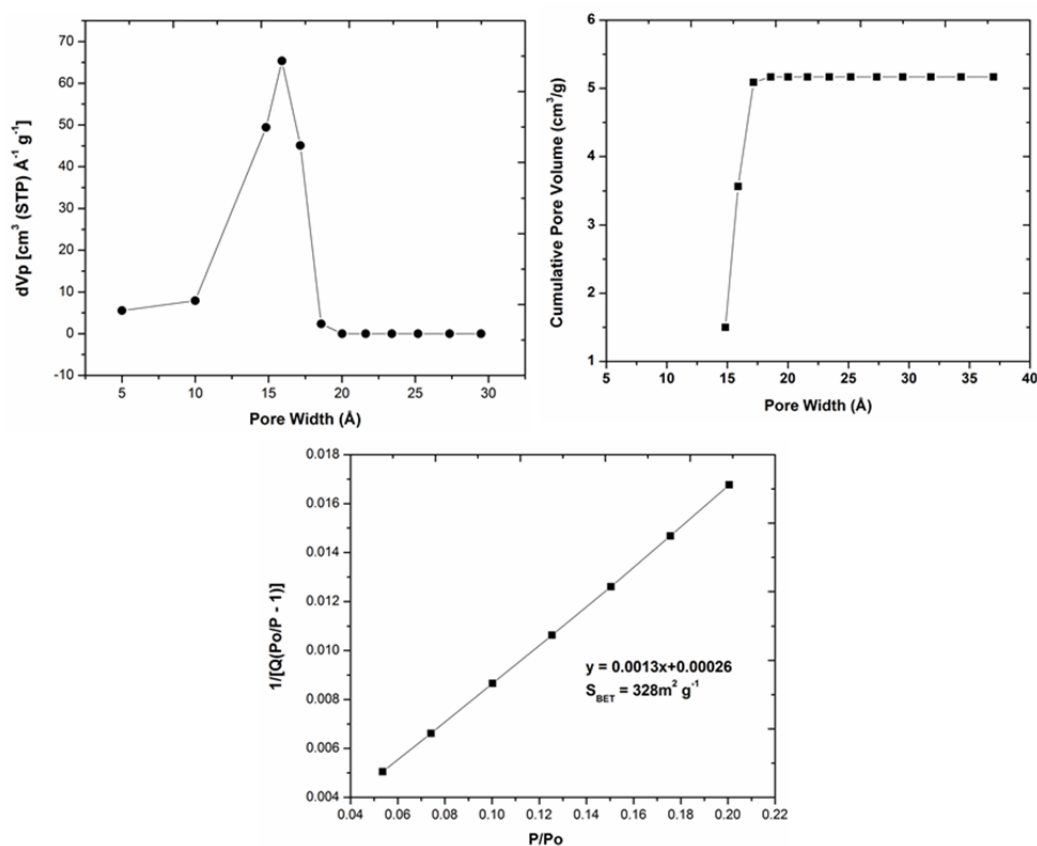


Figure 68. Differential (top left) and cumulative (top right) pore size distribution plot of IBTP from the application of the NLDFT model to the N₂ isotherm. BET plot (below) for IBTP calculated from isotherm data.

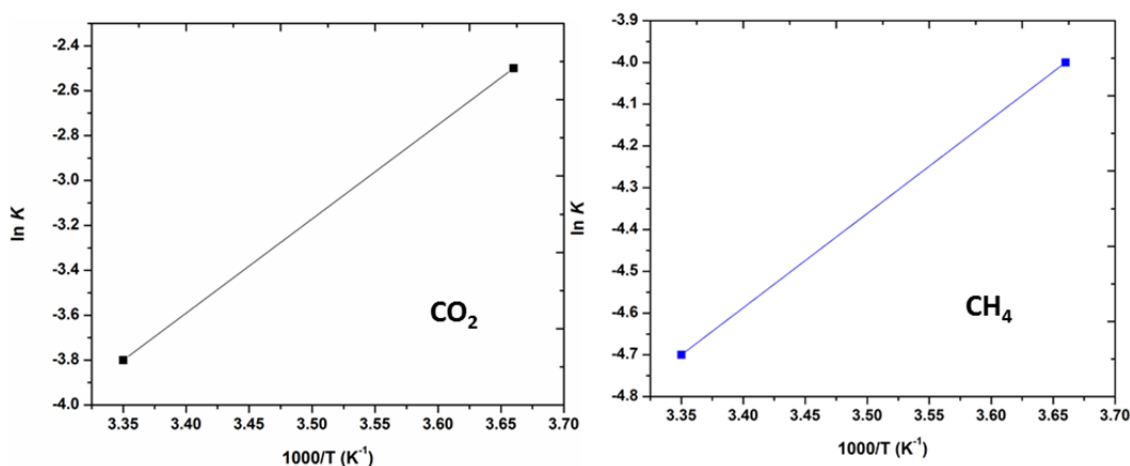


Figure 69. Van't Hoff plots of CO₂ (red) and CH₄ (blue).

3.2.4 Diffuse reflectance UV-Vis measurements of IBTP

We also measured the absorption spectra of IBTP and diaminobenzo bisthiazole monomer to find the absorption ability of benzothiazole units in the UV-Vis region. The molecular organization of these benzothiazole chromophores in the porous polymer was evident from new absorption peaks at 595 and 640nm, with the spectrum of monomer 2,6-diaminobenzo bisthiazole, while peaks at 230 and 290nm (Figure 74) were conserved. This proves the presence of benzothiazole chromophores in the IBTP polymer which is further evident from the color change of the polymer sample to dark brown whereas the monomers are white and yellow.

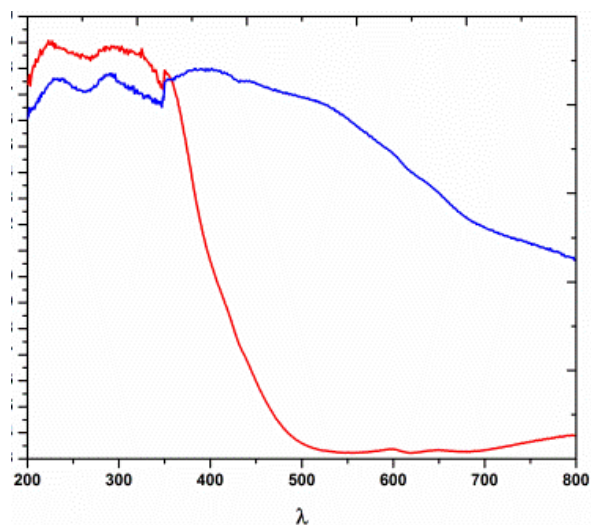


Figure 70: Solid-state UV absorption spectra IBTP (red), 2,6-diaminobenzo bisthiazole (blue) as powders using a praying mantis diffuse reflectance accessory.

3.2.5 Solid state NMR measurements of IBTP

Solid-state ^{13}C CP-MAS NMR measurements support the presence of benzothiazole and 1,3,5 tris (4-formylphenyl)-benzene monomers in the framework. The IBTP polymer exhibited peaks at 169 and 156 ppm which correspond to the $\text{C}=\text{N}$ ($-\text{C}=\text{N}$) carbons in the benzothiazole and imine units (Figure 75), respectively. In addition, the NMR spectrum also showed multiple peaks between 104 and 139 ppm which can be assigned to other aromatic carbon atoms from both building blocks.

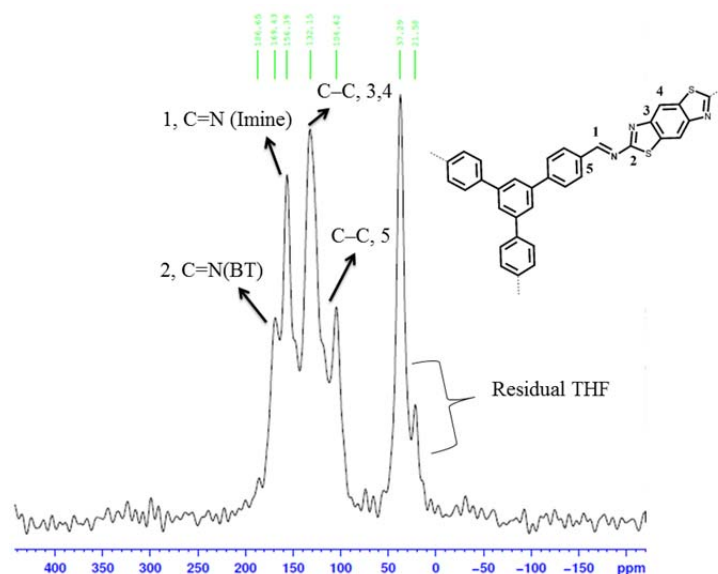


Figure 71. Solid state ^{13}C CP-MAS NMR spectrum of IBTP recorded at a MAS rate of 10 kHz.

3.2.6 Scanning electron microscopy images of IBTP

Visualization of these imine and benzothiazole based networks using scanning electron microscopy (SEM) showed randomly aggregated particles of IBTP powder, which did not provide any further insight into the porous nature of the framework (Figure 76).

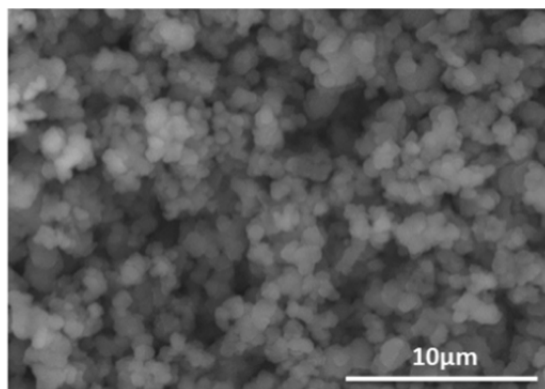


Figure 72. Scanning electron microscope image of the IBTP.

3.2.7 Thermogravimetric analysis of IBTP

To measure the thermal stability, IBTP samples were subjected to thermogravimetric analysis under a flow of N₂ (Figure 77). The TGA trace is typical of the other reported POPs, retaining 80% of the mass at 450°C.

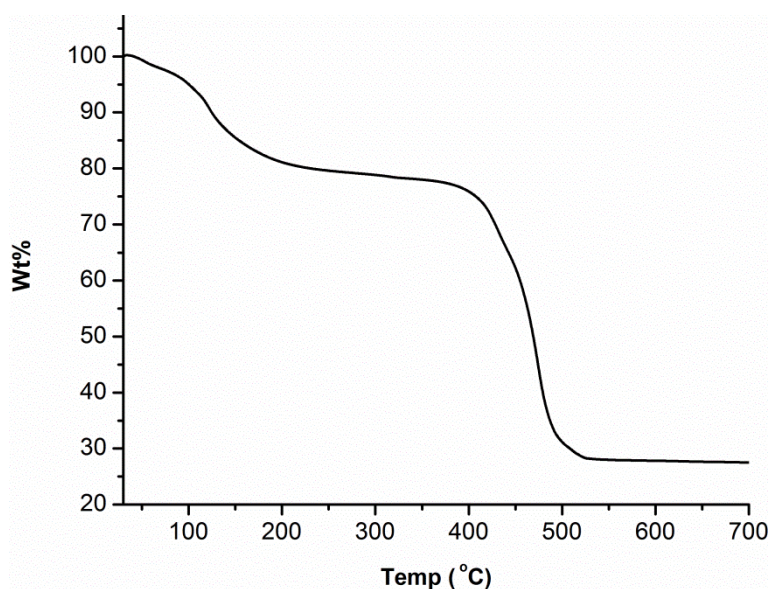


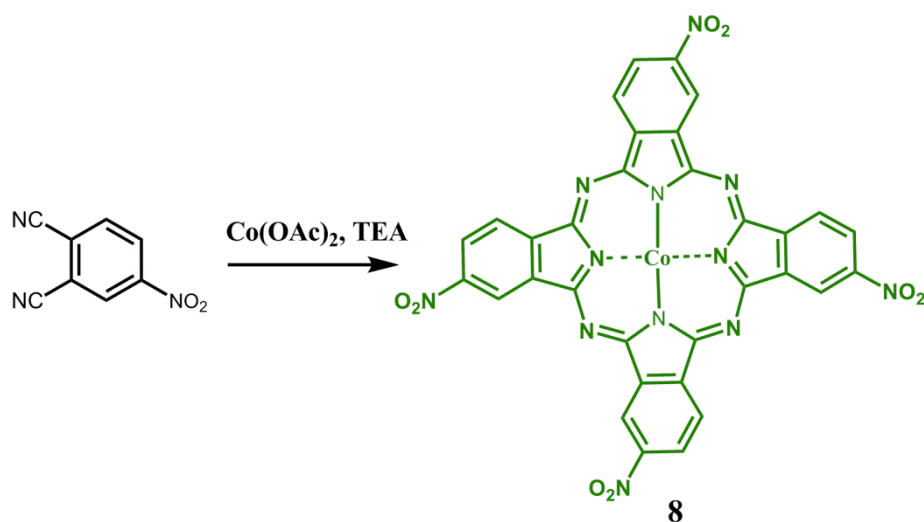
Figure 73. TGA of IBTP obtained up to 700°C using a linear 3°C/min ramp method.

3.3 Synthesis and characterization of precursors of Pc-POP

Synthesis of 2,9,16,23 tetranitro Co(II) phthalocyanine (8):

A finely ground mixture of 4-nitrophthalic acid (10.0 g, 0.09 mol), CoSO₄ · 7H₂O (7.5 g, 0.03 mol), ammonium chloride (5.0 g, 0.09 mol), urea (30.0 g, 0.49 mol) and a catalytic amount of ammonium molybdate was stirred in a 500-mL round-bottomed flask containing nitrobenzene solvent (15 mL) at 180 °C for 5 h. The resulting crude product was ground and washed with methanol repeatedly until the

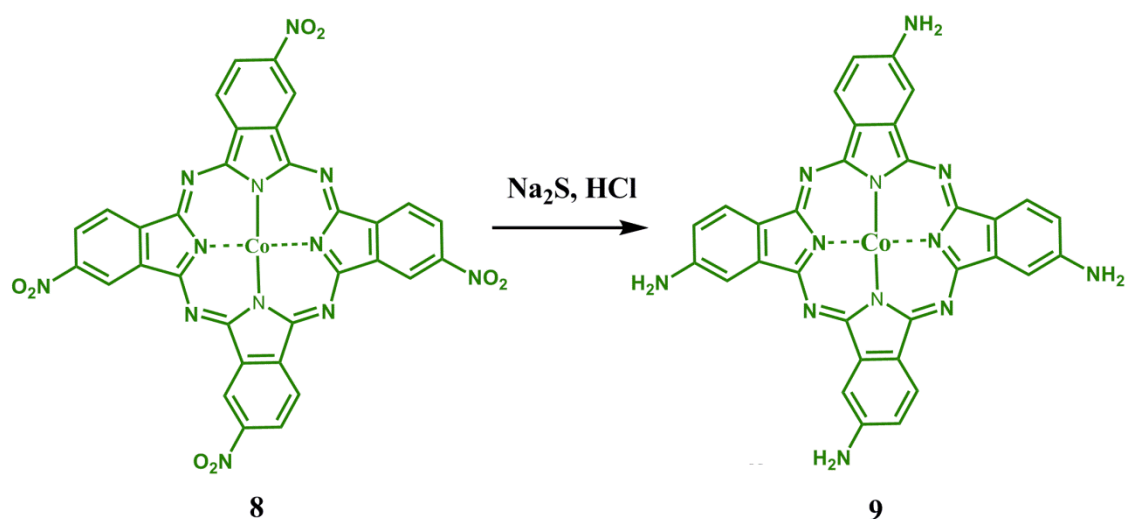
solvent was completely removed. It was further stirred in 1 M HCl (500 mL) saturated with NaCl for 5 min and filtered. The residue was then washed using 1 M NaOH (500 mL) saturated with NaCl at 90 °C until the evolution of NH₃ ceased. The resulting product was centrifuged and further treated with NaCl-saturated HCl and NaOH solutions a few times. The bluish-green product, 2,9,16,23-tetranitro cobalt (II) phthalocyanine (**8**) was washed with water until free from chloride ions, centrifuged and dried in vacuum.



Scheme 9. Synthesis of tetranitro Co(II) phthalocyanine from nitrophthalonitrile.

Synthesis of 2,9,16,23 tetraamino Co(II) phthalocyanine (9):

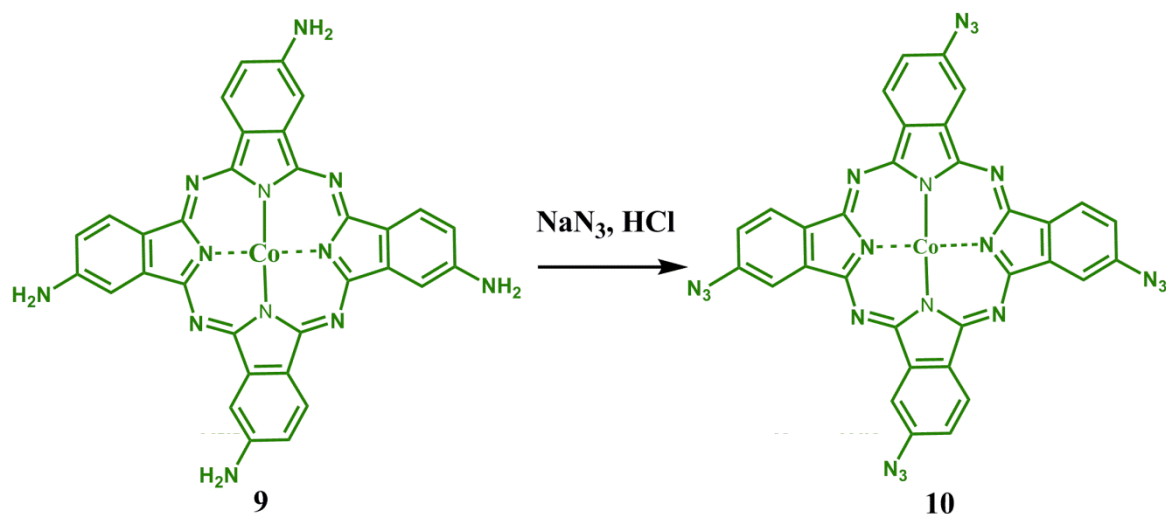
The reduction of the nitro groups was carried out by stirring 2,9,16,23-tetranitro cobalt (II) phthalocyanine (**8**, 10.0 g, 0.01 mol) in an aqueous solution (250 mL) of sodium sulfide nonahydrate (50.0 g, 0.21 mol) at 50°C for 5 h. The solid product was separated in a centrifuge and treated with 1 M HCl (500 mL). The residue was separated and treated with 1 M NaOH (500 mL), stirred for 1 h, and centrifuged to separate the solid complex. The product was repeatedly washed with water until free from NaOH and NaCl. The pure 2,9,16,23-tetraamino cobalt(II) phthalocyanine (**9**) was dried in vacuum.



Scheme 10. Synthesis of tetraamino Co(II) phthalocyanine from tetraamino Co(II) phthalocyanine.

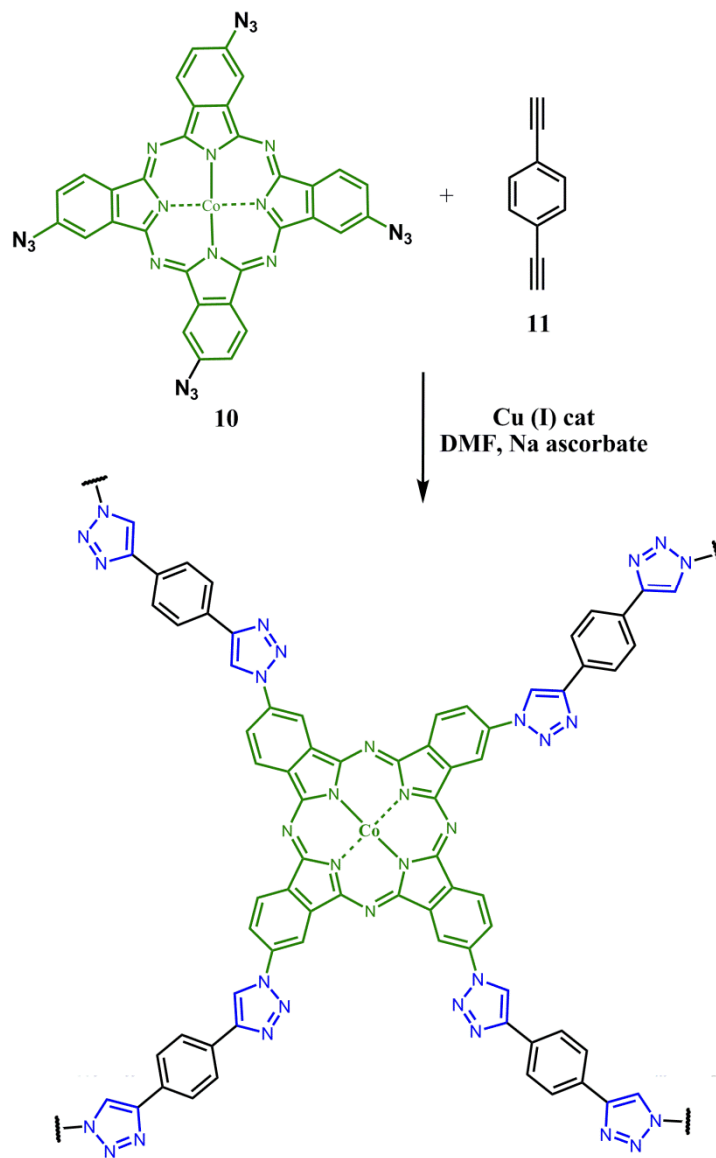
Synthesis of tetraazidophthalocyanine Co(II) (10):

Tetraamino Co(II) phthalocyanine (**9**, 2 g, 5.2 mmol) was dissolved in 2 N aqueous HCl (100 mL) in a 1-L roundbottom flask and cooled down to 0°C . A solution of NaNO_2 (1.6g, 23.3 mmol) in H_2O (10 mL) was then added drop-wise into the cooled reaction flask with vigorous stirring. The reaction mixture was kept at 0°C for 30 minutes before being neutralized with CaCO_3 . To this mixture was then added a solution of NaN_3 (1.8g, 27.7 mmol) in H_2O (10 mL) at 0°C . The resulting mixture was allowed to stir at 0°C for an additional 20 min and then filtered. The collected green solid was washed with excess H_2O and dried under dynamic vacuum to afford **10** as a green solid (2 g, 79% yield).



Scheme 11. Synthesis of tetraazido Co(II) phthalocyanine from tetraamino Co(II) phthalocyanine

Synthesis of phthalocyanine polytriazole porous organic polymer



Scheme 12. Synthesis of CoPc-BPDA COF from 4,4'-biphenylboronic acid and (OH)₈Pc Co(II).

Tetraazidophthalocyanine Co(II) (**10**, 48.5 mg, 0.1 mmol) and DMF (10 mL, to make a 0.04 M solution of azide functional group, at 1:1 alkyne to azide functional group ratio) were added into a 50-mL flask equipped with a magnetic stir bar and a water-cooled reflux condenser. Then CuSO₄·5H₂O (10 mg, 0.04

mmol, 0.1 equivalent per acetylene functional group), sodium ascorbate (10 mol%) and 1,4-diethynylbenzene (**11**, 41.6 mg, 0.1 mmol) were added subsequently. The reaction mixture was then heated to 100°C for 24 h before being stopped. A green precipitate was observed after 15-30 min for the reaction at 100°C.

3.3.1 Powder X-ray diffraction and simulation of Pc-POP

Both CoPc-N₃ and Pc-POP were amorphous powders as evidenced by their powder X-ray diffraction (PXRD) (Figure 78).

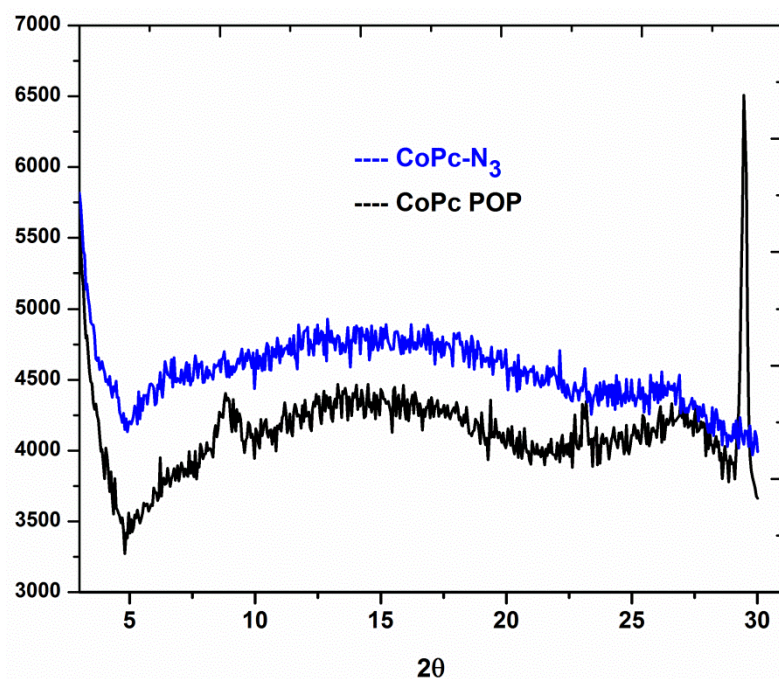


Figure 74. Powder X-ray diffraction pattern of CoPc-POP and CoPc-N₃. No intensive diffraction peaks were observable.

3.3.2 FT-IR measurements of Pc-POP

Fourier transform infrared spectroscopy (FT-IR) shows significant depletion of the stretching frequencies of azide functional groups at 3257 cm⁻¹ for CoPc-N₃ and acetylene functional groups at

3396cm^{-1} which correspond to C-H protons of the acetylene triple bond on diethynylbenzene. Both CoPc-N₃ and Pc-POP exhibited strong stretching frequencies at 1030 cm^{-1} which is a characteristic of the N-Co vibration band remaining unchanged in the corresponding polymers (Figures 79 and 80).

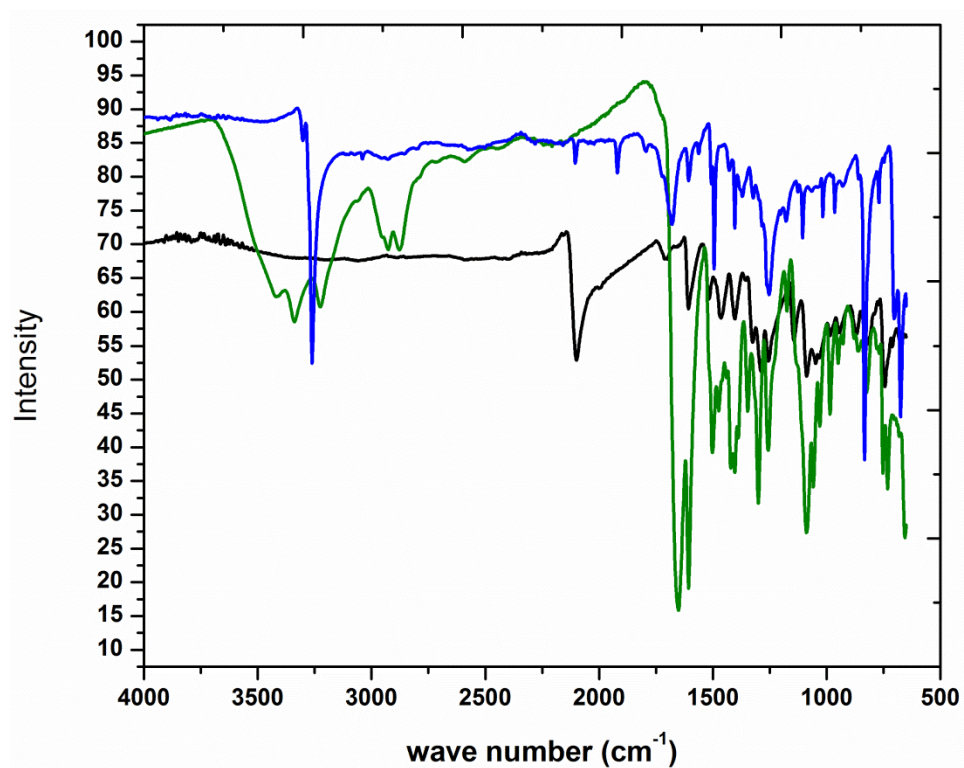


Figure 75. IR spectra of 1,4-diethynylbenzene (blue), CoPc-POP (black) and CoPc-N₃ (green).

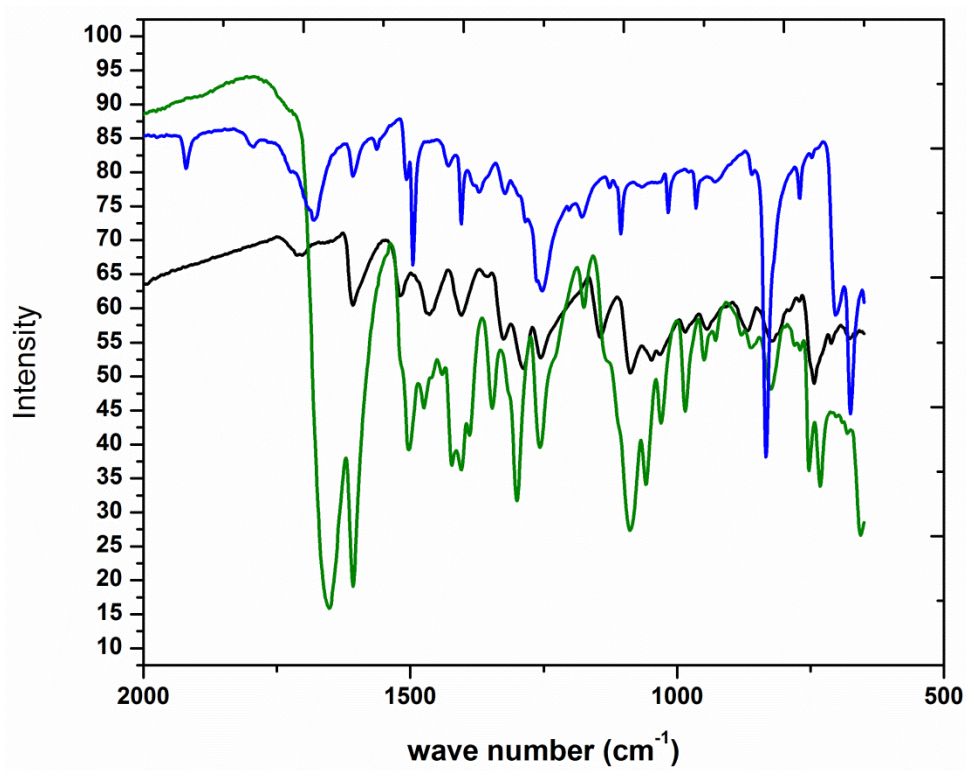


Figure 76. Expanded IR spectra of 1,4-diethynylbenzene (blue), CoPc-POP (black) and CoPc-N₃ (green).

3.3.3 Gas adsorption measurements of Pc-POP

The porosity parameters of the Pc-POP polymer were studied by gas adsorption analysis using N₂ at 77K and 273K on activated samples. Activation was done by exchanging guest molecules using THF followed by filtration and degassing at 100°C in a vacuum oven before gas adsorption analysis. The Brunauer–Emmett–Teller (BET) surface areas were found to be 115m²/g within the pressure range of $P/P_0 = 0 - 1$ (Figure 81). The N₂ adsorption-desorption of Pc-POP exhibited a type I isotherm indicating its microporous nature.

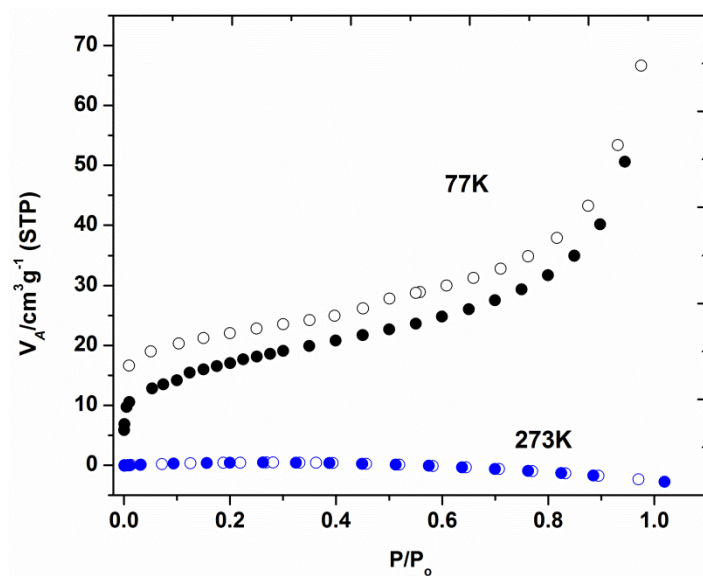


Figure 77. N₂ adsorption of Pc-POP at 77K and 273K. Adsorption (filled symbols) and desorption (empty symbols) isotherm curves.

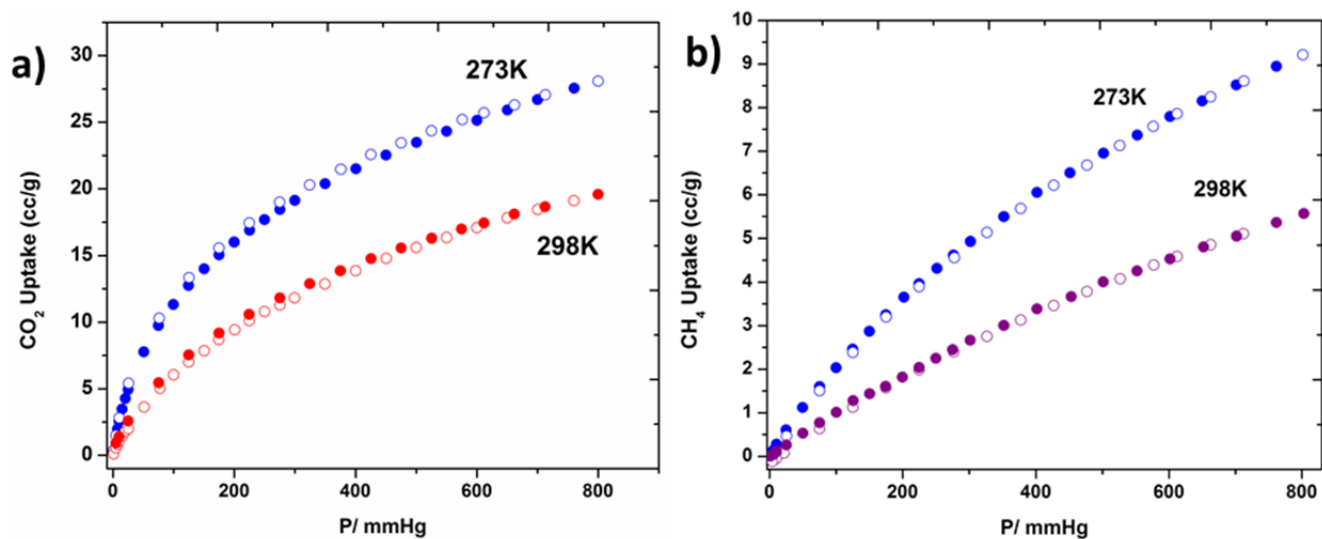


Figure 78. CO₂ and CH₄ adsorption at 273K and 298K. Adsorption (filled symbols) and desorption (empty symbols) isotherm curves.

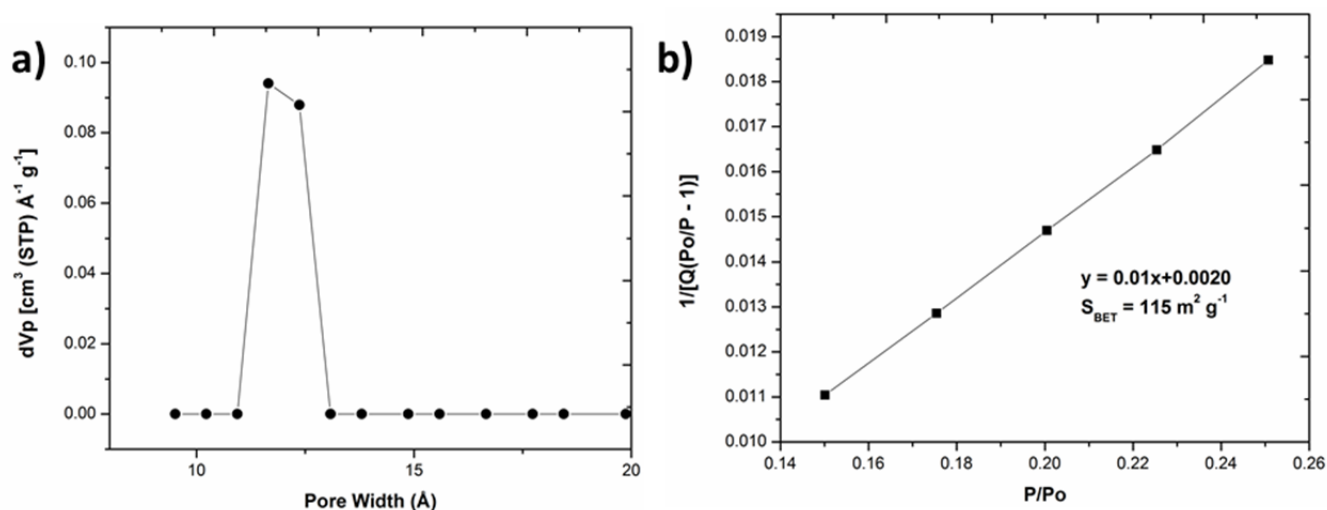


Figure 79. (a) Differential pore size distribution plot of Pc-POP from the application of the NLDFT model to the N₂ isotherm. (b) BET plot for Pc-POP calculated from isotherm data.

3.3.4 Solid state NMR measurements of Pc-POP

Pc-POP was characterized by ¹³CP/MAS NMR spectroscopy to confirm the chemical connectivity (Figure 85). There are six peaks observed at approximately 189.42, 166.83, 163.32, 148.02, 130.62 and 119.42 ppm for Pc-POP. The peak at 148.02 ppm corresponds to nonacetylenic-substituted phenyl carbons and the peak at 130.62 corresponds to the acetylene-substituted phenyl carbons and the low-intensity peak at approximately 119.42 ppm can be attributed to the acetylene carbons. The other peaks at 163.32, 166.83, and 189.42 ppm can be assigned to the carbon atoms of the phenyl groups.

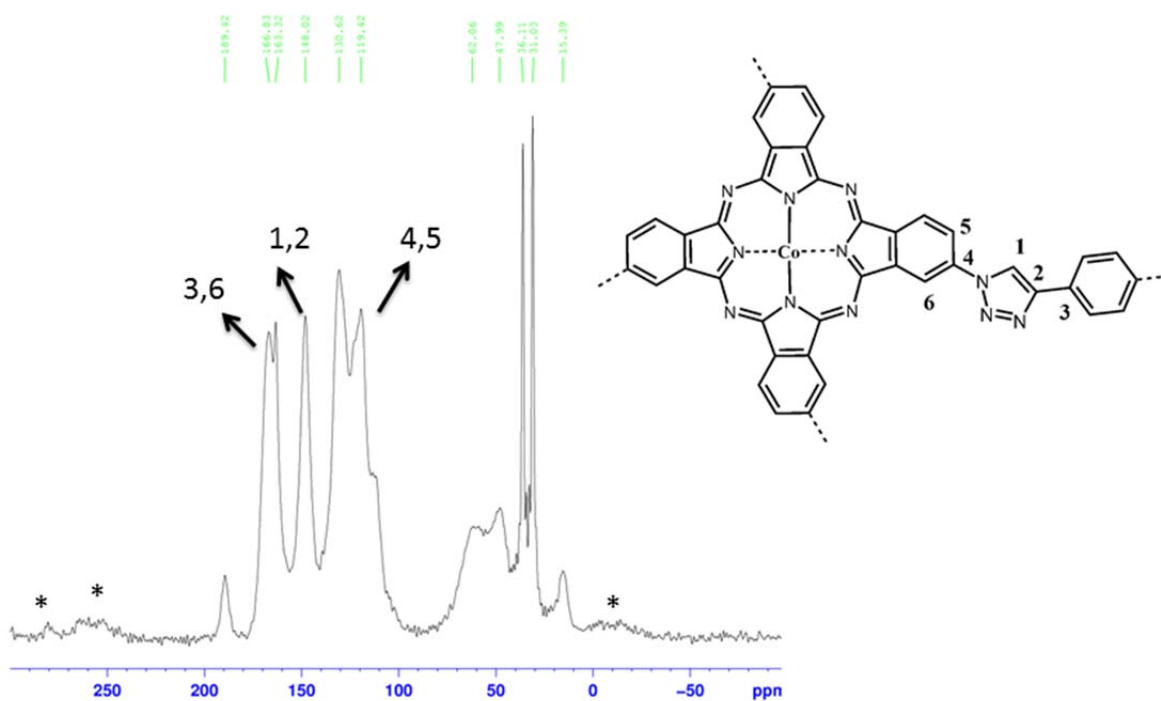


Figure 80. Solid state ^{13}C CP/MAS NMR spectrum of Pc-POP recorded at a MAS rate of 12.5 kHz. Signals with * are residual solvent and side bands.

3.3.5 Scanning electron microscopy images of Pc-POP

The morphology of Pc-POP investigated using SEM. From field-emission scanning electron microscopy (FE-SEM) images, Pc-POP contains flake-shaped monoliths with sizes of 500nm-2 μm , indicating phase purity (Figure 86).

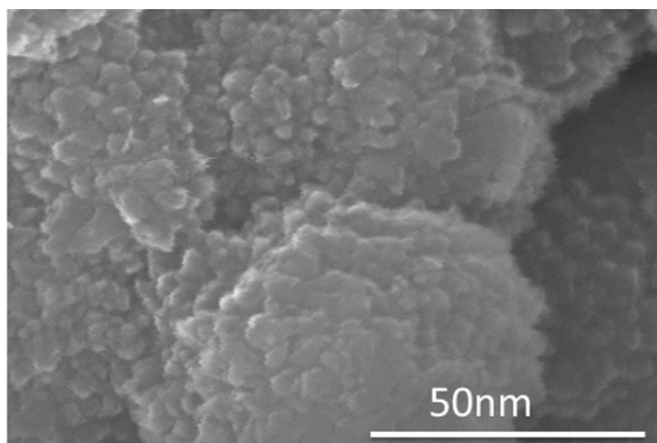


Figure 81. Scanning electron microscope image of the Pc-POP.

3.3.7 Thermogravimetric analysis of Pc-POP

To evaluate the thermal stability of the Pc-POP, thermogravimetric analysis was conducted under a flow of N₂ (Figure 87). TGA traces show that Pc-POP remain stable up to about 500°C. Pc-POP is highly stable due to extended conjugation and π - π stacking of the phthalocyanines within the framework and is comparable to previously published phthalocyanine polymers.

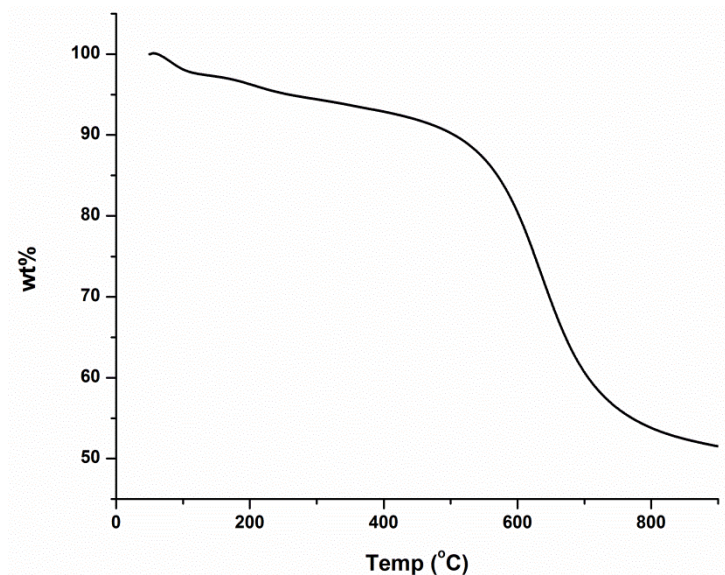


Figure 82. TGA of Pc-POP obtained up to 700°C using a linear 5°C/min ramp method.

3.4 H₂, CH₄, and CO₂ uptake properties of porous organic polymers at 273K/1bar.

POP	H ₂	CH ₄	CO ₂	PORE VOLUME
CuPor-BPDC	0.4 wt%	0.32 wt%	5.5 wt%	0.41cm ³ g ⁻¹
IBTP	0.78 wt%	0.9 wt%	7.8 wt%	0.81cm ³ g ⁻¹
Pc-POP	0.62 wt%	0.47 wt%	5.6 wt%	0.55cm ³ g ⁻¹

Conclusions

To conclude, we have prepared three new nitrogen containing porous organic polymers and investigated their potential for CO₂ adsorption and gas storage. By varying the nitrogen content of the building blocks, the porous polymers possess different basicity and moderate surface areas, indicating that the current synthetic approach does not provide precise control over pore metrics. The resulting porous polymers are chemically and thermally stable, and the best performing one exhibited very high CO₂ uptake (up to 3.75 mmol g⁻¹) and reasonable selectivities based on initial slope calculations: CO₂/N₂ (51 at 273 K) and CO₂/CH₄ (6.4 at 273 K). These results highlight the potential of nitrogen rich porous polymers in postcombustion CO₂ capture and separation.

References

- 1) O. K. Farha, A. M. Spokoyny, B. G. Hauser, Y-S. Bae, S. E. Brown, R. Q. Snurr, C. A. Mirkin and J. T. Hupp, *Chem. Mater.*, 2009, **21**, 3033
- 2) N. B. McKeown, *J. Mater. Chem.*, 2010, **20**, 10588
- 3) M. Hashem, C. G. Bezzu, B. M. Kariuki and N. B. McKeown, *Polym. Chem.*, 2011, **2**, 2190
- 4) K. V. Rao, R. Haldar, C. Kulkarni, T. K. Maji, and S. J. George, *Chem. Mater.*, 2012, **24**, 969
- 5) Y. Zhu, H. Long, and W. Zhang, *Chem. Mater.*, 2013, **25**, 1630
- 6) F. J. Uribe-Romo, J. R. Hunt, H. Furukawa, C. Klöck, M. O’Keeffe and O. M. Yaghi, *J. Am. Chem. Soc.*, 2009, **131**, 4570
- 7) S. Wan, F. Gándara, A. Asano, H. Furukawa, A. Saeki, S. K. Dey, L. Liao, M. W. Ambrogio, Y. Y. Botros, X. F. Duan, S. Seki, J. F. Stoddart and O. M. Yaghi, *Chem. Mater.*, 2011, **23**, 4094
- 8) V. S. P. K. Neti, X. Wu, S. Deng and L. Echegoyen, *Polym. Chem.*, 2013, **4**, 4566.
- 9) S.-Y. Ding, J. Gao, Q. Wang, Y. Zhang, W.-G. Song, C.-Y. Su and W. Wang, *J. Am. Chem. Soc.*, 2011, **133**, 19816

- 10) J. Sculley, D. Yuan and H-C. Zhou, *Energy Environ. Sci.*, 2011, **4**, 2721
- 11) M. G. Rabbani, A. K. Sekizkardes, Z. Kahveci, T. E. Reich, R. Ding and H. M. El-Kaderi, *Chem. Eur. J.*, 2013, **19**, 3324
- 12) H. A. Patel, F. Karadas, J. Byun, J. Park, E. Deniz, A. Canlier, Y. Jung, M. Atilhan, and C. T. Yavuz, *Adv. Funct. Mater.*, 2013, **23**, 2270.
- 13) P. Pandey, A. P. Katsoulidis, I. Eryazici, Y. Wu, M. G. Kanatzidis, and S. T. Nguyen, *Chem. Mater.*, 2010, **22**, 4974
- 14) P. Pandey, O. K. Farha, A. M. Spokoyny, C. A. Mirkin, M. G. Kanatzidis, J. T. Hupp and S. T. Nguyen, *J. Mat. Chem.*, 2011, **21**, 1700
- 15) Y. Jin, Y. Zhu and W. Zhang, *CrystEngComm*, 2013, **15**, 1484
- 16) S. Yang, J. Sun, A. J. Ramirez-Cuesta, S. K. Callear, W. I. F. David, D. P. Anderson, R. Newby, A. J. Blake, J. E. Parker, C. C. Tang and M. Schröder, *Nat. Chem.*, 2012, **4**, 887.
- 17) P. Kuhn, M. Antonietti and A. Thomas, *Angew. Chem., Int. Ed.*, 2008, **47**, 3450
- 18) F. J. Uribe-Romo, C. J. Doonan, H. Furukawa, K. Oisaki and O. M. Yaghi, *J. Am. Chem. Soc.*, 2011, **133**, 11478.
- 19) M. Zhang, Z. Perry, J. Park, H-C Zhou, *Polymer.*,
- 20) M. G. Rabbani and H. M. El-Kaderi, *Chem. Mater.*, 2011, **23**, 1650
- 21) M. G. Rabbani and H. M. El-Kaderi, *Chem. Mater.*, 2012, **24**, 1511
- 22) M. G. Rabbani, T. E. Reich, R. M. Kassab, K. T. Jackson and H. M. El-Kaderi, *Chem. Commun.*, 2012, **48**, 1141
- 23) K. Sumida, D. L. Rogow, J. A. Mason, T. M. McDonald, E. D. Bloch, Z. R. Herm, T. H. Bae, J. R. Long, *Chem. Rev.*, 2012, **112**, 724.
- 24) T. E. Reich, S. Behera, K. T. Jackson, P. Jena and H. M. El-Kaderi, *J. Mater. Chem.*, 2012, **22**, 13524

Chapter 4

Synthesis of Metal Organic Framework

Introduction

Fluorescent metal organic frameworks are by far the most widely explored type of MOF sensors to date.¹⁻⁵ The popularity of fluorescence over other transduction mechanisms is mainly due to a visible indicator of change. Fluorescence spectroscopy is highly useful because it is well established and the detection limits can reach the single molecule level.⁶ Since there are many different explosive materials, it is important to develop a sensor that is sensitive to a wide range of explosive molecules without being sensitive to other interfering materials. The most common explosives are nitrogen-containing organic compounds, such as trinitrotoluene (TNT), trinitrophenol (TNP), and cyclotrimethylenetrinitramine (RDX). Explosives are electron poor species which may undergo electron transfer with an electron rich molecule in order to be detected.⁷⁻¹⁰ Recently, metal organic frameworks have become materials of interest for explosive detection because they can contain electron rich organic building blocks, making them good candidates for this application.¹¹⁻¹⁵

Another advantage of MOF-based sensing materials is that the organic units can be synthetically tailored to improve detection capabilities. Conjugated molecules are interesting candidates for explosive detection due to their amplified fluorescence responses when compared to those of small molecules.¹⁶⁻²² Fluorescence quenching signals the insertion of an analyte that quenches the fluorescence of the conjugated polymer, as shown in Figure 1 (A-C).

The MOFs presented in this chapter are three dimensional (3D) microporous structures. All of these materials have 3D open channels but different pore sizes. This chapter is focused on the rational design and synthesis of 1,3,5-benzenetribenzoate (BTB) and its Zn(II) 3D-MOF and its graphene composite. Micrometer-sized particles of this Zn(II)-MOF and its graphene composite are strongly fluorescent when dispersed in ethanol and show selective sensing of nitroaromatics (e.g. nitrobenzene, DNT, TNT) through a fluorescence quenching mechanism. The triphenylbenzene was introduced to

make toroidal effect. Zinc (II) ions were chosen as the metal connector because of their high complexation affinity with carboxylates and nondetrimental effect on the fluorescence. MOF-177 crystals were synthesized according to published procedures using 1,3,5-benzenetribenzoate (BTB) and zinc nitrate hexahydrate as the precursors, and diethylformamide (DEF) as the solvent. The MOF-177/BFG composite was synthesized using large amounts of BFG (30 wt%) added into a sonicated mixture of zinc nitrate/BTB in an ampoule, subsequently swirled vigorously after adding BFG, flame sealed and heated in an oven at 100°C for 23 hours and cooled down slowly. The MOF-177/BFG composite was filtered and washed with DEF to remove the starting materials, dried under vacuum overnight and characterized. The phase purity of the bulk material was confirmed by powder X-ray diffraction. The sharp diffraction peaks in the powder XRD pattern of the MOF-177 (Fig. 2) indicate that these particles are highly crystalline in nature. The SEM image of the MOF (Fig. 2) is also indicative of a highly crystalline structure. The fluorescence spectrum of the micrometer-sized particles of the MOF dispersed in ethanol exhibits strong fluorescence peaks at 470 nm upon excitation at 350 nm.

The synthesis of MOF-177/BFG and DPyP were carried out solvothermally in a mixture of DEF or DMF in glass vials at 100°C for 72 h. The chemical connectivity and composition of all the MOFs presented here were characterized by several analytical methods such as Fourier-Transform infrared spectroscopy (FT-IR), powder X-ray diffraction (PXRD), BET surface area measurements, scanning electronic microscopy, transmission electron microscopy, Raman spectroscopy, and fluorescence quenching titrations.

Experimental Methods

All chemicals and solvents were purchased from Sigma-Aldrich or Alfa Aesar. Fourier transform Infrared (FT-IR) spectra were recorded on a Perkin-Elmer Spectrum one infrared spectrometer (ATR).

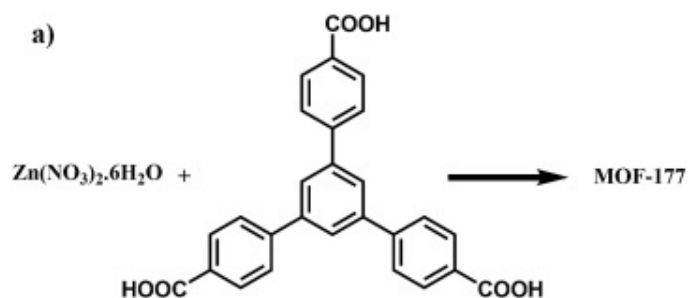
^1H NMR spectra were recorded on JEOL 600MHz spectrometer, where chemical shifts (δ in ppm) were determined with a residual proton of the solvent as standard. Matrix-assisted laser desorption ionization time-of-flight mass (MALDI-TOF MS) spectra were recorded on Bruker benchtop microflex model using matrix trihydroxyanthracene. Field-emission scanning electron microscopy (FE-SEM) was performed on a Hitachi S-4800 fitted with an EDAX energy-dispersive spectrometry system by adhering sample on a sampling platform. Powder X-ray diffraction (PXRD) data were recorded on a Bruker DiscoverD8 model diffractometer by depositing powder on plastic substrate, from $2\theta = 1^\circ$ up to 30° with 0.05° increment. In order to determine pore textural properties including the specific Brunauer–Emmet–Teller (BET) surface area, pore volume and pore size distribution, nitrogen adsorption and desorption isotherm on MOF-177 and MOF-177/BFG samples at 77 K were measured in an ASAP-2020 adsorption apparatus (Micromeritics). The as-synthesized samples were degassed in situ at 150°C with a heating rate of $3^\circ\text{C}/\text{min}$ under a vacuum (0.0001 mmHg) for 12 h before nitrogen adsorption measurements in order to ensure the micro-channels in the structure were guest-free. The Brunauer–Emmett–Teller (BET) method was utilized to calculate the specific surface areas by using the non-local density functional theory (NLDFIT) model, the pore volume was derived from the sorption curve. Thermogravimetric analysis from 30 – 700°C was carried out on a Mettler-Toledo thermogravimetric analyzer in an N_2 atmosphere using a $3^\circ\text{C}/\text{min}$ ramp time.

4.1 *Synthesis and characterization of MOF-177 and MOF-177/BFG composite*

Synthesis of graphene oxide (GO), benzoic acid functionalized reduced GO (BFG) and MOF-177:

GO was prepared from natural graphite flakes according to the Hummers method. Functional groups (epoxy, hydroxyl) were removed by reduction with NaBH_4 to make chemically reduced GO (r-GO). Further r-GO was functionalized with benzoic acid (Figure 88) by using the diazonium grafting method, and this allowed the basal planes of r-GO to become extended by benzoic acid groups. MOF-

177 crystals were synthesized according to published procedures using 1,3,5-benzenetribenzoate (BTB) and zinc nitrate hexahydrate as the precursors, and diethylformamide (DEF) as the solvent. The MOF-177/BFG composite was synthesized using large amounts of BFG (30 wt%) added into a sonicated mixture of zinc nitrate/BTB in an ampoule, subsequently swirled vigorously after adding BFG, flame sealed and heated in an oven at 100°C for 23 hours and cooled down slowly. The MOF-177/BFG composite was filtered and washed with DEF to remove the starting materials, dried under vacuum overnight and characterized. We used the same strategies developed by Bando *et al* and Loh *et al* to make a MOF-177/BFG composite using reduced graphene oxide, functionalized with benzoic acid using the diazonium grafting method to functionalize the graphene basal planes. As a result we obtained 1 mm long and 50 μm wide MOF-177/BFG nanorod composites which are potentially useful for the detection of nitro aromatic explosives. Benzoic acid functionalized graphene (BFG) was synthesized following the procedure¹¹ reported by Loh *et al* as shown in Figure 88.



Scheme 1. Synthetic scheme for MOF-177

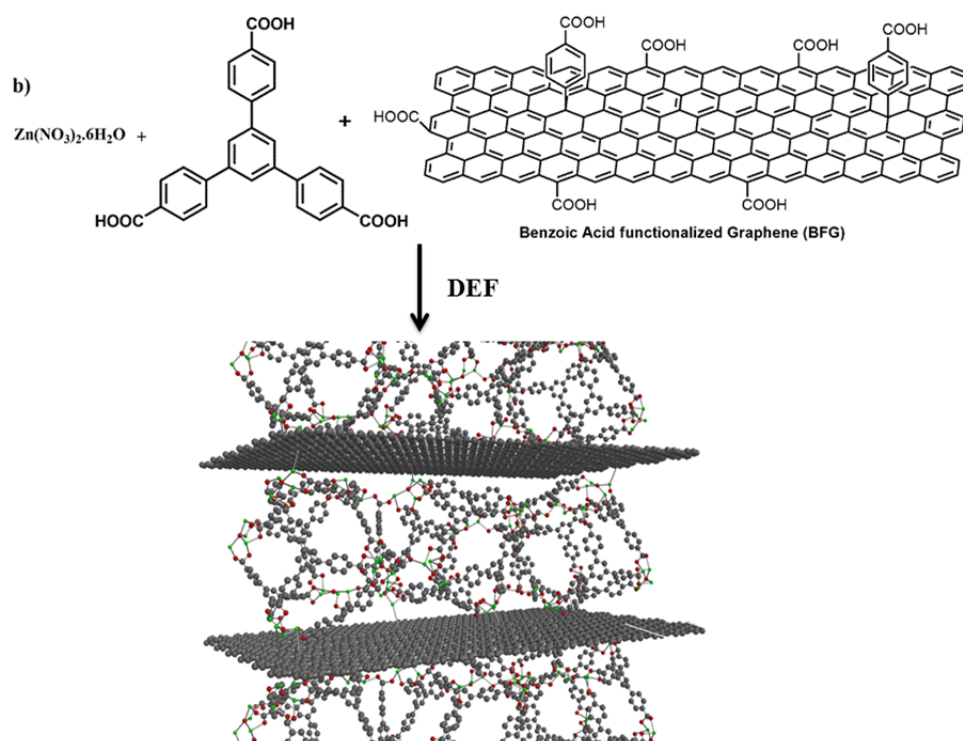


Figure 84. Synthetic scheme for (a) MOF-177 (b) MOF-177/BFG composite and TEM image of the composite MOF-177/BFG.

4.1.1 Powder X-ray diffraction and simulation of MOF-177/BFG

All samples except zinc nitrate showed a most intense peak at $2\theta = 5.6$ and other intense peaks at $2\theta = 6, 6.5$ and 11.2 which are slightly offset by $\sim 0.4^\circ$ relative to the original MOF-177 diffraction peaks reported^{5b} by Yaghi *et al.* We believe that this minor offset is due to interactions between the MOF and the graphene sheets (Figure 89).

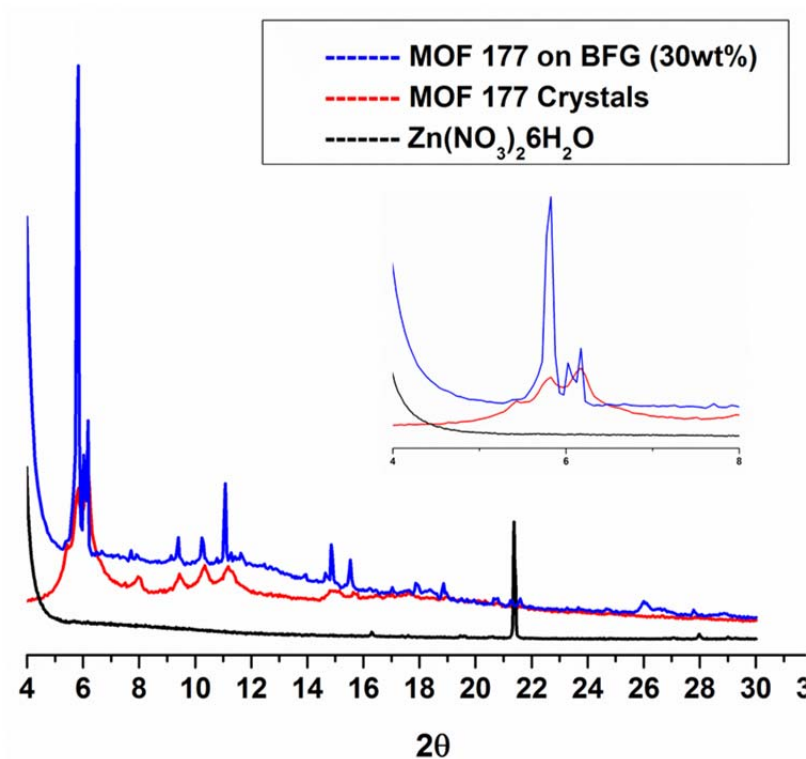


Figure 85. Powder XRD patterns of MOF-177 (red), MOF-177/BFG 30 wt% (blue) and $\text{Zn}(\text{NO}_3)_2 \cdot 6\text{H}_2\text{O}$ (black) and N_2 adsorption-desorption isotherms (inset).

4.1.2 FT-IR measurements of MOF-177/BFG

The FT-IR spectrum of the MOF-177/BFG composite largely resembles that of MOF-177 (Figures 90 and 91) with broad peaks at 1670 cm^{-1} and 1710 cm^{-1} , assignable to the C=O stretch of carboxylate groups from the BFG and the stretch of the bidentate coordination of the carboxylate group with the zinc clusters in the MOF. Furthermore, broad bands between 2500 and 3300 cm^{-1} confirmed the presence of carboxyl groups in the MOF-177/BFG composite.

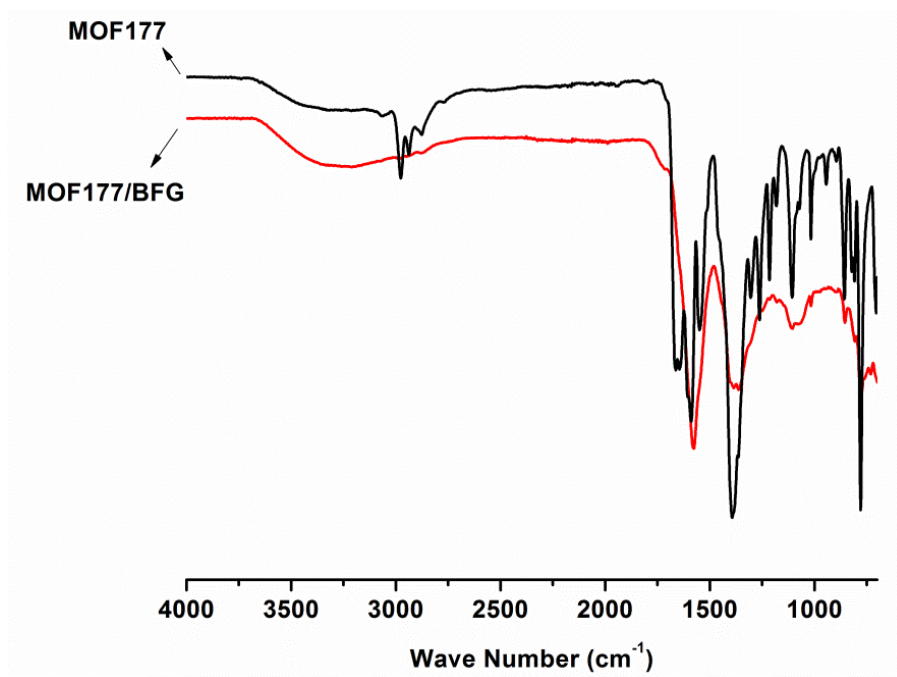


Figure 86. IR spectra of MOF-177 (black) and MOF-177/BFG composite (red)

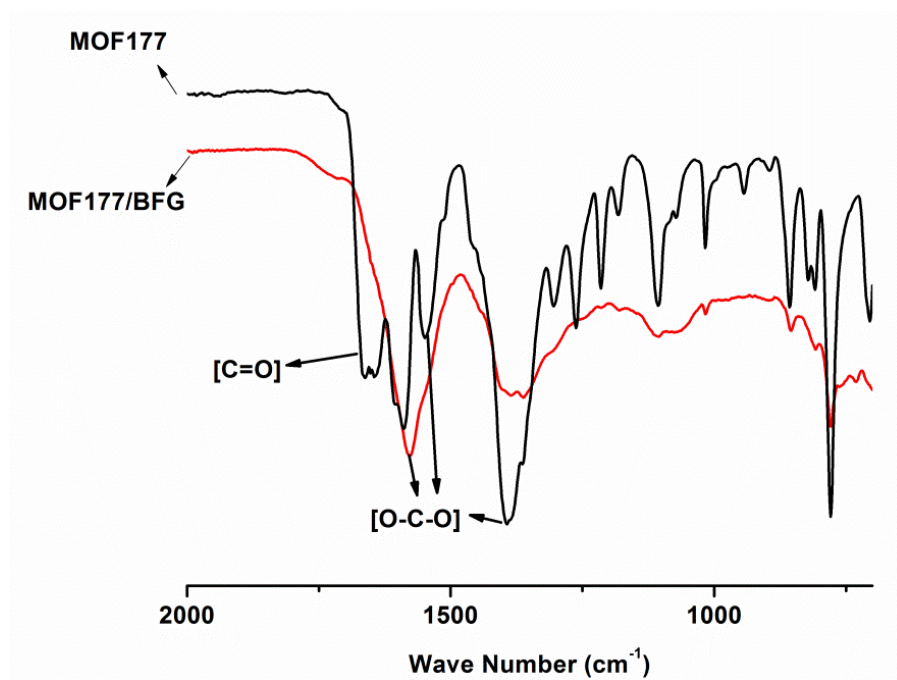


Figure 87. Expanded IR spectra of MOF-177 (black) and MOF-177/BFG composite (red)

4.1.3 Raman spectrum of MOF-177/BFG

Raman spectroscopic analysis (Figure 92) showed equal intensity of both G and D bands which are characteristic of sp^3 and sp^2 hybridized carbon bonds, respectively. This means the basal plane of graphene is sufficiently functionalized with carboxylic acid and other functional groups.

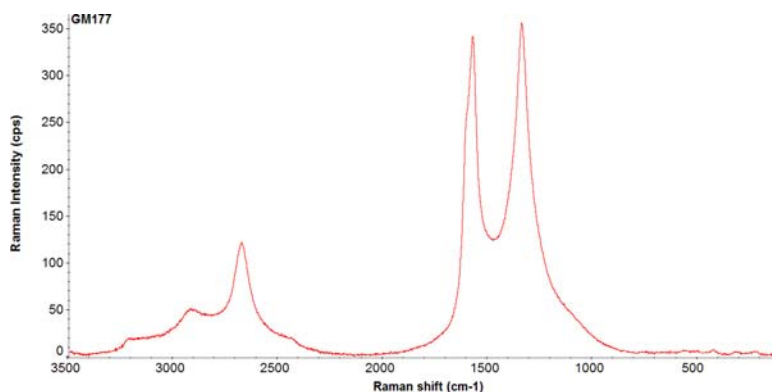


Figure 88. Raman spectrum of MOF-177/BFG composite.

4.1.4 Gas adsorption measurements of MOF-177/BFG

The structural differences between the MOF-177 and MOF-177/BFG composites are also observed from the BET surface area measurements (N_2 adsorption–desorption). We did not perform the surface area measurement for BFG, since it is known to be a very low porosity material. The isotherms for MOF-177 and MOF-177/BFG composites exhibit type-IV curves (Figure 93), indicative of the mesoporous nature of the composites. The porosity of MOF-177/BFG is lower than for the parent MOF-177. This could be due to incorporation of small amounts of BFG within the pores of MOF-177. Reduction of the porosity of GO-MOF composites was also observed in previous reports.¹¹ The BET surface area value for the MOF-177/BFG was $321\text{ m}^2\text{ g}^{-1}$, maybe due to a decrease in the size of the MOF-177 crystals counterbalancing the amount of BFG layers. The total pore volume was calculated to

be $0.41\text{cm}^3\text{ g}^{-1}$ and the average pore size of BFG/MOF-177 was calculated to be 15\AA by applying nonlocal density functional theory (NLDFT) to the BET measurements (Figure 94). By comparing the NLDFT pore size with the TEM image, approximately 20 unit cells of MOF-177 must exist within the adjacent graphene sheets (Figure 96).

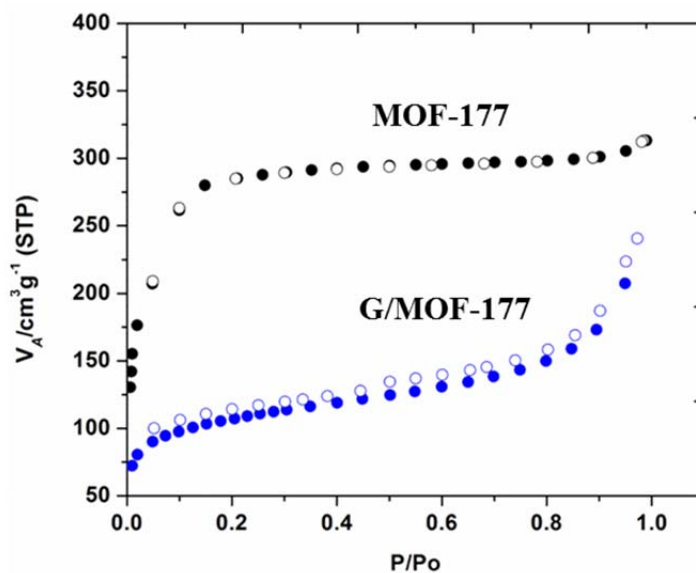
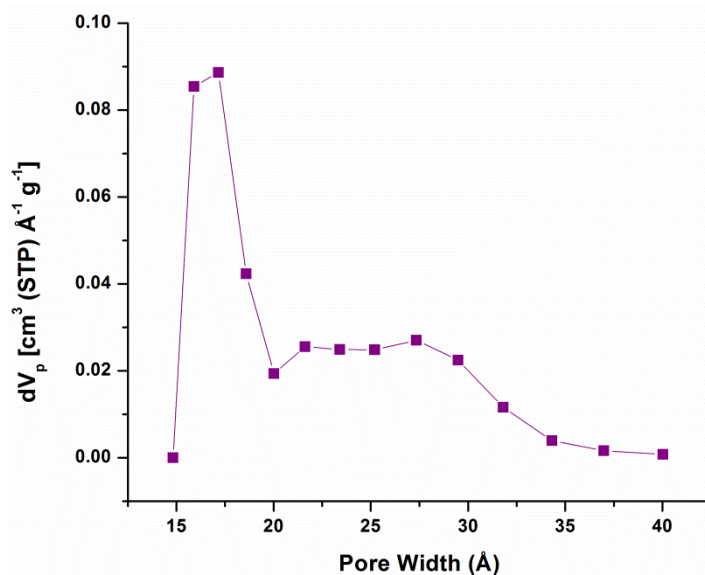


Figure 89. N_2 at 77K adsorption (filled symbols) and desorption (empty symbols) isotherm curves.



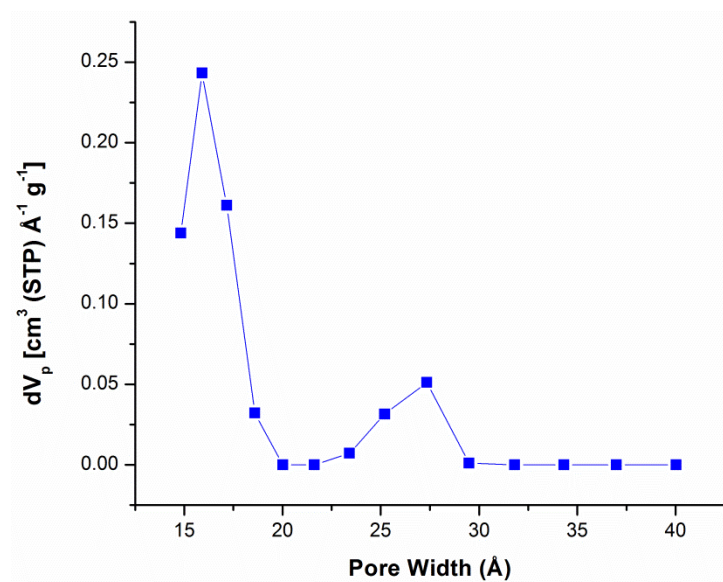
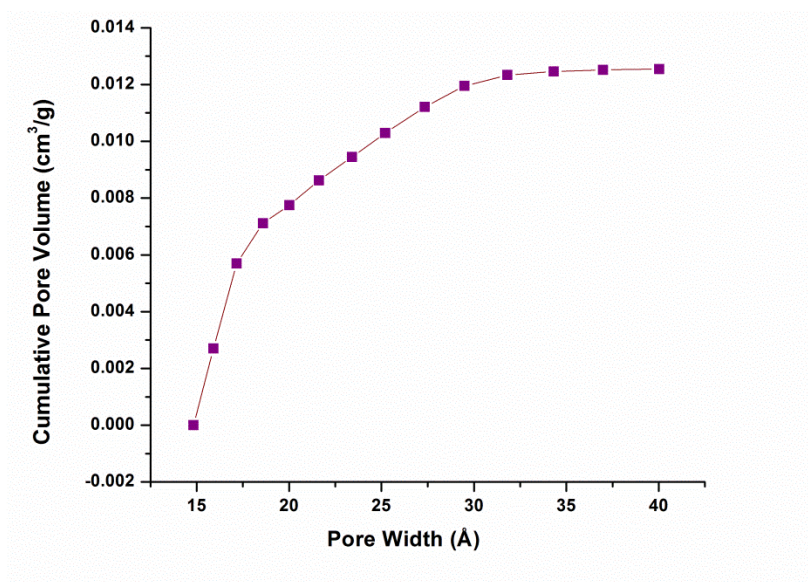


Figure 90. Differential (top: MOF-177/BFG, bottom: MOF-177) pore size distribution plot from the application of the NLDFIT model to the N_2 isotherm.



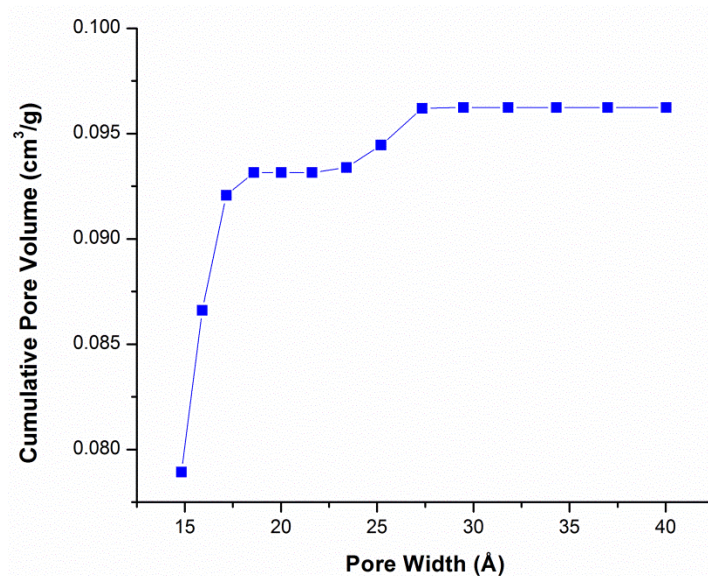


Figure 91. Cumulative (top: MOF-177/BFG, bottom: MOF-177) pore size distribution plot from the application of the NLDFT model to the N₂ isotherm.

4.1.5 Scanning and Transmission electron microscopy images of MOF-177/BFG

The SEM analysis (Figure 96) of the MOF-177/BFG composite showed 1mm long and 50μm wide rod-shaped needles with uniform morphology. These findings show that the MOF-177/BFG composite has rod/wire architectures as previously proposed by Loh *et al* for MOF-5/BFG. TEM analysis of the MOF-177/BFG showed regular patterns with an interlayer distance around 3.2nm (Figure 96). The morphology of these MOF-177/BFG composites showed a clear difference when compared to that of MOF-177, which shows small cubic crystal shapes. Both XRD and SEM showed that the phase and structure of the synthesized composites are crystalline and rod shaped.

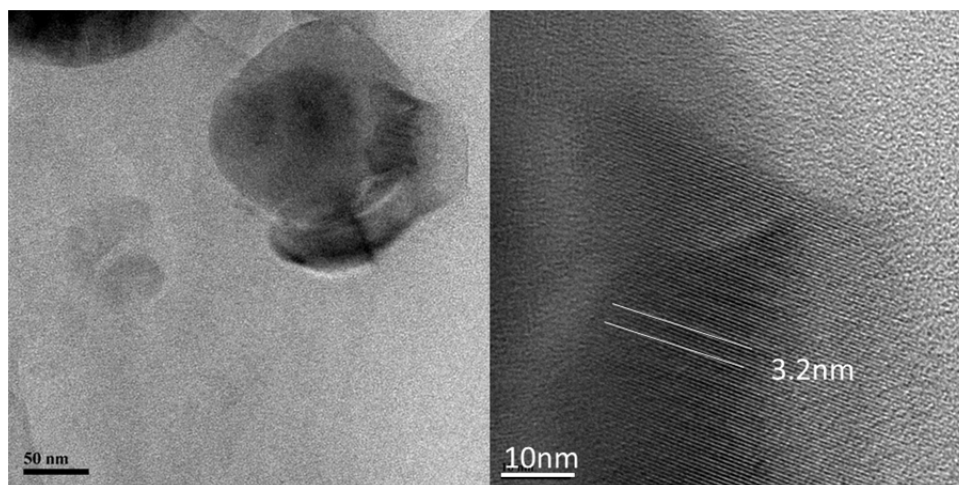
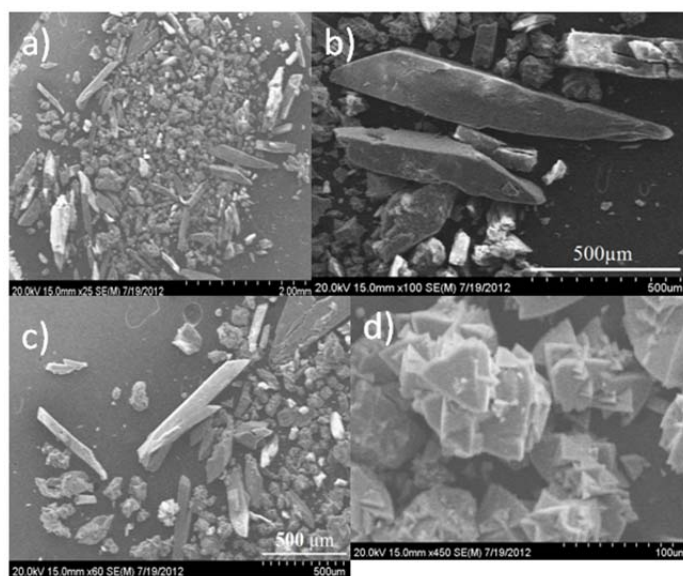


Figure 92. SEM images (above) for (a), (b) and (c) MOF-177/BFG show 1mm in length and 50 μ m wide (d) MOF-177 (cubic) and TEM images (below)

4.1.6 Fluorescence quenching titration of MOF-177 and MOF-177/BFG

Fluorescence emission spectra were recorded at 298 K. The fluorescence of finely grounded MOF-177 and MOF-177/BFG were measured by dispersing 5 mg of it in 2 mL of ethanol and subsequently placed in a quartz cell. All titrations were carried out by gradually adding quenchers (0.01M) solutions. Each titration was repeated at least three times to get agreeable value. Dispersed solutions of MOF were excited at $\lambda = 370$ nm and their corresponding emission wavelength was

monitored from $\lambda = 400$ nm to 540 nm. The fluorescence efficiency was calculated by $[(I_0-I)/I_0] \times 100 \%$, where I_0 and I are the initial and final fluorescence intensities.

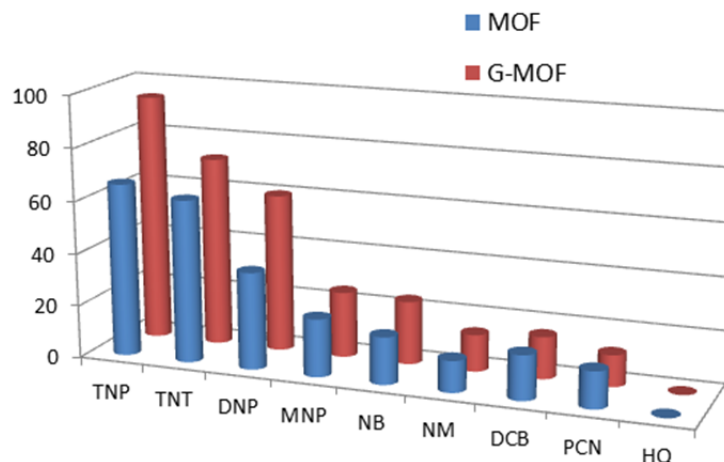
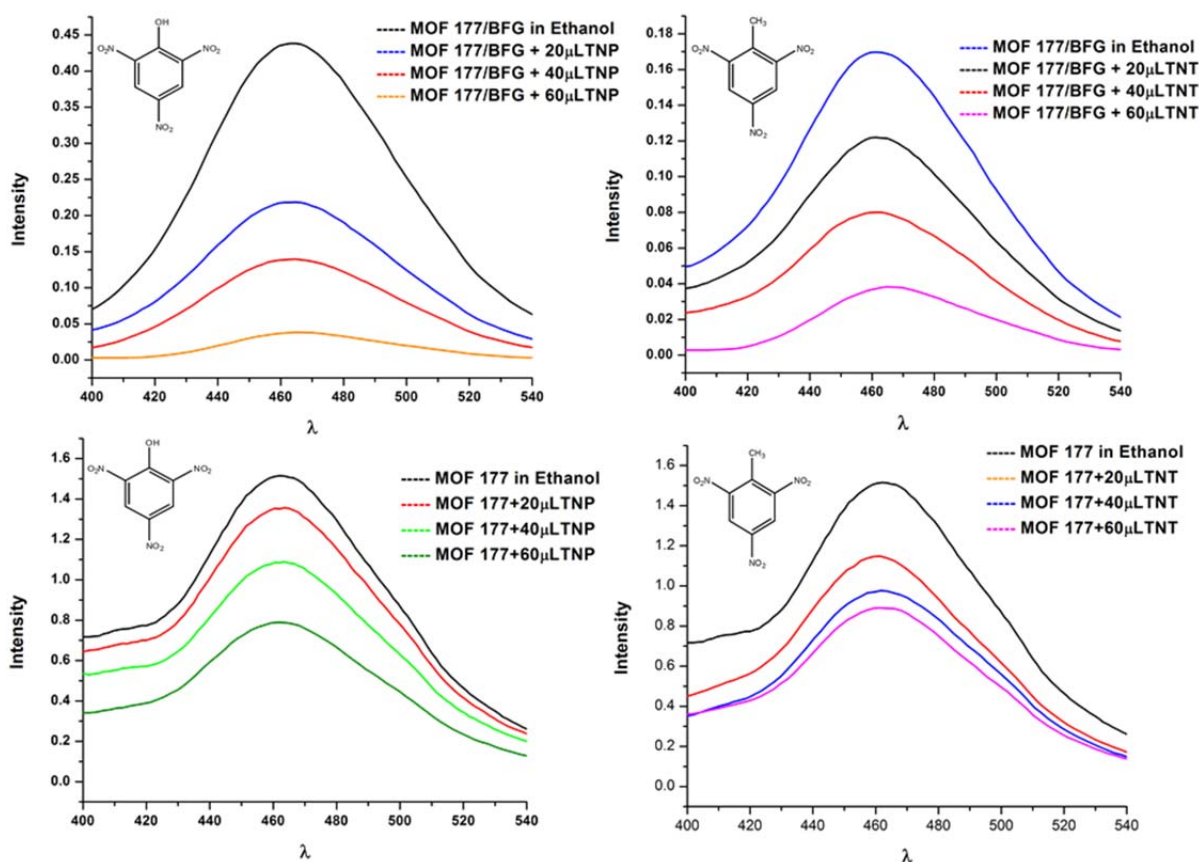
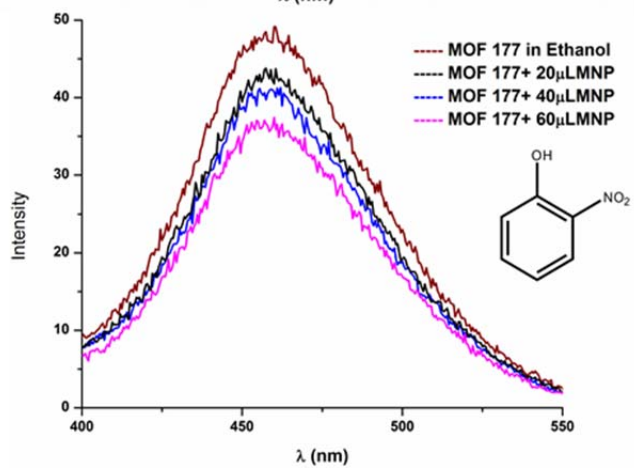
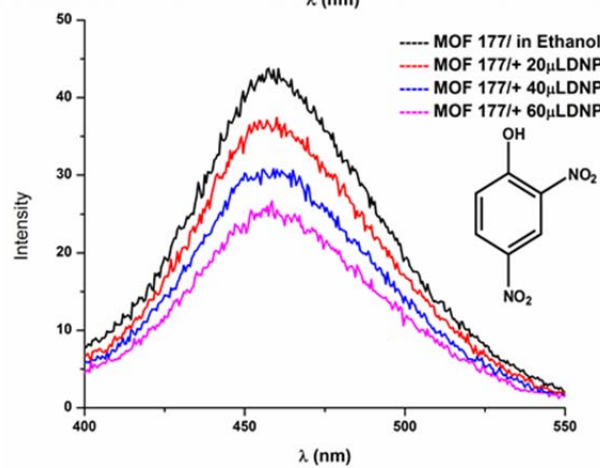
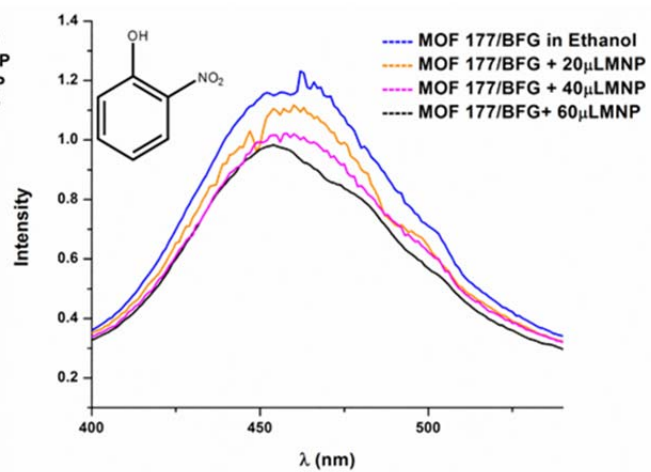
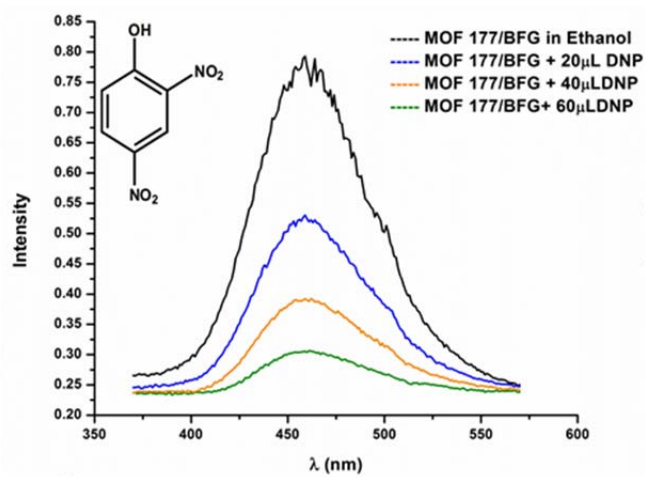


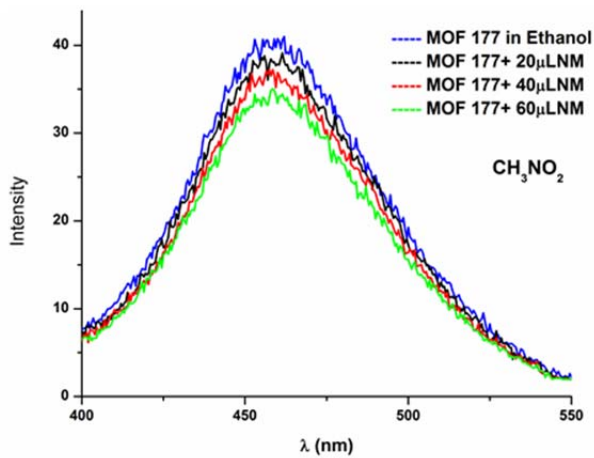
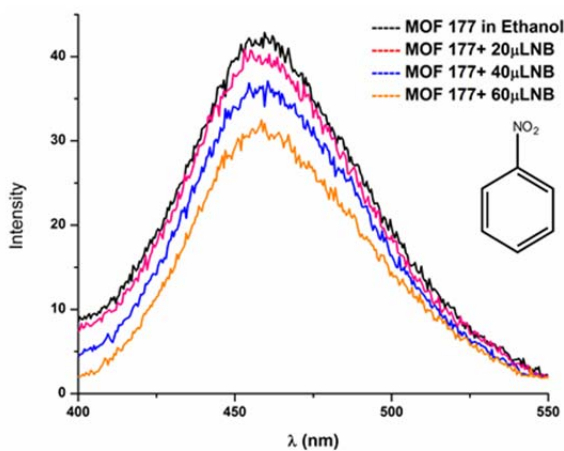
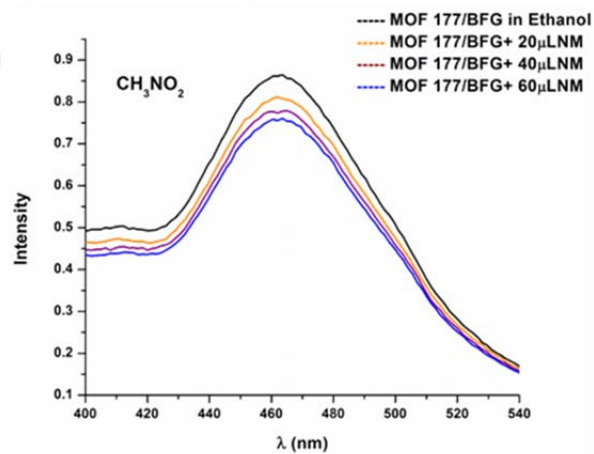
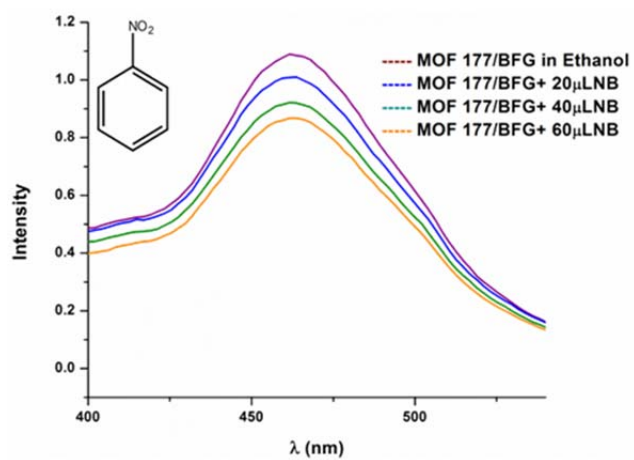
Figure 93. Fluorescence quenching selectivity of MOF-177/BFG [trinitrophenol (TNP), trinitrotoluene (TNT), dinitrophenol (DNP), mononitrophenol (MNP), nitrobenzene (NB), nitromethane (NM), dicyanobenzene (DCB), pyridinecarbonitrile (PCN) and hydroquinone (HQ)].

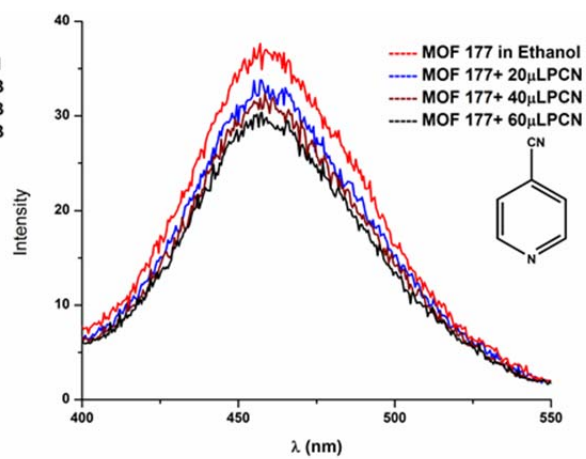
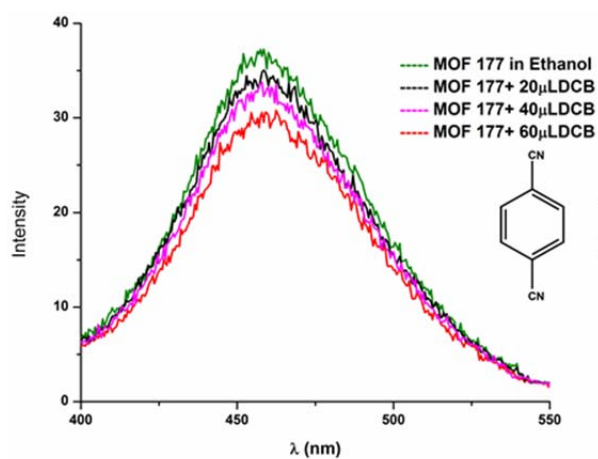
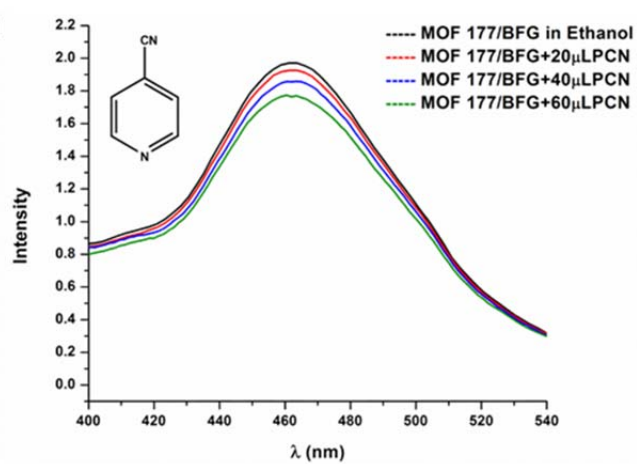
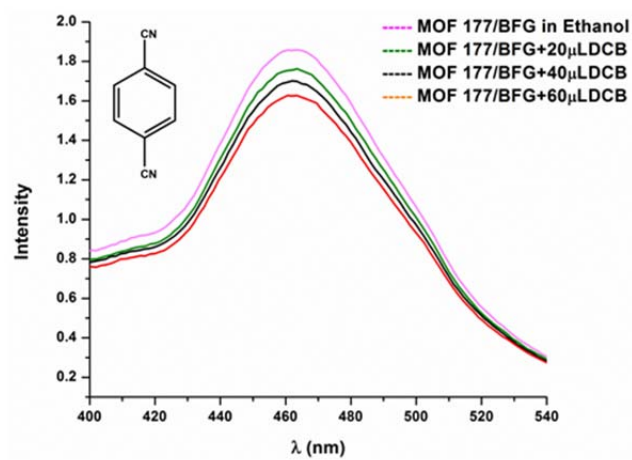
The fluorescence spectrum of the MOF-177/BFG composite dispersed in ethanol exhibited a strong emission at 460nm when excited at 370nm. To explore the ability of the MOF-177/BFG composite to sense trace quantities of nitro aromatic explosives, fluorescence-quenching titrations were performed with incremental additions of six nitro compounds to the MOF-177/BFG composites dispersed in ethanol. Fast, pronounced and selective fluorescence quenching was observed upon addition of the analytes. The bright blue emission of the MOF-177/BFG composite was quenched nearly 94% upon addition of 60 μ L of TNP, whereas only 72% of the fluorescence intensity was quenched using 60 μ L of TNT at the same concentration (0.01M). In the case of other nitro aromatic analytes, approximately 20% of the initial fluorescence intensities were quenched using 60 μ L of the analytes (Figure 11). Fluorescence intensities were almost unchanged upon addition of *p*-hydroquinone, pyridine carbonitrile and terephthalonitrile as control experiments, indicating that the MOF-177/BFG composite is selective towards TNP (Figure 97). Stern-Volmer plots for MOF-177/BFG were subsequently

constructed and the quenching rate constant values were found to be similar to those for other reported MOFs (Figure 99).⁹ There was some partial fluorescence quenching observed in the presence of cyano compounds due to their partial electron withdrawing nature. We further tested the ability of pure MOF crystals to sense nitroaromatic compounds. The fluorescence quenching intensities for TNP and TNT were almost the same and lower than that of the graphene composites. This selectivity can be attributed to the fast and efficient electron and energy transfers with TNP, which has the lowest LUMO energy level at -3.3 eV compared to the other analytes in this study. The high polarizability of the TNP could also facilitate π - π interactions, enhancing the selectivity. The high LUMO energy level of the MOF 177/BFG composite can promote faster electron transfer from the electron rich composite to the electron deficient TNP during the fluorescence quenching process.









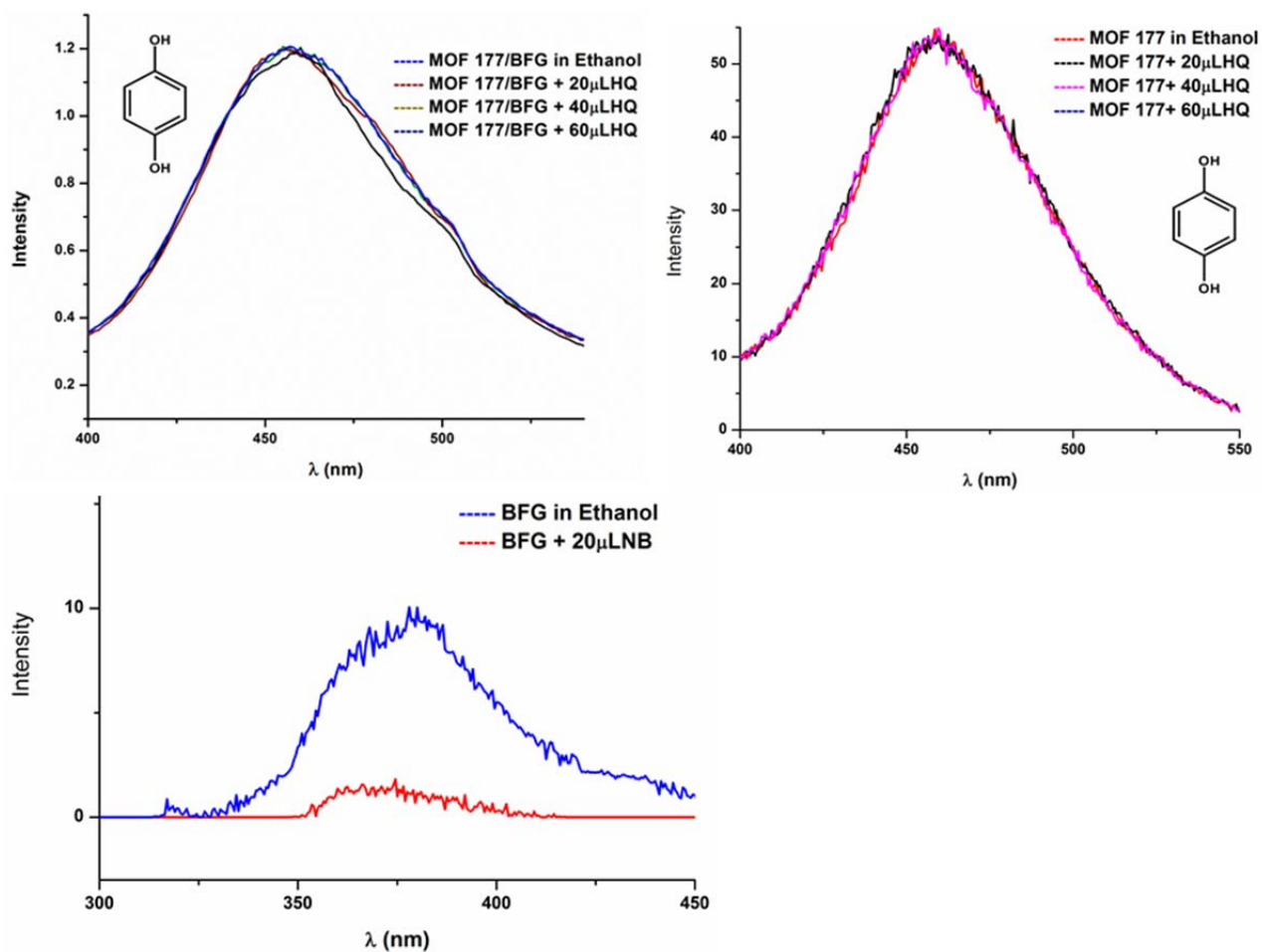


Figure 94. Fluorescence titration spectra of MOF-177 and MOF-177/BFG composites.

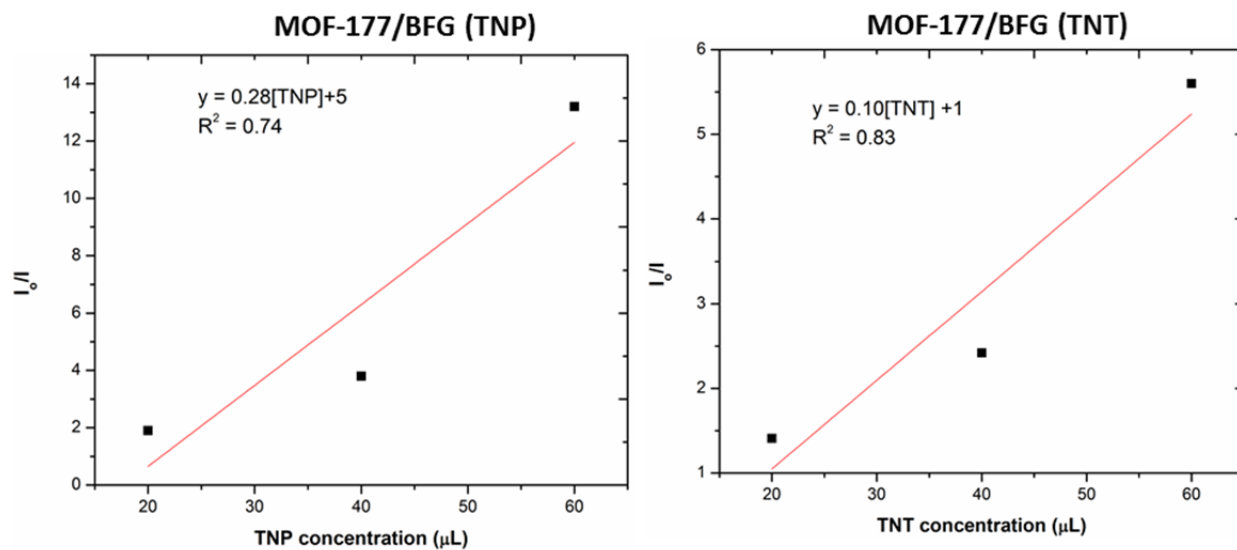


Figure 95: Stern–Volmer plots for quenching of the MOF-177/BFG with TNP and TNT at 25 °C.

4.1.7 Thermogravimetric analysis of MOF-177 and MOF-177/BFG

Thermogravimetric analysis (Figure 100) of the composite and MOF showed that the thermal stability of MOF-177/BFG is increased $\sim 25^{\circ}\text{C}$ compared to the parent MOF-177, probably due to the larger amount of graphene.

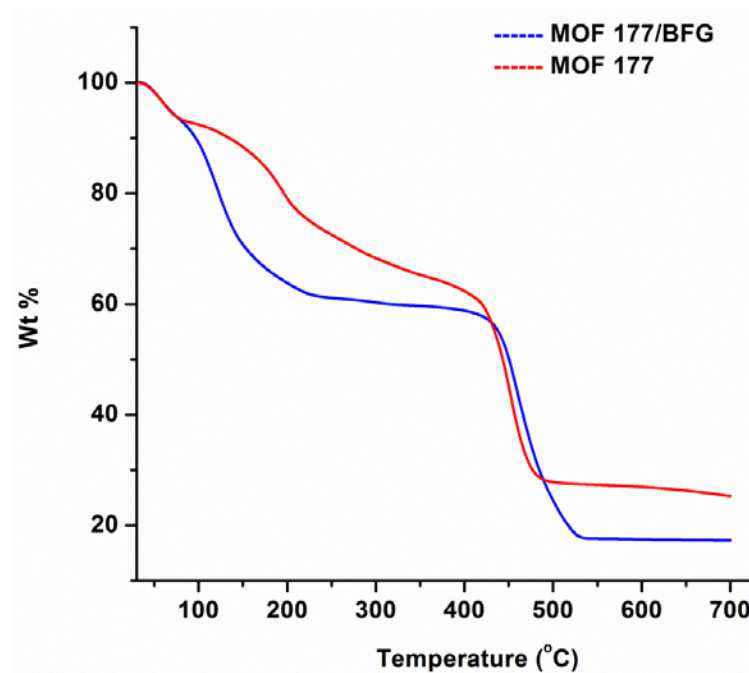


Figure 96. TGA of MOF-177 (red) and MOF-177/BFG composite (blue) obtained up to 700°C using a linear 3°C/min ramp method.

4.2 Synthesis and characterization of ZnDPyP

$\text{Zn}(\text{NO}_3)_2 \cdot 6\text{H}_2\text{O}$ (35.6mg , 0.12mmol), 5,15-bispyridyl-10,20-dibenzyl-porphyrin (36.9mg , 0.06mmol) and 8ml DMF were combined in an ampoule (20ml), sonicated for two minutes, sealed under vacuum and then heated to 100°C for 10hrs. The mixture was allowed to cool down, filtered one time and stored over fresh DMF (4ml). Single crystals suitable for XRD were formed in the filtered mixture. Yield: 45% (18.2mg) based on porphyrin. Elemental analysis (%) calcd. for trans-ZnDPyP ($\text{C}_{42}\text{H}_{26}\text{N}_6\text{Zn} \cdot 1.6\text{DMF}$) Theory: C, 69.57; H, 4.60; N, 13.82. Found: C, 68.74; H, 4.20; N, 13.97, respectively.

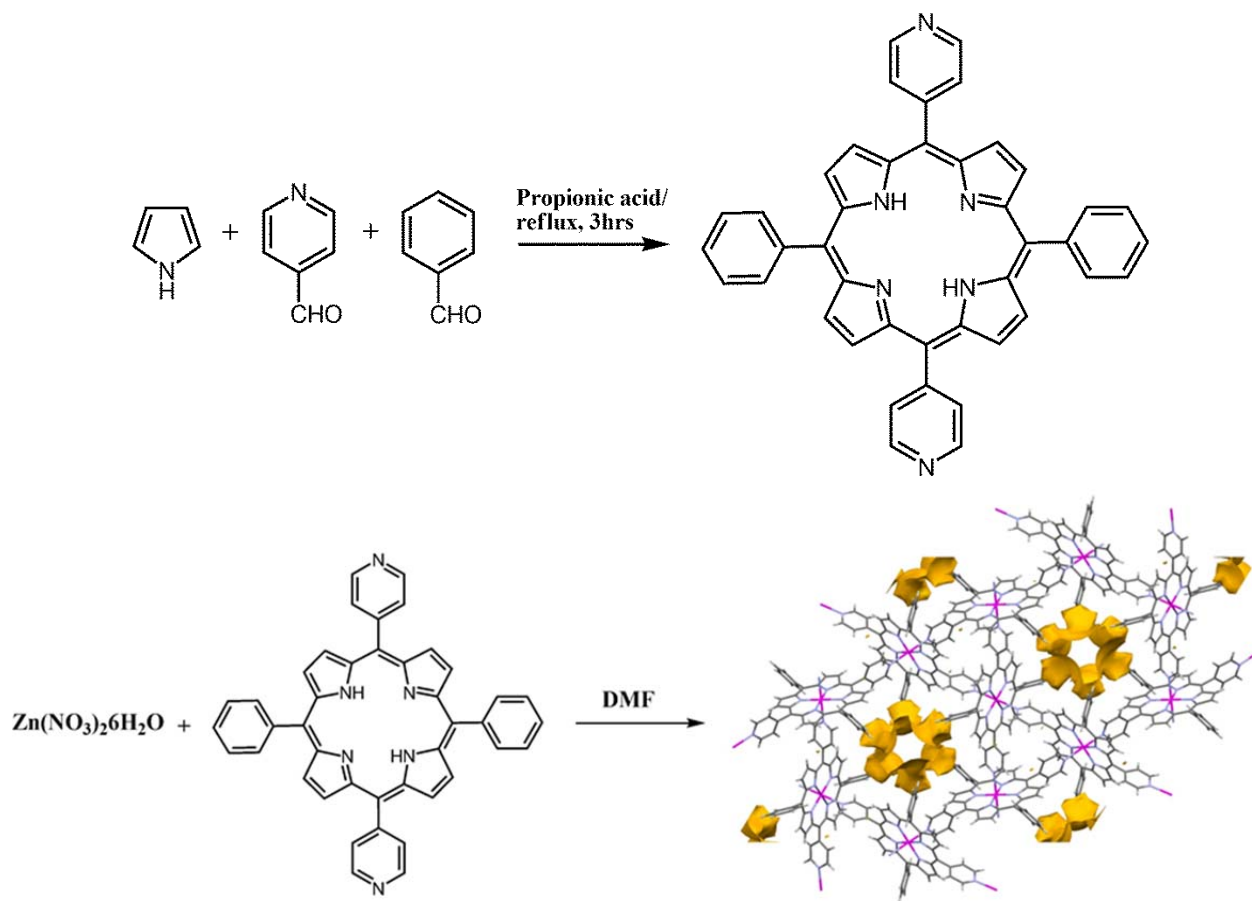


Figure 96. Synthetic scheme for ZnDPyP and crystal packing through the axis c showing the resulting solvent accessible channels (DMF: yellow-gold and voids in the middle)

4.2.1 Single and Powder X-ray diffraction and simulation of ZnDPyP

Suitable single crystals were mounted on a Bruker Smart Apex CCD diffractometer equipped with graphite monochromatized Mo-K α radiation ($\lambda = 0.71073\text{\AA}$) at 298K in the ω -2 θ scan mode. The single crystal structure of the metal-porphyrin was solved using direct methods (SHELXS-97) and refined by full-matrix least-squares based on F^2 using SHELXL-97. Hydrogen atoms were generated geometrically. Crystallographic data and selected bond lengths and angles are given in Table 1, respectively. Powder X-ray diffraction (Cu K α radiation, $\lambda = 1.54\text{\AA}$) was used to determine the phase purity of (trans-DPyP)Zn. Powder X-ray diffraction data were recorded on a Bruker DiscoverD8 model

diffractometer by depositing crushed crystals of (trans-DPyP)Zn on a plastic substrate, from $2\theta = 2^\circ$ up to 30° with 0.05° increment. The most intense diffraction peak at $2\theta = 5.2^\circ$ and the other 2θ values at 9.4, 10.7, and 14.9, respectively.

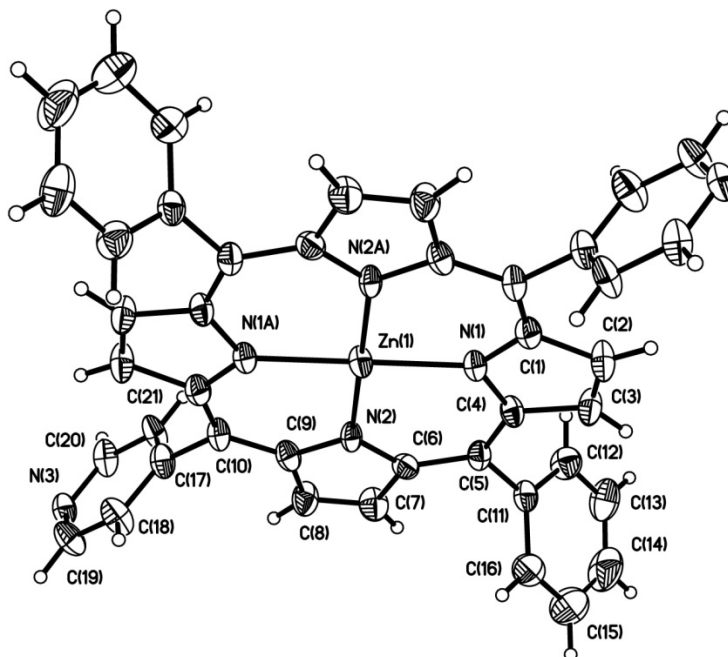


Figure 97. The ellipsoids of trans-ZnDPP are drawn at 35% of probability level. Only the asymmetric part is numbered (above). Octahedral geometry of Zn (red) in the trans-ZnDPP framework (below).

The Zn in the crystal structure adopts distorted octahedral coordination geometry, by coordinating with two pyridyl rings above and below the porphyrin plane. The axial coordination axis is tilted (83°) towards N1. The porphyrin structure itself presents a slight puckering and the aryls are not perpendicular to the mean plane of the porphyrin but tilted, and the dihedral angle of the phenyl ring is 68° while for the pyridyl ring it is 76° towards the porphyrin mean plane.

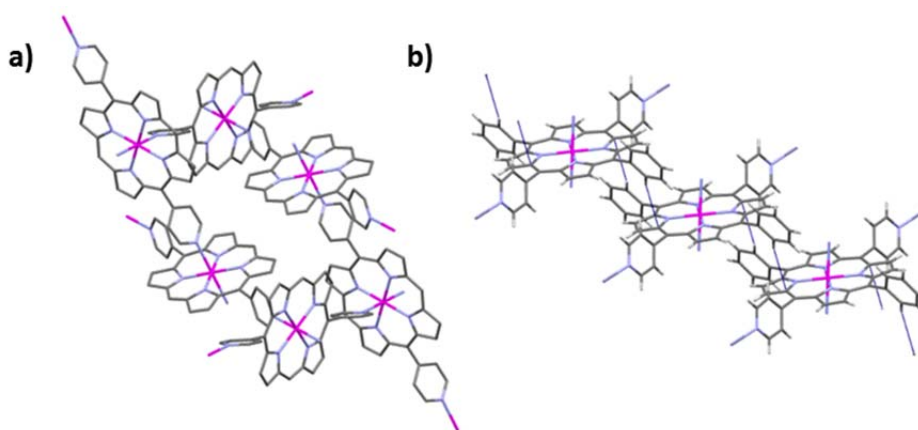


Figure 98. The coordination cycle of (trans-DPyP)Zn formed (a) and H-- π interactions (b). The hydrogens on the phenyl rings have been omitted for clarity.

The coordination network is formed by a 6-membered macrocycle (Figure 103). On this motif each porphyrin has two free sites to extend the network. In addition to the coordination network, there is a reciprocal H $\cdots\pi$ interaction between a phenyl hydrogen (H12) and a pyridyl ring (N1, 1-x,2-y,-z) with a distance of 2.80 Å, which generates a chain through the c axis.

Table 1. Crystal data and structure refinement.

Empirical formula	C ₄₂ H ₂₆ N ₆ Zn
Formula weight	680.06
Temperature	296(2) K
Wavelength	0.71073 Å
Crystal system	Rhombohedral
Space group	<i>R</i> -3
Unit cell dimensions	<i>a</i> = 33.198(5) Å α = 90° <i>b</i> = 33.198(5) Å β = 90° <i>c</i> = 9.351(3) Å γ = 120°
Volume	8925(3) Å ³
<i>Z</i>	9
Density (calculated)	1.139 Mg m ⁻³
Absorption coefficient	0.653 mm ⁻¹
<i>F</i> (0 0 0)	3150
Crystal size	0.018 mm × 0.016 mm × 0.008 mm
Reflections collected	30,540
Independent reflections	3482 [<i>R</i> (int) = 0.2106]
Completeness to theta = 25.00°	99.5%
Absorption correction	Semi-empirical from equivalents
Max. and min. transmission	0.7457 and 0.5979
Refinement method	Full-matrix least-squares on <i>F</i> ²
Final <i>R</i> indices [<i>I</i> > 2 sigma(<i>I</i>)]	<i>R</i> 1 = 0.0692, <i>wR</i> 2 = 0.1553

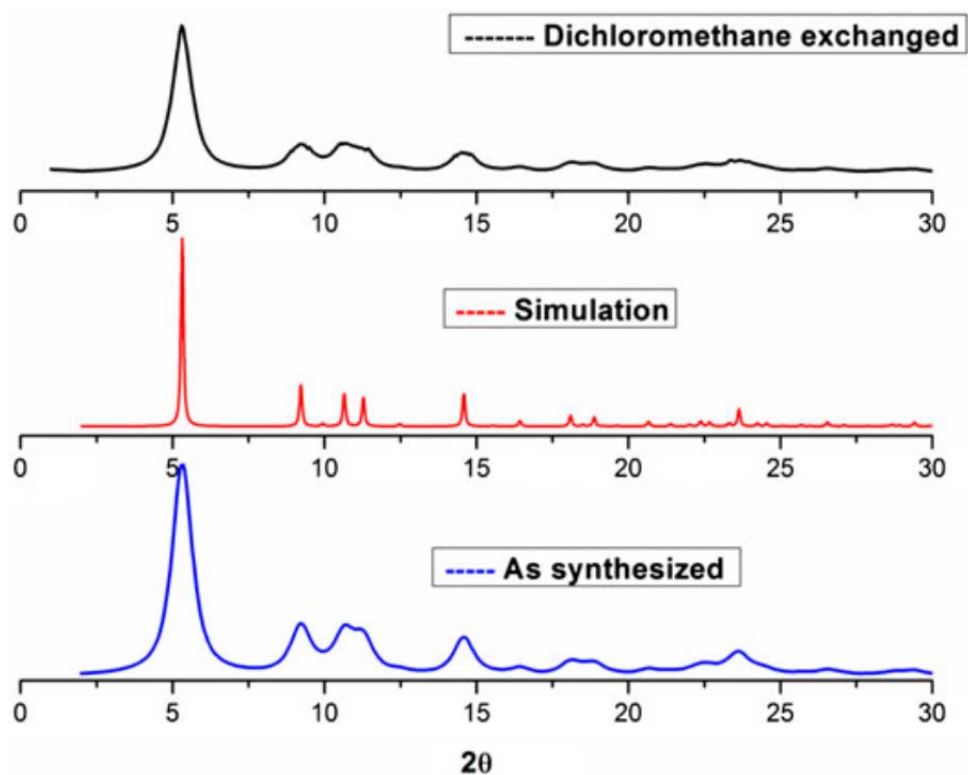


Figure 99. PXRD of (trans-DPyP)Zn.

4.2.2 Thermogravimetric analysis of ZnDPyP

Thermogravimetric analysis of (trans-DPyP)Zn showed ~15% weight loss around 160°C which is the boiling point of DMF (Figure 105). Based on the TGA mass loss we converted the ~15% mass of DMF into moles per unit formula (1.6). Since Hosseini *et al* reported the robustness of the framework by exchanging the solvent molecules, we exchanged the DMF in the channels of the structure with dichloromethane by following the previously published procedure for MOFs. We couldn't observe any significant amount of dichloromethane desorption from the TGA traces after exchanging the solvent from DMF to dichloromethane.

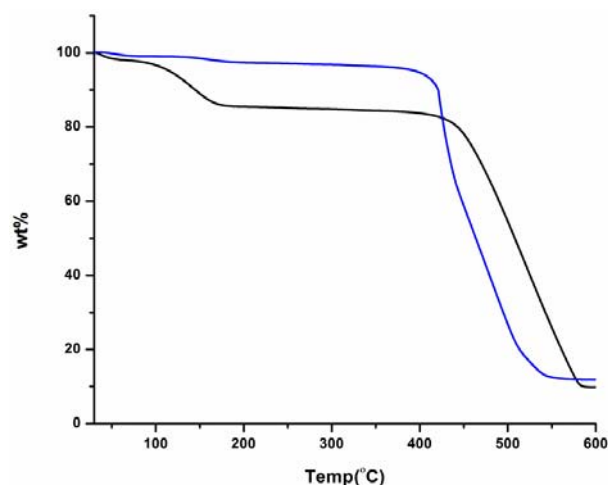


Figure 100. TGA of (trans-DPyP)Zn obtained up to 700°C using a linear 3°C/min ramp method.

Conclusions

A graphene composite containing benzoic acid functionalized graphene oxide and MOF-177 has been prepared. The structure of the precursors is preserved in the composite, where graphene layers from BFG alternate with layers of the MOF structures. Photophysical studies show that the composite exhibits a typical π - π^* transition which gives rise to the highly fluorescent behavior. Upon formation of the metal-organic framework/benzoic acid-functionalized graphene oxide nanocomposite, the nanocomposite shows a pronounced fluorescence enhancement for the detection of trinitrophenol (TNP). In addition, MOF/BFG composites can act as chemosensors, as for TNP and TNT detection. Graphene-based MOF composites could provide a powerful strategy for developing new molecularly defined materials for sensing applications.

References

- 1) A. Lan, K. Li, H. Wu, D. H. Olson, T. J. Emge, W. Ki, M. Hong, and J. Li, *Angew. Chem., Int. Ed.*, 2009, **48**, 2334
- 2) S. Pramanik, C. Zheng, X. Zhang, T. J. Emge, and J. Li, *J. Am. Chem. Soc.*, 2011, **133**, 4153
- 3) S. Shanmugaraju, H. Jadhav, R. Karthik and P. S. Mukherjee, *RSC Adv.*, 2013, **3**, 4940.
- 4) D. Banerjee, Z. Hu, S. Pramanik, X. Zhang, H. Wang, J. Li, *CrystEngComm.*, 2013, **15**, 9745.
- 5) S. Pramanik, Z. Hu, X. Zhang, C. Zheng, S. Kelly, J. Li, *Chem. Eur. J.*, 2013, **19**, 15964.
- 6) J. H. Lee, S. Kang, J. Jaworski, K-Y. Kwon, M. L. Seo, J. Y. Lee, and J. H. Jung, *Chem. Eur. J.*, 2012, **18**, 765.
- 7) J. H. Lee, J. Jaworski, J. H. Jung, *Nanoscale.*, 2013, **5**, 8533.
- 8) L. E. Kreno, K. Leong, O. K. Farha, M. Allendorf, R. P. Van Duyne, and J. T. Hupp, *Chem. Rev.*, 2012, **112**, 1105.
- 9) Z. Hu, S. Pramanik, K. Tan, C. Zheng, W. Liu, X. Zhang, Y. J. Chabal, and J. Li, *Cryst. Growth. Des.*, 2013, **13**, 4204.
- 10) S. S. Nagarkar, B. Joarder, A. K. Chaudhari, S. Mukherjee, S. K. Ghosh, *Angew. Chem., Int. Ed.*, 2013, **52**, 2881.
- 11) A. K. Chaudhari, S. S. Nagarkar, B. Joarder, and S. K. Ghosh, *Cryst. Growth. Des.*, 2013, **13**, 3716.
- 12) B. Gole, A. K. Bar and P. S. Mukherjee, *Chem. Commun.*, 2011, **47**, 12137.
- 13) S. Shanmugaraju, S. A. Joshi and P. S. Mukherjee, *J. Mater. Chem.*, 2011, **21**, 9130.
- 14) V. Vajpayee, H. Kim, A. Mishra, P. S. Mukherjee, Peter J. Stang, M. H. Lee, H. K. Kim and K-W. Chi, *Dalton Trans.*, 2011, **40**, 3112.

- 15) R. Li, Y-P. Yuan, L-G Qiu, W. Zhang, J-F Zhu, *Small.*, 2012, **8**, 225.
- 16) T. K. Kim, J. H. Lee, D. Moon, and H. R. Moon, *Inorg. Chem.*, 2013, **52**, 589.
- 17) J. L. Novotney and W. R. Dichtel, *ACS Macro Lett.*, 2013, **2**, 423.
- 18) D. Gopalakrishnan and W. R. Dichtel, *J. Am. Chem. Soc.*, 2013, **135**, 8357.
- 19) C. Petit, T. J. Bandosz, *Adv. Mater.*, 2009, **21**, 4753.
- 20) Z-H. Huang, G. Liu, and F. Kang, *ACS Appl. Mater. Interfaces.*, 2012, **4**, 4942.
- 21) X. Liu, H. Zhou, Y. Zhang, Y. Liu, and A. Yuan, *Chin. J. Chem.*, 2012, **30**, 2563.
- 22) M. Jahan, Q. Bao, J-X. Yang, K. P. Loh, *J. Am. Chem. Soc.*, 2010, **132**, 14487.

Vita

Venkata Neti earned his Bachelor and Master of Science degrees in Chemistry from Sri Venkateswara University in 2006. In 2009 he joined the doctoral program in Chemistry at Clemson University, Clemson, SC. In fall 2010 he moved with his research supervisor to The University of Texas at El Paso. Throughout his doctoral research Venkata gained research experience in the design, synthesis, purification and characterization of organic/polymer/inorganic porous materials, carbon based nanomaterials, films. He made new 2D crystalline and amorphous polymers such as covalent organic frameworks (COFs) as prototypical ordered materials for energy storage and porous organic polymers (POPs) for CO₂ capture and energy storage.

Venkata has presented his research at the American Chemical Society national meetings and international conference meetings and workshops. Additionally Venkata has published his research in 8 international journals.

Venkata's dissertation, *Design and Synthesis of Porous Organic Frameworks for Hydrogen and Methane Storage and for Selective Carbon Dioxide adsorption*, was supervised by Dr. Luis Echegoyen.

Permanent address: D. No. 2-6, P.O. Ganapavaram

PIN: 534198, W. G. Dt, A.P, INDIA

This thesis/dissertation was typed by Venkata Surya Pavan Kumar Neti.